UC Irvine
UC Irvine Electronic Theses and Dissertations

Title
Nanoscale electronic properties of ferroelectric heterostructures studied via four-dimensional scanning transmission electron microscopy

Permalink
https://escholarship.org/uc/item/6pd3k37d

Author
Addiego, Christopher

Publication Date
2021

Peer reviewed|Thesis/dissertation

eScholarship.org Powered by the California Digital Library
University of California

UNIVERSITY OF CALIFORNIA,
IRVINE

Nanoscale electronic properties of ferroelectric heterostructures studied via four-dimensional scanning transmission electron microscopy

DISSERTATION

submitted in partial satisfaction of the requirements
for the degree of

DOCTOR OF PHILOSOPHY

in Physics

by

Christopher A. Addiego

Dissertation Committee:
Professor Xiaoqing Pan, Chair
Professor Ruqian Wu
Professor Zuzanna Siwy

2021

Portion of Chapter 1 © 2019 American Chemical Society
Portion of Chapter 2 © 2020 Elsevier
Portion of Chapter 3 and Appendix B © 2020 Springer Nature Ltd.
All other materials © 2021 Christopher A. Addiego

DEDICATION

To my parents and my sister

TABLE OF CONTENTS

Page

LIST OF FIGURES **v**

ACKNOWLEDGMENTS **vii**

VITA **ix**

ABSTRACT OF THE DISSERTATION **xii**

1 Introduction **1**
1.1 Ferroelectric materials 1
1.1.1 $BiFeO_3$ 4
1.1.2 $PbTiO_3$ 5
1.2 Transmission electron microscopy 6
1.2.1 Specimen Preparation 7
1.2.2 Conventional TEM 8
1.2.3 Scanning Transmission Electron Microscopy (STEM) 9
1.2.4 Theory of probe and image formation in STEM 13
1.2.5 Theory of high-energy electron scattering in thin samples 16
1.3 Imaging electronic properties in S/TEM and applications to ferroelectrics . . 19

2 4D STEM for electric field imaging **24**
2.1 Introduction to 4D STEM and electric field imaging in STEM 24
2.2 Experiments from bulk $SrTiO_3$ 32
2.3 Examining thickness and defocus dependence in $SrTiO_3$ 37
2.4 Conclusion 43

3 4D STEM applied to the $BiFeO_3$-$SrTiO_3$ interface **45**
3.1 Introduction 45
3.2 Bulk $SrTiO_3$ and $BiFeO_3$ 48
3.2.1 Electric field map and analysis 48
3.2.2 Charge density imaging and comparison with theory 50
3.3 $BiFeO_3$-$SrTiO_3$ interface 55
3.3.1 Atomic structure analysis 57
3.3.2 Charge Separation 60
3.3.3 Charge state measured with Bader charge analysis 61

3.3.4 EELS analysis . . . 65
3.4 Conclusion . . . 67

4 Electric field imaging in $PbTiO_3$-$SrTiO_3$ superlattice 68
4.1 Introduction . . . 68
4.2 Film growth and sample preparation . . . 70
4.3 Atomic scale E-field . . . 72
4.4 Nanometer scale E-field . . . 77
4.4.1 Phase field simulations . . . 79
4.5 Conclusion . . . 81

5 Charge density imaging of a $PbTiO_3$-$SrTiO_3$ interface 84
5.1 Introduction . . . 84
5.2 PTO/STO (100) projection . . . 86
5.3 PTO/STO (110) projection . . . 90
5.4 Image simulations from bulk materials from (110) projection . . . 93
5.5 Conclusion . . . 97

6 Summary and outlook 98

Appendix A Derivation of the projected electric field with the phase object approximation 123

Appendix B Position averaged CBED thickness measurements 126

LIST OF FIGURES

Page

1.1 Structure Models . . . 6
1.2 Ray Diagrams . . . 10
1.3 Diffraction pattern examples . . . 12

2.1 4D STEM/Scanning Diffraction . . . 27
2.2 Effect of probe size on electric field measurement . . . 31
2.3 Experimental Variation with Sample Thickness . . . 34
2.4 Momentum Transfer Line Profiles . . . 35
2.5 Camera noise effect . . . 36
2.6 Simulated Momentum Transfer . . . 38
2.7 Propagation of the Electron Probe . . . 40
2.8 Thickness Dependence of Momentum Transfer . . . 42

3.1 Atomic structure and electric field of STO . . . 49
3.2 Atomic structure and electric field dipole of BFO . . . 51
3.3 Real space charge density mapping in STO and BFO . . . 53
3.4 Separation of positive and negative charge in a BFO unit cell . . . 55
3.5 Atomic-resolution HAADF image and EDS maps across the BFO-STO interface 56
3.6 Charge-density map, O octahedron rotation and valence charge state at the interface between BFO and STO . . . 58
3.7 Measurement of O octahedron rotation . . . 59
3.8 Determination of the region for measuring the total charge of atomic columns 61
3.9 Measurement of the total charge of each atomic site . . . 63
3.10 Charge-intensity change as a function of valence . . . 64
3.11 High-resolution core-loss EELS measurement of Ti, O and Fe at the BFO-STO interface . . . 67

4.1 Superlattice and probe conditions . . . 71
4.2 Atomic scale electric field . . . 73
4.3 Polarization down E-field . . . 73
4.4 Average A-site electric field . . . 75
4.5 Average Ti/O site electric field . . . 76
4.6 Unit cell electric field . . . 76
4.7 Nanoscale electric field . . . 78
4.8 Polarization map . . . 79

4.9 Polarization correspondence 81

5.1 Comparison of perovskites 87
5.2 (100) PTO/STO Interface 89
5.3 (110) PTO/STO interface 92
5.4 EELS from (110) PTO/STO 94
5.5 Imaging simulations 96

ACKNOWLEDGMENTS

I would like to express my deepest gratitude to my adviser, Prof. Xiaoqing Pan, for his guidance, support, and instruction during my PhD program. His help has been essential at every step in the process as he has continuously pushed me hone my research skills and shown me how to be an effective scientist. I would also like to thank Prof. Ruqian Wu and Prof. Zuzzana Siwy for serving on my committee; their assistance and advice throughout my time in the program has been very valuable.

I would also like to thank my friends and colleagues in Pan Research Group for their help. I would especially like to thank Prof. Wenpei Gao for his mentorship and training throughout my PhD; his help was indispensable in turning from a curious graduate student into a proficient researcher. I would also like to thank the other post doctoral researchers in the group, Dr. Xingxu Yan, Dr. Mingjie Xu, Dr. Linze Li, Prof. Ye Zhang, and Prof. Sheng Dai for their training in the early years and collaboration in the later years of my PhD. I would also like to thank the other graduate students in Pan group whom I have worked closely with in my time at UCI, especially Chaitanya Gadre, Thomas Blum, Peter Tieu, Huaixun Huyan, and Tom Lee. Working with all of you has made this an incredibly enriching experience.

I would also like to thank the staff members at the Irvine Materials Research Institute, Dr. Toshi Aoki, Dr. Jian-guo Zheng, and Dr. Li Xing for their help, advice, and support of my work.

Significant portions of this text is reprinted from "Real-space charge-density imaging with sub-ångström resolution by four-dimensional electron microscopy" [Nature 575, 480-484 (2019)] and "Thickness and defocus dependence of inter-atomic electric fields measured by scanning diffraction" [Ultramicroscopy 208, 112850 (2020)]. Portions of the work presented here was performed and supervised by the co-authors listed on these articles: Wenpei Gao, Xiaoqing Pan, Hui Wang, Xingxu Yan, Yusheng Hou, Dianxiang Ji, Colin Heikes, Yi Zhang, Linze Li, Huaixun Huyan, Thomas Blum, Toshihiro Aoki, Yuefeng Nie, Darrell G. Schlom, and Ruqian Wu. I would also like to thank Elsevier and Springer Nature Ltd. for their permission to reproduce my previously published works in this dissertation.

Other portions of this text also contain unpublished work performed or supervised by collaborators: Jacob Zorn, Long-Qing Chen, Sujit Das, Ramamoorthy Ramesh, Lane W. Martin, Jie Li, and Ruqian Wu.

I would like to acknowledge funding provided by US Department of Energy, Office of Basic Energy Sciences, Division of Materials Sciences and Engineering under Award DE-SC0014430, the US National Science Foundation (NSF) under grant number DMR-1506535, and DMR-2034738. Electron microscopy experiments and sample preparation were performed at the Irvine Materials Research Institute supported in part by the National Science Foundation through the Materials Research Science and Engineering Center program (DMR-2011967).

Finally, I would like to thank my family, Mom, Dad, and Rina, friends, =N4D=, and girlfriend, Elisa, for their continued support. It would not have been possible without you.

VITA

Christopher A. Addiego

EDUCATION

Doctor of Philosophy in Physics **2021**
University of California, Irvine *Irvine, CA*

Master of Science in Physics **2017**
University of California, Irvine *Irvine, CA*

Bachelor of Science in Physics **2015**
Carnegie Mellon University *Pittsburgh, PA*

RESEARCH EXPERIENCE

Graduate Research Assistant **2017–2021**
University of California, Irvine *Irvine, CA*

TEACHING EXPERIENCE

Teaching Assistant **2015–2017**
University of California, Irvine *Irvine, CA*

REFEREED JOURNAL PUBLICATIONS

Direct observation of polarization-induced two-dimensional electron/hole gases at ferroelectric-insulator interface **2021**
H. Huyan **et al.** *npj Quantum Materials* **7**, 88.

Emergent properties properties at oxide interfaces controlled by ferroelectric polarization **2021**
F. Ye **et al.** *npj Computational Materials* **7**, 130.

Manipulating magnetoelectric energy landscape in multiferroics **2020**
Y.L. Huang **et al.** *Nature Communications* **11**, 2836.

Enhanced electrical properties of $La_{1.9}Nd_{0.1}Ti_2O_7$ ceramics **2020**
Y. Li **et al.** *Journal of Materials Science: Materials in Electronics* **31**, 1853-1860.

Thickness and defocus dependence of inter-atomic electric fields measured by scanning diffraction **2020**
C. Addiego, et al. *Ultramicroscopy* **208**, 112850

Real-space charge-density imaging with sub-ångström resolution by four-dimensional electron microscopy. **2019**
W. Gao, **C. Addiego**, H. Wang et al. *Nature* **575**, 480-484.

Structures and electronic properties of domain walls in $BiFeO_3$ thin films **2019**
H. Huyan **et al.** *National Science Review* **6**, 669-683.

Probing the dynamics of nanoparticle formation from a precursor at atomic resolution **2019**
W. Gao **et al.** *Science Advances* **5**, eaau9590.

Intercorrelated in-plane and out-of-plane ferroelectricity in ultrathin two-dimensional layered semiconductor In_2Se_3 **2018**
C. Cui **et al.** *Nano Letters* **18**, 1253-1258.

Platinum-based nanowires as active catalysts toward oxygen reduction reaction: *in-situ* observation of surface-diffusion-assisted, solid-state oriented attachment **2017**
Y. Ma **et al.**, *Advanced Materials* **29**, 1703460.

REFEREED CONFERENCE PUBLICATIONS

Observation of a charged incoherent $BiFeO_3/SrTiO_3$ interface **Aug 2021**
Microscopy and Microanalysis

Multiscale Electric Field Imaging in Ferroelectric Vortices **Mar 2021**
APS March Meeting

Multiscale electric field imaging of vortices in $PbTiO_3$-$SrTiO_3$ superlattice **Aug 2020**
Microscopy and Microanalysis

Polarization in ferroelectric $BiFeO_3$ imaged in 3D using four-dimensional scanning transmission electron microscopy **Aug 2020**
Microscopy and Microanalysis

Charge density mapping via scanning diffraction in scanning transmission electron microscopy **Aug 2019**
Microscopy and Microanalysis

Charge density imaging of a ferroelectric-insulator interface with sub-Å resolution **Mar 2019**
APS March Meeting

Calculation of electric field based on average momentum transfer using pixelated electron detectors in STEM **Apr 2018**
MRS Spring Meeting

Calculation of electric field based on average momentum transfer using pixelated electron detectors in STEM **Aug 2017**
Microscopy and Microanalysis

ABSTRACT OF THE DISSERTATION

Nanoscale electronic properties of ferroelectric heterostructures studied via four-dimensional scanning transmission electron microscopy

By

Christopher A. Addiego

Doctor of Philosophy in Physics

University of California, Irvine, 2021

Professor Xiaoqing Pan, Chair

Due to their intrinsic polarization, ferroelectric materials have a variety of applications in electronic, optical, and electromechanical devices. In addition, modern thin film growth techniques such as molecular beam epitaxy and pulsed laser deposition have made it possible to grow heterostructures with atomically sharp interfaces leading to the discovery of many new phenomena and functional properties stemming from the coupling between the ferroelectric and the substrate material. In the study of these thin films, transmission electron microscopy has been a powerful technique for high resolution structural and chemical characterization of these heterostructures. With the development of fast pixelated detectors, four-dimensional scanning transmission electron microscopy (4D STEM) has led to the emergence of new techniques for directly interrogating the electronic properties of ferroelectrics with atomic resolution. This opens new opportunities for studying both the mechanisms for how macroscopic properties can emerge from atomic scale electronic phenomena and the fundamental physics of ferroelectricity. In this work, new analysis techniques based on 4D STEM electric field and charge density imaging are developed and applied to reveal the electronic properties of ferroelectric heterostructures.

First, we systematically study the effect of sample thickness and electron probe defocus on

the electric field measured in 4D STEM and demonstrate that the technique can be extended to samples up to 20 nm thickness. Next, new quantitative analysis techniques for 4D STEM charge density images are developed. These techniques are applied to a $BiFeO_3$-$SrTiO_3$ (ferroelectric-insulator) heterostructure, which reveals the local electronic properties of the interface. Through a combination of methods, we showed that there is charge accumulation at the interface due to an asynchronous change in the structural polarization and the charge distribution across the interface. Applying 4D STEM electric field imaging to $PbTiO_3$-$SrTiO_3$ superlattice, we found that asymmetric features in atomic scale images originate from the charge distribution in perovskite ferroelectrics and while nanometer-resolution images reveal the total electric field of the material system. Finally, an in-depth study of how Bader charge analysis, adapted for use with 4D STEM charge density images, can be leveraged to understand the bonding properties of $PbTiO_3$. These results demonstrate the potential of 4D STEM for investigating the electronic properties of materials and provide new insights into the behavior of ferroelectric heterostructures.

Chapter 1

Introduction

1.1 Ferroelectric materials

Ferroelectric materials exhibit a spontaneous electric polarization which can be reoriented with an external electric field; they are named analogously to the more common ferromagnets which exhibit spontaneous magnetization. In ferroelectric materials, the electric polarization in the material is generated by a separation of the positive and negative charge centers in the unit cell. This is generally driven by a structural distortion or broken symmetry in the unit cell which causes displacement of the anions, cations, and the valence electrons in the material [1–4]. Similar to ferromagnets, ferroelectrics can also form large regions of uniform polarization called domains [5–8]. The polarization of ferroelectric domains can be switched between different stable configurations with an applied electric field. The manipulation of ferroelectric domains and the interaction of the polarization with other properties/structures forms the basis for a significant portion of the research in ferroelectric materials.

Ferroelectric materials are a particularly promising candidate for components in future electronic devices. The stability of ferroelectric polarization states even in the absence of an

external field, the size of ferroelectric domains (less than 10nm in some cases), and the speed of ferroelectric switching makes ferroelectrics ideal for low power non-volatile memory [9–12]. In the first designs for ferroelectric based memory, the dielectric in standard capacitave dynamic random access memory cells was replaced with a ferroelectric layer, which allows the cell to hold it's charge without needing to be refreshed, making it non-volatile. More recent designs use the structure of the ferroelectric itself to store data. For example, in ferroelectric tunnel junctions, an ultra thin ferroelectric film is used to modulate the tunneling barrier between two electrodes [13–16]. Recent studies have also shown that conductive ferroelectric domain walls, with their ability to be written and erased with an applied field, can be used to create non-volatile resistive memories [17–19].

Many of the more recent designs for ferroelectric-based devices have relied on advances in thin film growth technology that allow for single atomic layers to be deposited with precise control over composition and structure. Molecular beam epitaxy (MBE) and pulsed laser deposition (PLD) have enabled the growth of high quality oxide ferroelectric thin films on a variety of substrates with a wide range of thicknesses [20–22]. As a result, many novel properties have also been discovered in ferroelectric interfaces and heterostructures [7, 23, 24]. Charge accumulation at perovskite (ABO_3 structure) ferroelectric interfaces is one phenomenon that has garnered significant interest since it's initial discovery in the non-ferroelectric $LaAlO_3/SrTiO_3$ [25]. Ferroelectric oxides grown on insulating substrates present a unique opportunity to tune and engineer the two-dimensional electron or hole gas (2DEG or 2DHG) that appears at oxide interfaces due to coupling between the polarization and free charge. The spontaneous polarization of ferroelectrics generates bound charge at the insulating interface. This bound charge in-turn attracts free charges to the interface, either resulting in the formation of a 2DEG/2DHG or the modification of an existing 2DEG/2DHG.

Theoretical studies predicted that a polarization controlled 2DEG/2DHG will appear at a variety of ferroelectric-insulator interfaces, including $KNbO_3/ATiO_3$ (A = Sr, Ba, Pb),

$BiFeO_3/SrTiO_3$, $BaTiO_3/SrTiO_3$, and $PbTiO_3/SrTiO_3$ [26–29]. In cases where the polar catastrophe model applies (materials with charged sub-layers) [30], the polarization modifies the existing 2DEG/2DHG by moving additional free holes or electrons towards the interface, depending on the polarization direction. In cases where the polar catastrophe model does not apply, the polarization alone causes charge accumulation. Despite the theoretical studies described above, there is still significant experimental work to be done in characterizing the electronic properties of these structures. Although imaging the atomic structure is quite routine, understanding the charge distribution and bonding structure in ferroelectric heterostructures is still a challenging task. Although piezoresponse force microscopy (PFM) and conductive atomic force microscopy (cAFM) have proven valuable tools in understanding the domain structure and charge distribution at the scale of 10's of nanometers [31–33], they do not have the spatial resolution necessary to understand how the atomic structure of the interface affects the 2DEG/2DHG. As will be described in the subsequent sections and chapters, scanning transmission electron microscopy (STEM) has the spatial resolution necessary to study the atomically sharp interfaces that lead to charge accumulation.

While most of the materials systems described above consist of only a single thin film, layer-by-layer control of film growth has also led to the synthesis of a variety of multi-layer structures as well. Where as the polarization of most thin film ferroelectrics are determined by the electrical and elastic boundary conditions provided by the substrate or surface, multi-layer systems offer an additional degree of freedom in their periodicity. In thin films, elsatic boundary conditions are determined by the misfit strain of the substrate which gradually relaxes as the film thickness increases. The electrical boundary conditions are determined by the conductivity of the substrate and the degree to which the bound charge is compensated. This is especially important because bound charge generates its own electric field called the depolarization field which can reduce the polarization in the material. The balance of the spontaneous polarization, depolarization field, and charge compensation at the interface determines its electrical properties [34]. In multi-layer or superlattice structures, the strain

relaxation and the strength of depolarization fields can both be adjusted by introducing layers of insulating material between ferroelectric layers. In $PbTiO_3/SrTiO_3$ superlattice, the strain and electrical boundary conditions favor different perpendicular polarization directions. Therefore, adjusting the balance of these two by changing multi-layer or superlattice periodicity can induce exotic polarization structures, such as vortices, skyrmions, and flux closure domains, in addition to the regular $\mathbf{a}_1/\mathbf{a}_2$ and $\mathbf{a}/\mathbf{c}$ domains [35–38]. Similar topological polarization structures and rotational nanodomains have also been observed in $LuFeO_3/LuFe_2O_4$ and $BiFeO_3/SrTiO_3$ superlattice [39, 40].

1.1.1 $BiFeO_3$

$BiFeO_3$ (BFO) is a multiferroic perovskite that exhibits strong ferroelecricity and weak antiferromagnetism at room temperature. In bulk BFO, the unit cell is rhombohedral, but in epitaxial thin films, BFO adopts a distorted monoclinic structure depending on the misfit strain of the substrate [8]. If the misfit strain between BFO and the substrate is less than 4.5%, the film adopts a rhombohedral-like (R-like) structure. In R-like BFO, the unit cell is often viewed as two pseudo-cubic unit cells connected along the body diagonal with the oxygen octahedrons rotated in opposite directions. In the pseudo-cubic structure, polarization can be pointed along any of the $\langle 111\rangle_{PC}$ directions, where PC denotes pseudo-cubic indices. Therefore, in the $[010]_{PC}$ projection, polarization appears to be along $[10\bar{1}]_{PC}$; this is illustrated in fig. 1.1a. The polarization in BFO is caused by a rotation of the oxygen octahedron about $\langle 111\rangle$ and displacement of the Fe atom away from the center of the adjacent four Bi atoms. In bulk, the rotation can be as much as 13.8°, but it is generally less in thin films due to constraints of the substrate [41]. If the misfit strain is greater than 4.5%, then the BFO unit cell adopts a tetragonal-like (T-like) structure. In this case, the oxygen octahedron is stretched along the growth direction, [001], and the Fe atom is also displaced along [001]. As a result, polarization in T-like BFO is along [001].

BFO thin films can exhibit a variety of domain structures. The domains in R-like BFO are classified based on the rotation angle between the polarization vectors; the allowed rotations are 71°, 109°, and 180°. Which domains form and their exact structure depends on the precise boundary conditions of the film. For example, BFO grown on $TbScO_3$ (TSO) exhibits 109°domains that form ordered stripes along $[110]_{TSO}$ [42] while BFO grown on $SrTiO_3$ (STO) will also form 109°domains, but with random orientation along either $[100]_{STO}$ or $[010]_{STO}$ [43]. More exotic domain patterns can also appear in BFO thin films depending on the balance of electrical and elastic boundary conditions. Triangular vortex nanodomains can form at the termination of 109°domain walls at BFO-insulator interfaces. These vortex domains form to minimize the electrostatic energy associated with bound charges at the interface which cannot be compensated by the insulating interface [34, 44]. Polar half vortices (merons) have also been observed in ultrathin BFO thin films where the surface has been modified with Bi_2O_3 islands. In this case, the presence of Bi_2O_3 on the surface modifies the electrical boundary conditions by introducing a strong dipole field which increases the surrounding polarization [45].

Charged domain walls can also appear in BFO [17, 18, 46]. These domain walls exhibit either head-to-head or tail-to-tail polarization, causing a large concentration of bound charge that attracts compensating free charges and thus generate a localized insulator-metal transition. These domain walls are especially interesting for memory applications because the charged domain wall can be written and erased with an external electric field.

1.1.2 $PbTiO_3$

$PbTiO_3$ (PTO) is a prototypical perovskite ferroelectric that has a tetragonal structure. In PTO thin films, the polarization is directed along $\langle 001 \rangle$ and is associated with the displacement of the central Ti column and distortion of the oxygen octahedron. The domain structure

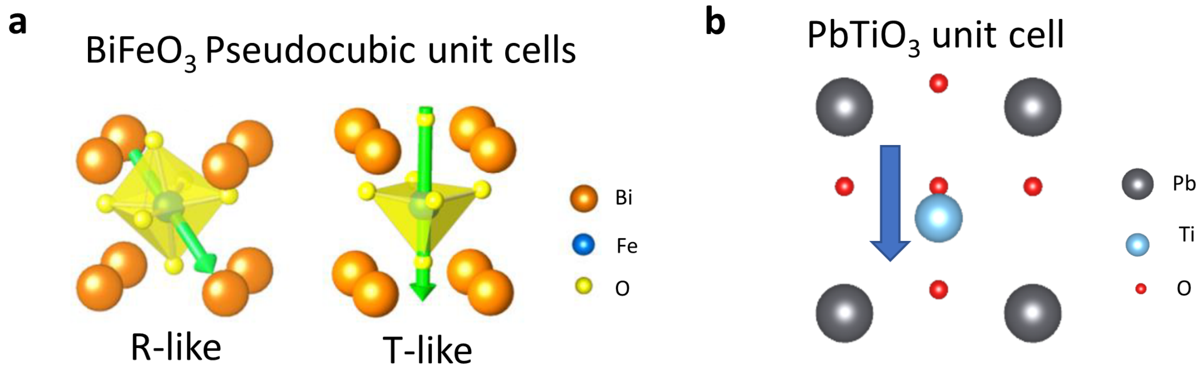

Figure 1.1: **Structure Models.** **a**, Atomic structure models for the pseudocubic unit cells of $BiFeO_3$. **b**, atomic structure model of the $PbTiO_3$ unit cell. Arrows indicate polarization direction. **a** is adapted from Li et al., Nano Lett. 2019, 19, 10, 6812–6818 with permission Copyright 2019 American Chemical Society.

in PTO generally exhibits either 180°or 90°domain walls. In the case of 90°domains, the polarization can be either in the *a/c* or a_1/a_2, where *a* refers to in-plane directions and *c* refers to the out-of-plane/growth direction [47–49]. Recently, PTO/STO superlattice structures have garnered significant attention due to the discovery of polarization vortex structures [35]. Further studies have found that a range of different domain structures can be stabilized by adjusting the superlattice periodicity [36, 50]. In addition, *in-situ* studies have also shown that the domain structures of the superlattice can be reversibly erased and written with an applied electric field or compressive forces [50–52].

1.2 Transmission electron microscopy

Transmission electron microscopy (TEM) has been used extensively to study oxide thin films. The TEM uses series of magnetic lenses to focus a high energy beam of electrons through an ultra thin specimen and focus an image onto a camera or into a spectrometer. The TEM specimens are prepared via either mechanical polishing and low energy ion milling or with a dual-beam scanning electron microscope (SEM)/focused ion beam (FIB) system [53, 54].

The development of aberration correctors has allowed TEMs to achieve sub-Å resolution routinely [55, 56]. TEMs can generally be operated in conventional mode where the beam is parallel or in scanning mode where the beam is converged into a fine probe. Both modes are useful in the study of oxide thin films.

1.2.1 Specimen Preparation

High quality TEM imaging requires preparing high quality specimens. Thin film specimens are generally prepared such that the film cross-section will be visible in the final specimen. Both the conventional method involving mechanical polishing followed by low energy ion milling and FIB preparation can produce high quality specimens with their own advantages. In the mechanical polishing process, a section of the thin film (approximately 5 mm square) is first glued to a piece of sacrificial silicon and then polished into a wedge with a shallow angle such that the silicon is slowly polished away using successively smoother lapping films until the specimen is as thin as possible while avoiding any cracking. Then the specimen is transferred to a low energy Ar ion milling system, Gatan PIPS II, and thinned to electron transparency [53]. In the FIB preparation process, a small section of the thin film (approximately 20 μm width x 2 μm height x 10 μm deep) is cut out of the surface of the film and mounted to a copper grid using the FIB. The grid is then rotated such that the thin film is facing the ion beam head-on and the 2 μm height is milled away until the sample is electron transparent [54].

Mechanically polished samples generally have the advantage of resulting in a large cross-section of the film being electron transparent, and thus accessible for imaging. The thickness along the beam direction can vary from less than 5 nm at the center of the ion milled region to over 100 nm at the edges. Since the sample is prepared in a wedge shape, the thinnest regions will always appear closer to the film surface. The large initial size of the mechanically

polished specimen and the wide thickness variability means that a wide variety of microscopic structures are present in the specimen, but it is difficult to tell what these structures are prior to completing the sample as there is little microscopic control over exactly which region the sample is cut from. In contrast, FIB specimens can be made with uniform thickness along the beam direction and the SEM/FIB can be used to select specific features/regions to include in the sample. However, it is very difficult to make a FIB specimen less than 20 nm in thickness along the beam direction without the ion beam causing significant damage, precluding their use in combination with a variety of advanced S/TEM that require very thin samples.

In the imaging of electronic properties, many techniques require specimens to be 5-10 nm thick along the beam direction. Therefore, all specimens used in this work were prepared by mechanical polishing and low energy ion-milling.

1.2.2 Conventional TEM

In conventional TEM, the parallel beam electron beam scatters into a series of diffracted beams after interacting with the lattice planes in the sample and the objective lens focuses these beams into a diffraction pattern in the back focal plane of the microscope. The intermediate and projector lenses of the microscope can be configured to either project this diffraction pattern directly on to a camera or to allow the diffracted beams to interfere with each other and form an image which is projected onto the camera, as shown in fig. 1.2a. In each mode, the TEM provides an image of the electron beam in either real space (imaging) or reciprocal/momentum space (diffraction) [53].

In high resolution TEM (HRTEM) imaging, all diffracted beams focused in the back focal plane are allowed to interfere together to form the final image. The resulting image is called a phase-contrast image because the complex phase relationship of all the diffracted beams determines the final image. In general, the phase change is associated with interactions

between the electron beam and the electrostatic potential of the sample. When samples are very thin (less than about 5 nm), the phase-object approximation can be used to understand the contrast of the image and advanced techniques like holography can be used to determine the electrostatic potential. Under the phase-object approximation, the interaction with the sample is modeled as only a phase shift of the initial beam which is linearly related to the electrostatic potential [57–62]. However, under most circumstances, this interaction is non-linear, so contrast in the final image cannot be directly interpreted as being representative of the atomic structure. In addition, the phase of the electron beam is highly sensitive to slight changes in sample thickness, zone-axis alignment, and lens aberrations. As a result, HRTEM is not the favored method for studying oxide thin films at atomic resolution unless a more advanced phase-reconstruction technique, such as holography, is being employed.

Other lower resolution imaging modes, such as bright-field (BF) or dark field (DF) imaging are often used in studying ferroelectrics because they exhibit strong contrast between domains. In BF/DF imaging, only one beam is selected to form an image in the back focal plane by inserting an aperture. In BF imaging, the undiffracted beam is selected, while in DF imaging, a diffracted beam is selected. These modes exhibit strong contrast between ferroelectric domains because image contrast is generated by slight changes in the diffraction condition which is strongly affected by the polarization direction [44, 63]. However, since only one diffracted beam is used to form the image, high resolution imaging is not possible.

1.2.3 Scanning Transmission Electron Microscopy (STEM)

In STEM, the incident electron beam is converged into a small probe and focused on the sample surface. With aberration correction, the probe can reach 0.6 Å full-width half-max (FWHM). Scanning coils are then used to raster scan the beam across the sample in a regular grid. Unlike in conventional TEM, a STEM always operates in diffraction mode, projecting

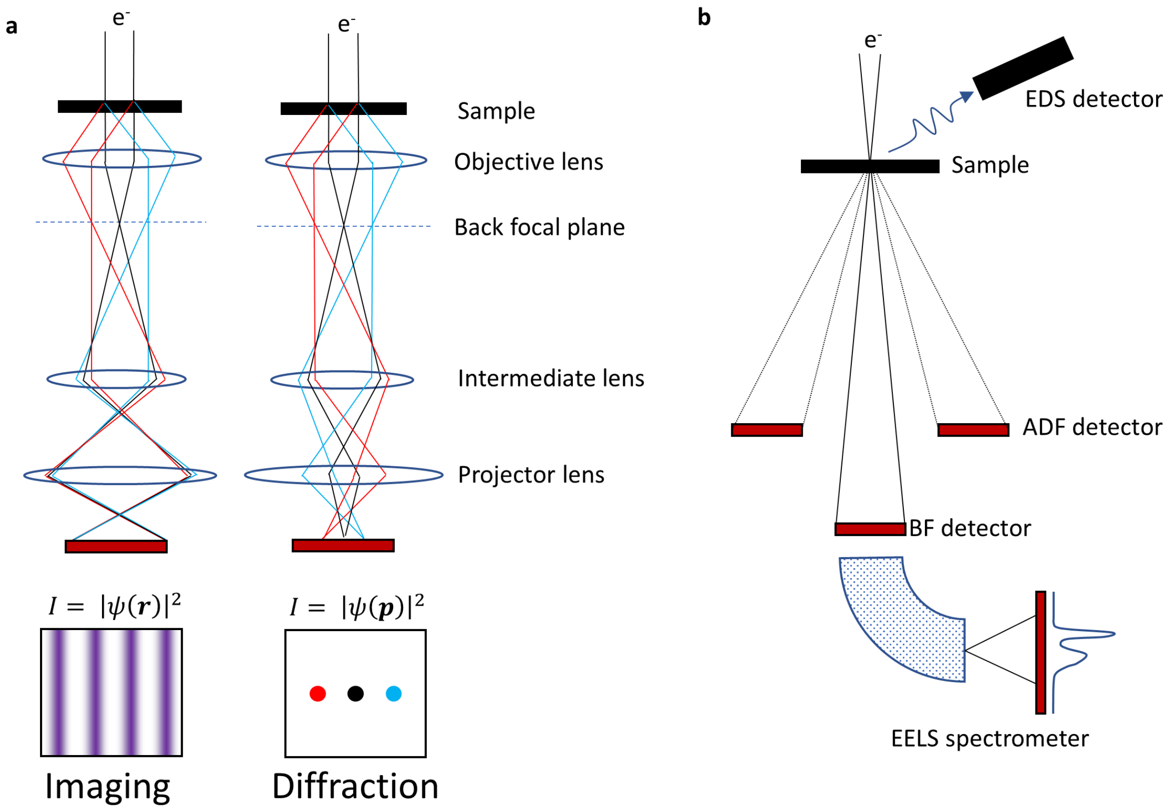

Figure 1.2: **Ray Diagrams.** **a**, Schematic diagram of a TEM in imaging and diffraction modes. **b**, Schematic diagram of a STEM, including STEM detectors and associated EDS and EELS spectrometers

a convergent beam electron diffraction (CBED) pattern onto the detectors below the sample. This is depicted schematically in fig. 1.2b. In a CBED pattern, the spots of a conventional diffraction pattern are expanded into disks with diameter matching the convergence angle of the probe. Depending on the lattice spacing and convergence angle, the disks may overlap. This is illustrated in Fig. 1.3. All diffraction patterns shown in 1.3 are collected from the same material, $PbTiO_3$ (in-plane lattice parameter = 3.9Å), but under different illumination conditions. The first diffraction pattern on the far left is collected in a TEM under parallel beam illumination, so the diffraction spots are single points. On the right, the diffraction patterns are collected with a convergent beam in STEM mode with increasing convergence angles. The experimental CBED patterns show that as the convergence angle increases, the diffraction disks start to overlap with each other until only the central disk is visible at the highest convergence angles. As depicted schematically, increasing the convergence angle also decreases the size of the electron probe. Therefore, smaller convergence angles are useful when features of the diffraction disks are important to the experiment while larger convergence angles are most useful when high resolution imaging is the goal.

In STEM, conventional images are constructed by measuring how many electrons are scattered into different angular ranges. As before, BF images are constructed from measuring only weakly scattered electrons from the center of the central disk. Annular bright field (ABF) images are also constructed from the central disk, but only includes electrons scattered between half the convergence angle and the full convergence angle of the probe. Both BF and ABF images are phase-contrast imaging methods and are similarly sensitive to external factors that affect the probe phase, such as sample thickness and alignment. However BF and ABF images are still useful in STEM because they can image both heavy and light elements under the right conditions [64–66]. Electrons scattered to angles greater than the convergence angle are collected in annular dark field (ADF) detectors. Unlike DF images in conventional TEM, all electrons scattered outside the center disk are integrated together. High angle annular dark field (HAADF) imaging is particularly useful in the study of oxide

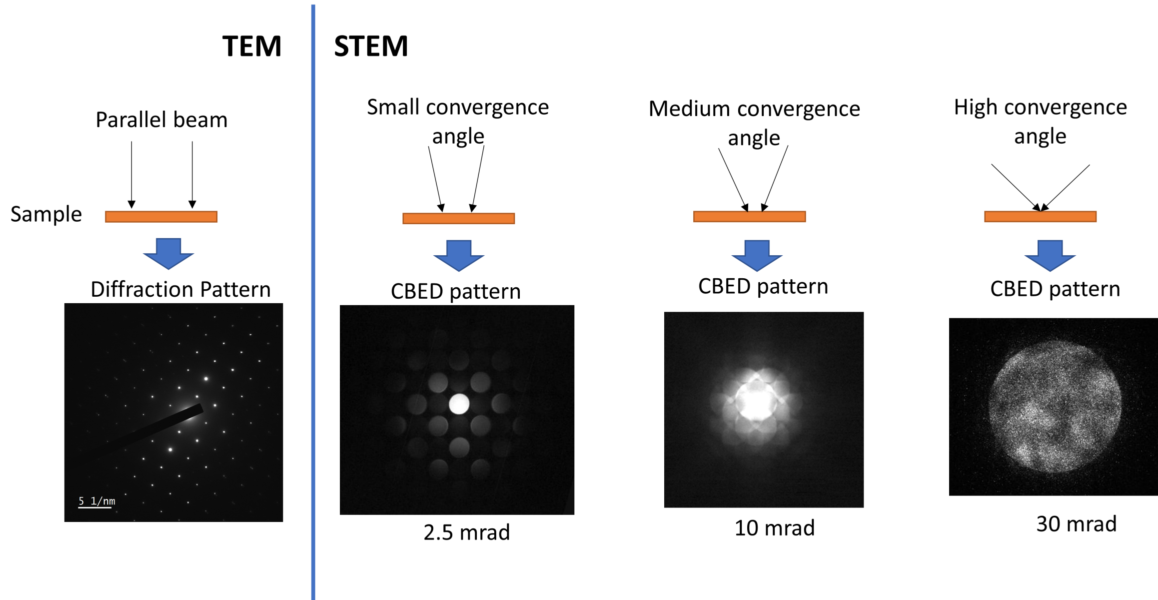

Figure 1.3: **Diffraction pattern examples.** Schematic diagram of the electron beam illumination condition under varying convergence angles and example diffraction patterns taken from $PbTiO_3$ in TEM mode and in STEM mode.

thin films because the intensity is proportional to the Z of the nucleus (intensity $\propto Z^{1.7}$) [67]. This allows atomic species to be easily distinguished in images. Contrast in HAADF images are also less sensitive to changes in thickness and zone-axis alignment, making it a more robust imaging method.

When the electron probe interacts with the sample, it can also generate a wide range of excitations in the material that can be studied with spectroscopy. Due to the spatial resolution of the electron probe, synchronizing a spectrometer with the raster scan allows for an individual spectrum to be associated with a pixel position. This allows the unmatched spatial resolution of STEM to be applied to spectroscopic techniques which often have much lower spatial resolution in other settings. There are two primary spectroscopic measurements integrated in STEM: X-ray energy dispersive spectroscopy (EDS) and electron energy loss spectroscopy (EELS). In EDS, the electron beam ionizes a core electron and a valence electron falls down to fill the vacancy, emitting a characteristic x-ray which is collected by a spectrometer. In EELS, the incident electron beam scatters inelastically off an atom,

depositing a small amount of its energy in the material and causing an excitation; the excitation energy can lead to the generation of phonons, plasmons, characteristic x-rays, or band gap transitions. The whole electron beam is then passed through a magnetic prism which disperses the beam according to the energy of each electron so that the change in the electron's energy can be analyzed to determine the excitation it caused in the material. Both EDS and EELS can be used to measure chemical composition based on the x-ray emissions. But EELS can also be used to study a variety of other properties, including the electronic properties of the material.

1.2.4 Theory of probe and image formation in STEM

The formation of the STEM probe can be described in terms of the wave function of electron beam. In STEM mode, the condenser lenses of the microscope converge the entire electron beam coming out of the electron gun onto the sample, but only the central portion of the beam will form a coherent wave. Therefore, a circular condenser aperture is inserted to block the incoherent portions of the beam. This process is described by a top hat function in momentum space [62, 68]:

$$A(\mathbf{k}) = \begin{cases} 1, & \text{for } |\mathbf{k}| < k_{\text{max}}, \\ 0, & \text{otherwise} \end{cases} \tag{1.1}$$

where k_{max} is defined by the radius of the condenser aperture. In practice, k_{max} is typically measured in terms of the semi-convergence angle $\alpha \approx k_{\text{max}}(\lambda/2\pi)$ (quoted in mrad), where λ is the relativistic wavelength of the high energy electrons. In the absence of any other factors, a small aperture that cuts out only the very center of the coherent region of the

beam would produce a diffraction limited probe with spatial resolution [68]

$$d_d = \frac{0.61\lambda}{\alpha} \tag{1.2}$$

Therefore, using a larger aperture to increase the convergence angle will generally increase the spatial resolution (decrease d_d). However, this only works up to a point because all lenses exhibit aberrations that will further broaden the beam, especially when using higher convergence angles. Spherical aberrations are the result rays from the edge of the lens being over-focused compared to rays from the center of the lens. Aberrations introduce a phase error to the electron wave function modeled by the aberration function:

$$\chi(\alpha) = \frac{1}{2}\delta f \alpha^2 + \frac{1}{4}C_{3,0}\alpha^4 + \frac{1}{6}C_{5,0}\alpha^6 + ... \tag{1.3}$$

where δf is the probe defocus (position of the focus), $C_{3,0}$ and $C_{5,0}$ are 3rd and 5th order spherical aberration coefficients [68]. Real electron optical systems are not perfectly symmetric, so additional terms can also be added to account for aberrations with different symmetry. Prior to the invention of aberration correctors for S/TEMs [55, 56], spatial resolution was dominated by $C_{3,0}$. Most modern aberration correctors can correct up to 3rd order spherical aberrations. Therefore, the ideal spatial resolution is limited by $C_{5,0}$ and can be approximated as

$$d_5 = 0.45\lambda^{5/6}C_5^{1/6} \tag{1.4}$$

For the JEOL JEM-ARM300F at University of California, Irvine, operating at 300kV, $C_{5,0} < 1$ mm; therefore, $d_5 = 0.2$ Å. In reality, lower order aberrations, along with electronic noise and environmental factors also impact the final probe size, so the spatial resolution in experiment is closer to 0.6 Å.

Putting this all together, the aperture and aberration functions, the wave function of the probe in real space shifted to a position $\mathbf{r}_o$ by the scanning coils, $\Psi(\mathbf{r}, \mathbf{r}_o)$, is given by [62, 68]

$$\Psi(\mathbf{r}, \mathbf{r}_o) = \mathrm{FT}^{-1}\left[A(\mathbf{k})e^{-i\chi}\right] \otimes \delta(\mathbf{r} - \mathbf{r}_o) \tag{1.5}$$

$$= \int A(\mathbf{k})e^{-i\chi}e^{i\mathbf{k}\cdot\mathbf{r}}d\mathbf{k} \otimes \delta(\mathbf{r} - \mathbf{r}_o) \tag{1.6}$$

The portion inside the fourier transform describes the probe formation by the condenser aperture along with the phase error introduced by the lens aberrations. The convolution with delta function represents the scanning of the probe across the sample in real-space by the scanning coils. With the help of the convolution theorem, the convolution in real-space can be turned into a multiplication in reciprocal space and the translation of the probe can be brought inside the Fourier transform as an additional phase factor. With this simplification, the final probe wave function at the sample surface is [68]

$$\Psi(\mathbf{r}, \mathbf{r}_o) = \int A(\mathbf{k})e^{-i\chi}e^{i\mathbf{k}\cdot(\mathbf{r}-\mathbf{r}_o)}d\mathbf{k} \tag{1.7}$$

In STEM mode, the imaging process may be either coherent or incoherent depending on size of the detector. The type of imaging affects the image formation in the plane of the detector. For the case of coherent imaging, the intensity in the detector plane is

$$I_{\text{coherent}} = |\Psi(\mathbf{r}_o) \otimes V_{\text{obj}}(\mathbf{r}_o)|^2 \tag{1.8}$$

where V_{obj} is the object function describing the sample, typically this is the electrostatic potential of the object. For the case of incoherent imaging, the intensity in the detector plane is

$$I_{\text{incoherent}} = |\Psi(\mathbf{r}_o)|^2 \otimes |V_{\text{obj}}(\mathbf{r}_o)|^2 \tag{1.9}$$

In either case, the image will be formed by integrating a range of scattering angles reciprocal space with an annular detector to get an intensity value for each scan position. If the detector is small compared to the features in the diffraction pattern (integrating a small angular range), it will be sensitive to interference effects that generate contrast in the diffraction pattern and the resulting image will be coherent. If the detector is large (integrating a large angular range), then any interference effects will be averaged out and the resulting image will be incoherent. Depending on the lens conditions (convergence angle and projector lens settings), BF imaging can be either coherent or incoherent, although it is generally used as a coherent imaging method. In contrast, ADF/HAADF imaging is always an incoherent method [68, 69].

1.2.5 Theory of high-energy electron scattering in thin samples

This section will present a simplified description of the electron probe's interaction with a thin sample starting from the non-relativistic Schrodinger equation where the goal is to derive the exit wave function of the probe as described by the phase-object approximation. This approximation forms the basis of all phase-retrieval methods that are used for imaging the electronic properties of materials which will be described in sections 1.3 and 2.1. The derivation here is adapted from ref [70] and [71]. The Schrodinger equation for a single electron interacting with the sample is

$$\left(-\frac{\hbar}{2m_e}\nabla^2 - eV(\mathbf{r})\right)\Psi(\mathbf{r}) = E_e\Psi(\mathbf{r}) \tag{1.10}$$

where $V(\mathbf{r})$ is the potential of the sample, E_e is the energy of the electron, Ψ is the electron wave function, and $\mathbf{r} = (x, y, z)$. Since the electron primarily moves along the z-direction, the wave function can be broken into two parts, one part is a plane wave along the z-direction which captures the wave generated by the high-voltage acceleration of the electron, and one

part that varies slowly in z that captures its interaction with the sample. Therefore, the electron wave function can be written as

$$\Psi(\mathbf{r}) = \psi(\mathbf{r})e^{ikz} \tag{1.11}$$

where k is the magnitude of the wave vector $\mathbf{k} = (k_x, k_y, k_z)$ defined by the energy of the electron such that $k = 2\pi/\lambda = \sqrt{2m_e E_e}/\hbar$. So $\psi(\mathbf{r})$ must vary over much larger distances compared to λ. Substituting eq. 1.11 into eq. 1.10 and then computing the Laplacian yields

$$-\frac{\hbar^2}{2m_e}\left(\nabla^2 + 2ik\frac{\partial}{\partial z} - k^2\right)\psi(\mathbf{r}) - eV(\mathbf{r})\psi(\mathbf{r}) = E_e\psi(\mathbf{r}) \tag{1.12}$$

If we express the energy in terms of the wave vector, then the k^2 terms will be eliminated and eq. 1.12 can be simplified to

$$\left(\nabla^2 + 2ik\frac{\partial}{\partial z} + \frac{2m_e e}{\hbar^2}V(\mathbf{r})\right)\psi(\mathbf{r}) = 0 \tag{1.13}$$

Considering the fact that the electron momentum is almost entirely along the z-direction and ψ varies slowly along z, the second derivative of ψ with respect to z will be small compared to other terms and can be safely neglected, so the Laplacian will operate only along the in-plane directions. This assumption allows us to separate the components of eq. 1.13 such that it can be expressed as a first order differential equation in z

$$\frac{\partial}{\partial z}\psi(\mathbf{r}) = \left(\frac{i}{2k}\nabla_\perp^2 + i\sigma V(\mathbf{r})\right)\psi(\mathbf{r}) \tag{1.14}$$

where $\nabla_\perp$ contains the in-plane derivatives with respect to (x, y) and $\sigma = m_e e/k\hbar^2$. Notice that in the absence of a sample ($V(\mathbf{r}) = 0$), then only first term remains and eq. 1.14 describes the propagation of the electron through free space. For this reason, the first term

is often referred to as the propagation operator. In the opposite case where the sample is infinity thin, propagation can be ignored and only the second term remains which describes the transmission of the wave function through the thin sample. For this reason, the second term is is often referred to as the transmission operator. In the case of an infinitely thin sample, eq. 1.14 becomes

$$\frac{\partial}{\partial z}\psi(\mathbf{r}) = i\sigma V(\mathbf{r})\psi(\mathbf{r}) \tag{1.15}$$

Based on eq. 1.15, ψ can be expressed as

$$\psi(x, y, z) = \exp\left[i\sigma \int_0^z V(x, y, z)dz'\right]\psi(x, y, 0) \tag{1.16}$$

where $\psi(x, y, 0)$ is the initial wave function. Notice that the integral is simply a projection of the potential along the z direction. Putting all of this together, we can express the final wave function after interaction with the sample (also called the object wave function, Ψ_{obj}) as

$$\Psi_{\text{obj}} = \Psi_o e^{i\sigma V_{\text{proj}}} \tag{1.17}$$

where V_{proj} is the projected potential of the sample and $\Psi_o = \psi(x, y, 0)$. In the case of a STEM probe, Ψ_o is Eq. 1.7. Eq. 1.17 is referred to as the phase-object approximation because the sample potential only modifies the phase of the initial wave function. Therefore, by measuring the phase of the exit wave (or the derivative of the phase), it is possible to measure the projected potential of the sample (or the electric field). Since the projected potential contains contributions from the nuclear charge, core electrons, and valence electrons, measuring the phase can reveal many electronic properties of the material. The key assumption in this process was that the sample was thin enough to ignore propagation. This is generally true when the sample is about 5 nm thick along the beam direction, but as will

be explored in Ch. 2, it can depend on a variety of factors.

From Eq. 1.14 and Eq. 1.17, we can also readily identify a method for calculating the exit wave function in arbitrarily thick samples. The thick sample is first divided into thin slices and the projected potential is calculated for each slice. Each slice is considered infinity thin and all the slices are separated by regions of free space equal to the slice thickness. Starting with an initial wave function, the wave function at arbitrary thickness can be calculated by repeatedly applying the propagation operator through free space and then the transmission operator at each slice. This process is called the multislice method and is now widely used to implement electron microscopy imaging simulations [72].

1.3 Imaging electronic properties in S/TEM and applications to ferroelectrics

Electrical and magnetic properties are of critical importance for materials with applications in semiconductor devices, batteries, photovoltaics, and sensors. For example, the electric field configuration can influence switching behavior, electron-hole pair separation, and the local conductivity. Charge accumulation in specific regions also plays an important role in functional properties as carrier types and concentrations can be varied with an applied field. Many of these properties only occur locally at atomically sharp interfaces, domain walls, or grain boundaries or at defects [18, 31–33, 46, 73]. There are a variety of techniques currently available to image or measure electronic properties in materials, including analysis of conventional images, detailed examination of the fine structure of x-ray edges in EELS, and phase reconstruction methods.

In ferroelectrics, the structural polarization plays a large role in determining the electronic properties and both DF TEM imaging and HAADF imaging provide methods for studying

the domain structure. As explained above, different ferroelectric domains slightly alater the diffraction condition, which generates contrast between domains. This can be used to visualize the domain structure, but not the arrangement of dipoles in individual unit cells [44]. Atomic resolution HRTEM or STEM images can resolve individual atomic columns in perovskite unit cells, so the polarization can be measured based on the position of individual atomic columns. In the images, atomic columns are typically fit with 2D gaussian to determine the position and then the average position is calculated for the anions/cations; the displacement between the center of the cations and anions represents dipole of the unit cell [44]. Typically the oxygen anions in perovskite materials are only visible in HRTEM, ABF, or other specialized imaging modes [44, 64]. However, in perovskite ferroelectrics, this technique is most often used to estimate the polarization based on only the displacement of the B-site from the adjacent four A-site atoms since the B-site displacement can be linearly related to the polarization in most cases [44]. Polarization mapping using atomic resolution HAADF images has been widely adopted to study polarization structures in ferroelectrics [18, 35, 50–52, 73, 74]. However, polarization mapping is not a direct measurement of the local electric field or charge distribution; both must be inferred from the polarization pattern. This is effective for building qualitative arguments or explanations for observations, but it is difficult to use for making quantitative measurements of the local charge or electric field.

Electron energy-loss spectroscopy does offer significant information regarding the electronic structure of materials through near or extended edge fine structure analysis and it provides the highest resolution of conventional imaging and spectroscopic methods sensitive to electromagnetic properties [75]. The core-loss edges in EELS are generated by the same x-ray emitting excitations that are generally studied in x-ray absorption spectroscopy (XAS). As a result, much of the analysis of edge fine structure that has been developed for XAS can also be applied to EELS [76] to determine the oxidation state of an element. Considering EELS can achieve atomic resolution in an aberration-corrected STEM [77], this can be used

to measure the charge distribution with atomic resolution. Changes in peak width, height, and area in the edge fine structure are all associated with different modifications to the bonding environment of the associated element [78–80]. Qualitatively, these changes can be taken in aggregate to correlate the shape of different spectra with different valence states by comparing spectra from the sample with reference spectra from samples with known valence states. Multiple linear least-squares fitting can also be used to fit experimental data with a linear combination of reference spectra taken from samples with known valence states [81]. The fine structure can also be analyzed quantitatively with advanced background subtraction and peak fitting methods to correlate specific spectral features with different valence states. Both qualitative and quantitative methods can be used to demonstrate charge accumulation and local changes to the electronic properties of a material [75]. In addition, EELS is generally applicable to almost all sample types and geometries. Spectroscopic techniques generally require a strong electron dose but advances in direct electron detectors have made it possible to study increasingly beam-sensitive materials. However, similar to polarization mapping, valence state and charge distribution measurements are correlative and not direct measurements of the charge or electric field. Correlations between bonding structure and valence state do not always present a clear picture.

In contrast to the methods described above, techniques based on phase reconstruction can be used to directly image the electric potential in a sample. In weakly interacting samples, the projected electrostatic (or vector potential in the presence of a magnetic field) will be encoded in the phase of the electron wave function according to the phase-object approximation [53, 57, 68]. However, measuring the phase is not an easy task. Since cameras and detectors can only record the intensity of the electron wave function, the phase information is lost in any conventional image. Holography is one of the primary methods for recovering the phase of the electron beam in TEM. In off-axis holography, part of the electron beam is directed through the sample and another part is directed through vacuum to act as a reference wave. The segment of the beam that interacts with the sample will have a shifted phase

compared to the reference wave. Using a biprism inside the electron microscopes projector lens system, an interference pattern between these two waves is generated and projected onto the detector. The phase can then be determined based on the interference pattern [57, 82]. In in-line holography, a focal series of images from the same region are collected; changing the the defocus introduces an additional phase shift between each image. An iterative algorithm can then be used to solve for the phase from the focal series images [83]. TEM holography has generally been used for lower resolution applications, studying the potential semiconductor devices or magnetic materials [61, 84]. However, it has been used recently in high resolution applications to study the 2DEG at the $LaAlO_3/SrTiO_3$ interface and the properties of vacancies in MoS_2 [85, 86]. To satisfy the weakly interacting condition required for holography, samples must generally be very thin (less than 5 nm) to avoid dynamical scattering. This is achievable with mechanically polished samples, but can still limit the technique's application. For off-axis holography, the requirement of an adjacent vacuum region limits the sample geometries which can be used. For in-line holography, the iterative reconstruction can be computationally intensive compared to other methods which do not require such calculations.

Other phase reconstruction methods based on STEM imaging include STEM holography and ptychography [87–91]. In ptychography, the phase of the electron probe is reconstructed based on a series of CBED patterns collected from probe positions with overlapping interaction volumes. The technique was originally developed for super-resolution imaging [92] and the technique has seen significant advancements in this regard, with the development of iterative algorithms for phase retrieval [89–91]. Ptychography has also been used extensively for low dose imaging and light element imaging [93–96]. Ptychography has the potential to be used for imaging electric properties since it is highly sensitive to the electrostatic potential, but has not been widely adopted for the task [97], likely because of its computational complexity.

A new paradigm has emerged in electronic property imaging in STEM over the last 10 years based on four-dimensional STEM (4D STEM) and an associated technique, differential phase contrast imaging (DPC). While 4D STEM relies on many of the same assumptions for weak interaction as phase reconstruction methods and the underlying physical interaction is very similar [62], imaging electronic properties with 4D STEM is significantly easier than any phase reconstruction method since it does not require an adjacent vacuum region or iterative reconstruction algorithm. The electric field from the scale of tens of manometers down to atomic resolution can be determined from 4D STEM/DPC data with a simple calculation [98, 99]. Considering these advantages over the other techniques, 4D STEM/DPC is uniquely positioned for imaging the electronic properties of ferroelectric thin films. In the subsequent chapters, we will introduce 4D STEM electric field and charge density imaging and examine its applications to a variety of ferroelectric heterostructures.

Chapter 2

4D STEM for electric field imaging

2.1 Introduction to 4D STEM and electric field imaging in STEM

Four-dimensional scanning transmission electron microscopy was developed to take advantage of the high frame rate CCD cameras and direct electron detectors that have recently become ubiquitous in the transmission electron microscopy. Instead of using the conventional annular detectors which only yield only one value per probe position per detector, a pixelated detector synchronized with the scanning probe can record an entire diffraction pattern for every probe position during the raster scan, as shown in fig. 2.1. Combining a 2D raster scan with a 2D convergent beam diffraction (CBED) pattern for each scan position results in a four-dimensional dataset, with two real-space dimensions and two momentum space dimensions. This kind of data requires more analysis to be useful than conventional STEM images, but it allows for significant flexibility in what material properties can be extracted. Whereas the parameters for conventional STEM imaging are constrained by the installed detectors, defining virtual detectors to integrate various regions of momentum space in 4D

data allows for real-space images to be generated with arbitrary inner and outer collection angles [100, 101]. Virtual detectors can also be designed with shapes that are impossible with physical detectors which enables unique dark field images that can be used to isolate specific phases [102, 103]. If the convergence angle is low enough that the diffraction disks are well separated, the local strain can also be quantitatively measured with high resolution based on the separation of the diffraction disks [104, 105]. Averaging many pixels in real space results in a position averaged CBED (PACBED) pattern that can be used to quantify the thickness [106]. 4D STEM data can also be used to determine the orientation of a single phase [106, 107].

While the techniques listed above are useful for studying a wide variety of materials and properties, they still ignore the full potential of a 4D dataset. As the charged electron beam passes through the sample, it is deflected by the electric field of the sample, as illustrated schematically in fig. 2.1a. The electric field in a material, and the charge distribution that generates the field, are of fundamental importance to a wide variety of functional properties at the micro and nanometer scale [12, 22, 108, 109]. Therefore, determining the electric field using the spatial resolution provided by a STEM probe is a valuable tool in materials science. Unlike many of the other methods available in electron microscopy for measuring electronic properties, this is a direct measurement of the electric field in the sample.

Prior to the proliferation of fast cameras, this deflection was measured using segmented conventional STEM detectors in a technique called differential phase contrast (DPC) imaging. By subtracting the signal from geometrically opposed segments, the magnitude and direction of the shift in the electron beam can be measured which yields an estimate for the local electric field. This technique was fist demonstrated by Shibata et al. to image the electric field of atomic columns in $SrTiO_3$ and in $BaTiO_3$ domains [98]. DPC has since been applied a wide variety of materials systems to reveal the internal electric field, including single gold atoms, GaN, GaAs nanowires and model semiconductor devices [110–113]. Due to the high

speed of conventional STEM detectors, (pixel times in the μs range compared to ms range for most cameras) and its sensitivity to light elements, DPC and its derivatives, such as integrated DPC (iDPC), are also effective tools for imaging beam sensitive materials [74, 114, 115]. However, DPC has several drawbacks associated with using a segmented detector instead of capturing the full diffraction pattern. Segmented detectors are insensitive to any intensity shift in the CBED pattern that takes place within a single detector segment which reduces the accuracy of the technique. In addition, intensity shifts that align with the boarders between detector segments also cannot be detected which will introduce artifacts into the final image. These issues can be mitigated by adding additional detector segments or with more complex arrangements [116], but the ultimate solution to these issues is to use a camera to capture an image of the CBED pattern, as in 4D STEM. In addition, as detector technology continues to advance, the difference in speed and sensitivity between conventional STEM detectors and cameras will continue to decline [117, 118].

In addition to resolving the issues described above, 4D STEM data also allows for the electric field to be quantified through a fairly simple calculation. A derivation of the electric field based on 4D STEM data will be presented here based on the work of Muller-Kaspery et al. in ref. [99, 119]. In the same way that a conventional TEM diffraction pattern records the intensity of the parallel electron beam's wave function in momentum space, each CBED pattern in a 4D dataset records a momentum space image of the electron probe at each probe position. If the exit wave function of the probe at scan position $\mathbf{r_o}$ in momentum space is $\psi_{obj}(\mathbf{r_o}, \mathbf{p})$, then the intensity in the CBED pattern can be expressed as

$$I_{\mathrm{obj}}(\mathbf{r_o}, \mathbf{p}_\perp) = |\psi_{\mathrm{obj}}(\mathbf{r_o}, \mathbf{p}_\perp)|^2 \tag{2.1}$$

We can utilize this to calculate the electric field in the sample [99, 119]. Note that $\mathbf{p}_\perp$ here is only in the direction transverse to the electron beam, any change in momentum along the beam direction cannot be detected. In classical physics, the electric field is related to the

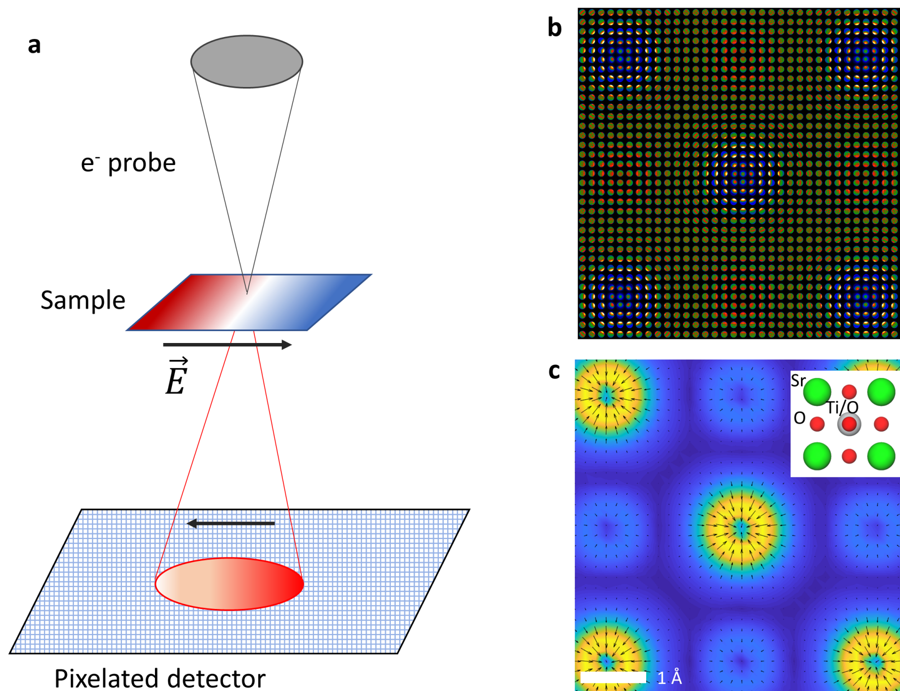

Figure 2.1: **4D STEM/Scanning Diffraction.** **a**, A diagram of the microscope configuration used for collecting 4D STEM data. **b**, Simulated CBED patterns from a $SrTiO_3$ unit cell. **c**, The momentum transfer calculated from simulated scanning diffraction data; the color shows the magnitude of the momentum transfer vector. The inset shows the (100) projection of $SrTiO_3$.

change in momentum via the Lorentz force. According to Ehrenfests theorem, the quantum mechanical expectation values can be substituted into the classical expression without issue. Therefore, the change in momentum of the probe can be expressed in terms of the electric field in the sample as

$$\frac{d\langle \mathbf{p}_\perp \rangle}{dt} = -e\langle \mathbf{E}_\perp \rangle \tag{2.2}$$

where e is the electron charge. The change in time (dt) on the bottom can be rewritten in terms of the speed of the electrons along the beam direction (v) and the thickness along the beam direction (dz) such that $dt = dz/v$. If we use this substitution and then rearrange Eq. 2.2, the result is

$$d\langle \mathbf{p}_\perp \rangle = -\frac{e}{v}\langle \mathbf{E}_\perp \rangle dz \tag{2.3}$$

Starting with the left side of this equation, integrating from the initial state of the probe to the final state of the probe this side simply yields the change in the expectation value of the probe's momentum, also called the momentum transfer. For the sake of simplicity, we will assume the probe is perfectly symmetric, so the initial momentum expectation value is zero and the momentum transfer is equal to the final momentum. However, this is not exactly true in experiment due to lens aberrations; we will address to this issue later when discussing analysis of experimental data. The momentum transfer of a probe at position $\mathbf{r_o}$ can be expressed as

$$\langle \mathbf{p}_\perp \rangle(\mathbf{r_o}) = \int \psi^*_{\text{obj}}(\mathbf{r_o}, \mathbf{p}_\perp)\ \hat{\mathbf{p}}_\perp\ \psi_{\text{obj}}(\mathbf{r_o}, \mathbf{p}_\perp) d^2p \tag{2.4}$$

where $\hat{\mathbf{p}}_\perp$ is the momentum operator. Since we're integrating in momentum space, $\hat{\mathbf{p}}_\perp$ is

just the momentum coordinate, $\mathbf{p}$, and the integral can be simplified to

$$\langle \mathbf{p}_\perp \rangle(\mathbf{r_o}) = \int \mathbf{p}_\perp \, |\psi_{\text{obj}}(\mathbf{r_o}, \mathbf{p}_\perp)|^2 d^2p \tag{2.5}$$

$$= \int \mathbf{p}_\perp \, I_{\text{obj}}(\mathbf{r_o}, \mathbf{p}_\perp) d^2p \tag{2.6}$$

Based on Eq. 2.6, we can see now that the momentum transfer is equivalent to calculating the center of mass (COM) of the CBED pattern. Calculating the COM for every probe position ($\mathbf{r_o}$) allows us to construct a vector field over the scanned area.

The right side of Eq. 2.3 is more difficult to resolve. The expectation value of the electric field at position $\mathbf{r_o}$ depends on the 3D probe intensity, $I(\mathbf{r}_\perp - \mathbf{r_o}, z)$, and the 3D electric field distribution inside the sample itself. This can be expressed as

$$\langle \mathbf{E}_\perp \rangle = \frac{1}{\Delta z} \int_{\Delta z} \int \mathbf{E}(\mathbf{r}_\perp, z) I(\mathbf{r}_\perp - \mathbf{r_o}, z) \; d^2r \; dz \tag{2.7}$$

where Δz is the thickness of the sample. Solving Eq. 2.7 exactly would require a-priori knowledge of the electric field in the sample and the intensity of the probe as it propagates through the sample. However, we can solve it if we assume that the electron probe is small compared to the length scale over which the electric field varies and does not broaden as it traverses the sample; then $I(\mathbf{r}_\perp - \mathbf{r_o}, z)$ becomes a delta function and the z-dependence can be removed. Then the integrals can be simplified so that it is a simple projection of the electric field. If we substitute the projected electric field into Eq. 2.3, then the result is

$$-\frac{v}{e} \langle \mathbf{p}_\perp \rangle(\mathbf{r_o}) = \Delta z \langle \mathbf{E}_\perp \rangle_p(\mathbf{r_o}) \tag{2.8}$$

$$-\frac{v}{e \, \Delta z} \langle \mathbf{p}_\perp \rangle(\mathbf{r_o}) = \langle \mathbf{E}_\perp \rangle_p(\mathbf{r_o}) \tag{2.9}$$

where $\langle \mathbf{E}_\perp \rangle_p$ is now the average projected electric field of the sample. The same result can also be achieved if the probe's interaction with the sample is modeled with the phase-object

approximation. For completeness, a derivation of the electric field in terms of the momentum transfer based on the phase object approximation is presented appendix A.

Eq. 2.9 is an especially useful result because the electric field at each probe position is linearly proportional to the momentum transfer/COM of the corresponding CBED pattern in the 4D dataset. An example of a simulated 4D STEM dataset from within a $SrTiO_3$ unit cell is shown in fig. 2.1b. The atomic positions of all nuclei(Sr, Ti, and O) are visible as the intensity in the surrounding CBED patterns are all biased towards the nucleus. Fig. 2.1c shows a vector map of the corresponding momentum transfer calculated from each CBED pattern in fig. 2.1b; the corresponding electric field vectors would simply point in the opposite direction. This approach to quantifying the electric field using 4D STEM data has been applied to variety of materials, including 2D materials [120, 121], GaN/AlN nanowires [122, 123], oxide ferroelectrics [124, 125], and semiconductor devices [126].

Although the direct imaging of electric fields with 4D STEM has found many applications, the assumptions required to reach the simple expression in Eq. 2.9 are quite restrictive. Going back to Eq. 2.7, we can see that the electric field measured with this method is actually the electric field of the sample convolved with the shape of the incident electron probe. This is illustrated in fig. 2.2 where a the electric field derived directly from the projected potential of the STO unit cell is convolved with the intensity profile of a 300kV electron probe with 32 mrad convergence angle and no aberration. After convolution, the electric field profile is spread out significantly and matches most closely in regions with weak electric field. Since this effect is a manifestation of the fundamental spatial resolution of the electron probe, the main avenues for minimizing the divergence between the true electric field and the measured electric field can only come from reducing the probe size through better aberration correction or full exit wave reconstruction; the former requires further development of electron optics technology and the latter is computationally intensive.

However, in addition to the probe size, there are several other factors that can influence

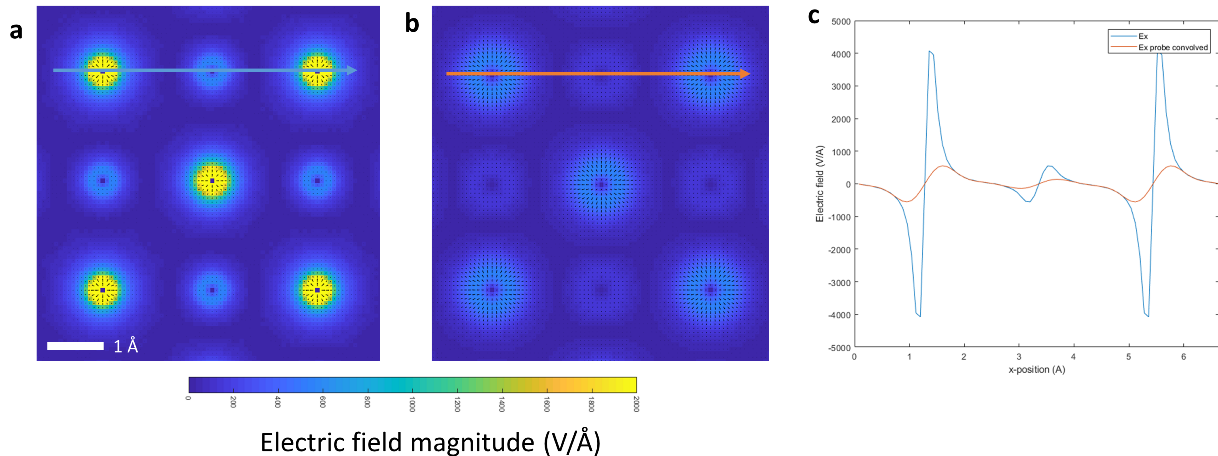

Figure 2.2: **Effect of probe size on electric field measurement.** **a**, The electric field calculated within an $SrTiO_3$ unit cell calculated from the projected potential used in simulation. **b**, The electric field in **a** convolved with the initial probe shape for a 300kv probe with no aberration. The arrows indicate the position of line profiles. **c**, Line profiles of the x-component of the electric field. Convolution with the electron probe has a significant influence on the electric field shape and magnitude close to nuclear cores; but the line profiles show that the electric field matches closely in regions with weaker electric field.

electric field or momentum transfer measured with 4D STEM which can be controlled more easily in experiments. To ensure the probe does not broaden significantly as it transmits through the sample, the thickness along the beam direction must generally be small, on the order of 5 nm, based on previous publications [99, 119]. Beyond 5 nm, the linear relationship between the momentum transfer and the electric field begins to break down, so the simple center of weight calculations used to determine the electric field becomes less quantitative. TEM specimens are generally fabricated with a wedge shape, so a range of regions with varying thickness may be available on a given sample. But high quality regions with thickness close 5 nm can still be difficult to find in bulk samples and introducing more complex structures, such as thin films or superlattices can make finding an appropriate region even more difficult. Therefore, understanding how changes in sample thickness affect the momentum transfer measured in 4D STEM is important to expanding the types of samples that can be studied with 4D STEM electric field imaging.

The probe defocus can also heavily influence the momentum transfer measured from 4D

STEM data. In conventional HAADF imaging, focusing the probe on the top surface of the sample produces the maximum contrast in the resulting image. But when capturing BF images, the the defocus must be adjusted slightly below the surface of the sample to maximize contrast. Since the defocus is one of the easiest parameters to control during experiment and also has a profound effect on the final images, understanding how momentum transfer depends on probe defocus is also important to optimizing 4D STEM data.

In the subsequent sections of this chapter, the effects of sample thickness, probe defocus, on the relationship between the momentum transfer measured via 4D STEM and the electric field in the sample are studied systematically through both experiment and STEM image simulation using $SrTiO_3$ as a model system. For these sections, we will focus on the relationship described by Eq. 2.8, which shows that the momentum transfer should grow linearly with sample thickness under the approximations described above. Focusing on Eq. 2.8 makes it quite easy to see when these approximations begin to breakdown by looking at how the magnitude of the momentum transfer changes as a function of sample thickness. We collected a complete set of momentum transfer images from a wedge sample with thickness ranging from 5 nm up to 22 nm in experiment, using PACBED to quantify the thickness in each region [106]. Our results cohesively show that by using appropriate defocus, electric field imaging can maintain quantitative relationship with sample thickness up to 5 nm. In samples with even larger thickness, while quantitative measurement on the electric field starts to fail, qualitatively, 4D STEM can still generate an image that is representative of the electric field in the sample.

2.2 Experiments from bulk $SrTiO_3$

$SrTiO_3$ is an ideal model system because the cubic perovskite structure should produce a symmetric electric field pattern at the atomic scale. This simple pattern also allows

us to compare the momentum transfer pattern measured from diffraction data with the internal electric field. In fig. 2.1c, the momentum transfer measured near each atomic site is rotationally symmetric and points radially inward towards the nucleus; the electric field map is identical but points radially outwards. Close to nuclei, we expect the electric field to resemble that of a point charge due to the strong positive nuclear charge. Overall, the electric field should also reflect the four-fold symmetry of the unit cell.

Experimental 4D STEM data was collected on a Gatan Oneview camera running at 300 fps to minimize scanning noise and drift during acquisition. Combined with a step size of 0.2 Å, this enabled us to acquire high resolution data that accurately shows the coulomb field surrounding each atomic site. To account for the initial momentum of the electron probe and to remove any overall shift in the CBED pattern affecting the entire dataset, the average COM position of all CBED patterns is chosen as the reference position instead of the geometric center of the CBED patterns. The momentum transfer vector is then the difference between the reference position and the COM of each CBED pattern.

Although previous 4D STEM studies based on simulation have predicted that the range of sample thicknesses offering interpretable images for measuring electric field is very small [99, 119] we found that this same radial and rotationally symmetric pattern persists even for samples with thickness up to 20 nm. Fig. 2.3 shows examples of momentum transfer data collected from an STO wedge sample where the thickness increases gradually when moving further away from the edge of the sample (towards the bottom of the image). The thickness in this region was determined with PACBED measurements [106]. A series of high-resolution scanning diffraction measurements were collected at varying thicknesses. As shown in fig. 2.3b-e, in qualitative terms, the pattern of the momentum transfer surrounding each atomic site does not change with increasing sample thickness. Irregularities in the shape of the momentum transfer pattern are mostly random and attributable to scanning noise while consistent artifacts, like the slight bias on the top of the atoms in figs. 2.3c

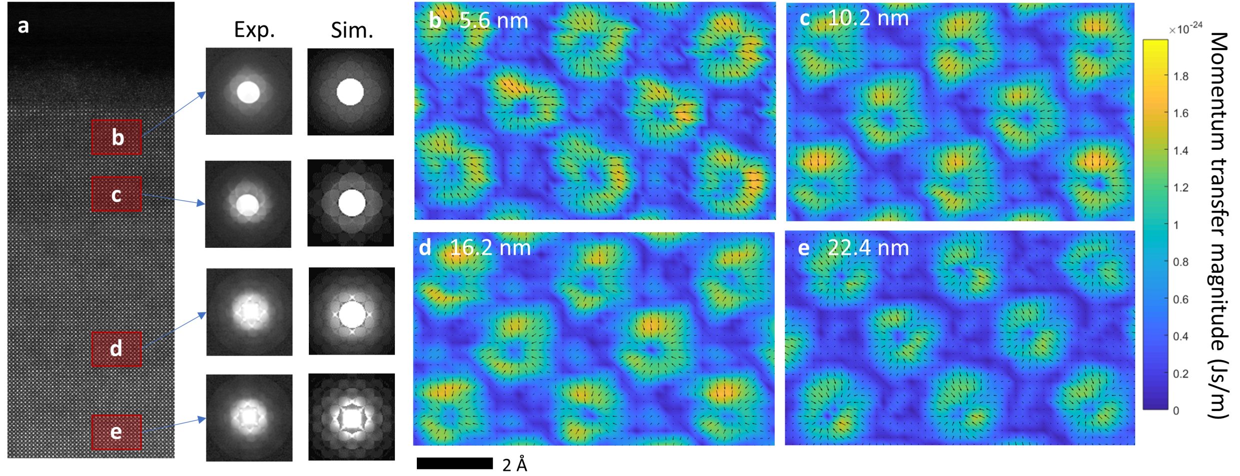

Figure 2.3: **Experimental Variation with Sample Thickness. a**, HAADF image of an $SrTiO_3$ cross-section sample with PACBED measurements from experiment and simulation to determine the local thickness. The sample is thinnest close to the vacuum region and grows thicker further away from the edge. The electric field was measured in the regions highlighted in red. The sample thickness in each region was measured to be: 5.6 nm (**b**), 10.8 nm(**c**), 16.2 nm (**d**), and 22.4 nm (**e**). The electric field points radially outward and appears mostly rotationally symmetric for all thicknesses.

and d, can be attributed to slight off-axis tilt. Although this is not the expected result from available simulated works [99, 119], it indicates that the technique is more robust to changes in thickness than previously expected. In addition, as shown by the color scale of the background, the magnitude of the momentum transfer does not change with sample thickness between 5.6 – 22.4 nm. This indicates that the momentum transfer does not increase linearly with the sample thickness in this range.

By taking line profiles of the momentum transfer, we can see how it changes as a function of sample thickness. Fig. 2.4 shows the average line profile of the momentum transfer across Sr atoms from regions with several different thicknesses, decreasing from top to bottom. The line profiles are drawn from the same data that is shown in fig. 2.3. The low momentum transfer in the central valley results from the small value of the projected electric field in the imaging plane, however the value is still non-zero due to the spatial extent of the electron probe. As the sample thickness increases, the overall profile flattens.

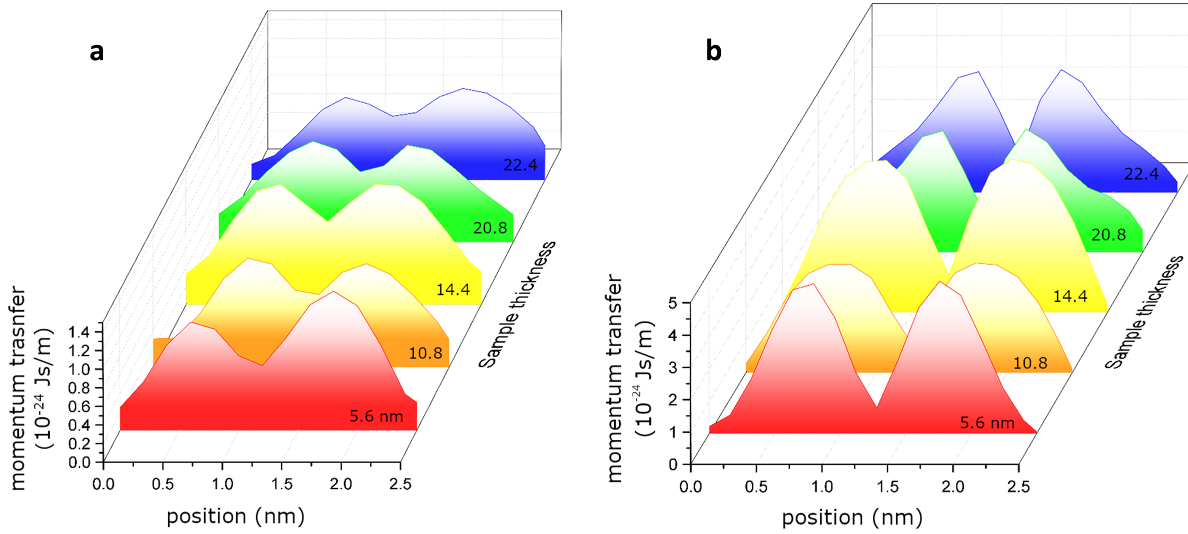

Figure 2.4: **Momentum Transfer Line Profiles.** **a**, Experimental line profiles showing the magnitude of the momentum transfer along horizontal line profiles across Sr atoms. **b**, Line profiles of the momentum transfer magnitude for simulated data. The line profiles are in increasing order of thickness from bottom to top. The profiles are separated on the vertical axis for clarity. Overall broadening of the peaks is visible in both the simulated and experimental data. However, the overall shape of the experimental line profiles is fairly consistent while the shape of the peaks in the simulation data changes noticeably.

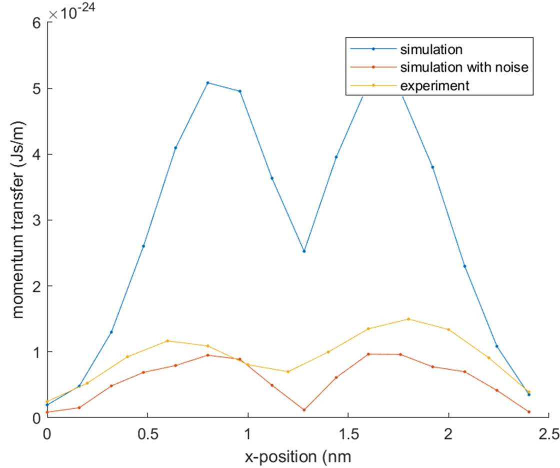

Figure 2.5: **Camera noise effect.** Line profiles of the momentum transfer magnitude across a Sr atom for a 5.6nm sample. Gaussian noise added to the simulated 4D data set significantly reduces the magnitude of the momentum transfer, making it more comparable to experiment.

We also conducted STEM simulations, shown in fig. 2.4b, to compare with experiment. The same trends observed in the experimental line profiles are also observed in the simulated data; an overall flattening of the electric field and broadening of the peaks is present on either side of the atom. However, it is noteworthy that the simulated momentum transfer is an order of magnitude higher than experimental. This is likely due to inelastic scattering and electronic noise from the camera which is present in the CBED images collected in experiment. This noise can completely obscure higher order diffraction disks and smooths out intensity variations which would otherwise make significant contributions the momentum transfer measured from the CBED pattern. Quantifying the noise model from experimental data and applying it to simulated data reduces the magnitude of the measured momentum transfer to be comparable to experiment, as shown in fig. 2.5.

2.3 Examining thickness and defocus dependence in $SrTiO_3$

To better appreciate the experimental results that electric field can be mapped with even thicker samples, we studied the effects of changing the focus of the electron probe on the measured momentum transfer. We examined three probe conditions: a probe focused on the top surface, a probe focused in the middle of the sample, and a probe focused at the bottom surface of the sample. For a 2 nm sample, shown in fig. 2.6a, the momentum transfer always points radially inward toward the nucleus, as would be expected from the strong positive charge concentrated in the nucleus, regardless of the probe conditions. The simulated momentum transfer for an 8nm sample with the probe focused in the middle of the sample, fig. 2.6b, also shows a radially symmetric pattern, but the region immediately surrounding the nucleus exhibits weak momentum transfer when compared to the 2 nm sample. When the probe is focused on the top surface, fig. 2.6c, the momentum transfer close to the nucleus reverses direction and the overall magnitude is much lower in comparison to other cases. This change in sign of the momentum transfer makes the top focused condition the least suitable for imaging the electric field. The momentum transfer of the probe focused on the bottom surface, fig. 2.6d, more closely resembles the middle-focus case, but with a smaller region of low momentum transfer surrounding the nucleus.

As the final momentum transfer of the probe is influenced by the entire path of the electrons inside the sample, we reconstructed the electron propagation in real space from the position marked in 2.6a by profiling the probe wave function from each slice in 3D, and projecting it along the STO (010) direction. Examining how the probe's intensity is distributed in real space can give us insight into how the probe is changing as it passes through the sample. In all three cases, shown in figs. 2.7a-c, the probe initially shifts to the right due to the electric field of the nearby Sr atom pulling the probe closer. In addition, all three probes show some

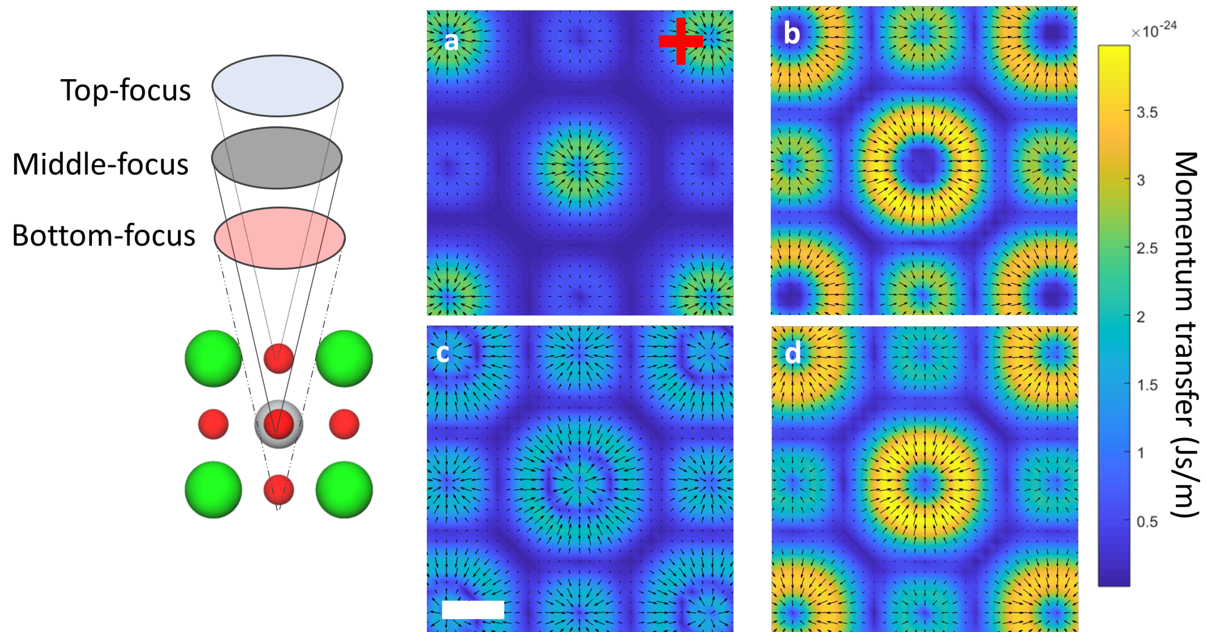

Figure 2.6: **Simulated Momentum Transfer. a**, Simulated momentum transfer from a 2 nm sample. **b-d**, The momentum transfer calculated from simulated 4D STEM data with the probe focused on the top surface (**b**), in the center of the sample (**c**), and focused on the bottom surface (**d**) for an 8nm sample. The middle-focus and bottom-focus conditions give the most accurate results. The scale bar is 1 Å.

intensity shifting back to the left before the probe reaches the bottom surface of the sample. Line profiles of the probe at three depths, 0 nm, 6 nm, and 8 nm, are shown in figs. 2.7d-f; 6 nm depth was highlighted because all three probes exhibit maximum displacement near this depth. The peak of the middle-focus probe shifts right 0.31 Å, the top-focus probe shifts 0.23 Å, and the bottom-focus probe shifts 0.39 Å between the top surface and 6nm into the sample. From this point, the behavior of the three cases diverges; the top-focus probe shifts as one peak back to the left by 0.23 Å, while the middle-focus and bottom-focus probes split into two peaks. These secondary peaks emerge directly under the original probe position. In the case of the middle-focus probe, the intensity of this second peak is slightly larger than the shifted peak; this is likely the cause of the large region of low momentum transfer surrounding the nucleus in fig. 2.6b. For the bottom-focus probe, the secondary peak is of much weaker intensity, translating to a larger measured momentum transfer near the nucleus in fig. 2.6d.

We also examined how closely equation 2.8 matches with the measured electric field/momentum transfer in simulation. Based on Eq. 2.8, for a single point where the electric field is constant, the momentum transfer should scale linearly with the thickness of the sample. To study this, we sampled the momentum transfer from a series of three points near a Sr column and plotted it as a function of sample thickness, when the electron probe was focused at all three positions, for a sample of thickness 15 nm. In this example, only the x-momentum transfer is shown because the y-momentum transfer should be minimal at the position chosen, directly to the left of the atomic column. Fig. 2.8a shows the momentum transfer of the probe which is focused in the middle of the sample; the blue, red, and yellow curves are for probe positions shown in the inset. Figs. 2.8b and c show the momentum transfer at the same positions, but with the probe focused on the top and bottom surfaces, respectively. In both Figs. 2.8a and 2.8b, the momentum transfer measured closest to the nucleus initially increases linearly before reaching a turning point, where the relationship described by Eq. 2.8 is no longer strictly valid. However, the turning point for the middle-focus beam

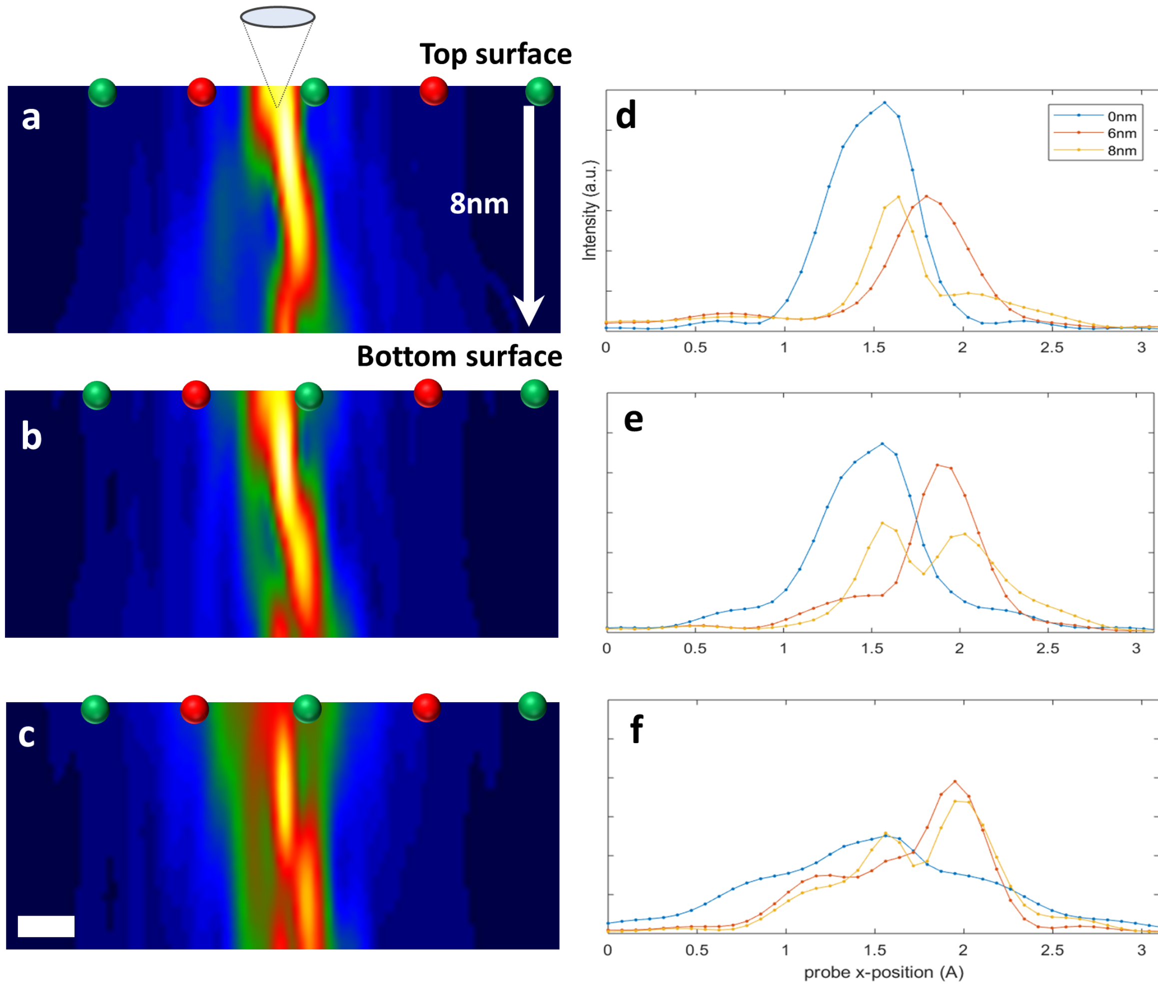

Figure 2.7: **Propagation of the Electron Probe.** The trajectory of the electron probe was examined in top-focus (**a**), middle-focus (**b**), and bottom-focus (**c**) at the position marked by the red cross in fig. 2.6. Scale bar is 1 Å in horizontal direction. Red dots are oxygen atoms, green are Sr. **d-f**, show line profiles of the probe intensity at depths of 0nm, 6nm and 8nm for the top-focus, middle-focused, and bottom-focused probes, respectively.

occurs later than that of the top-focus beam. Similar to the results found in ref. [99, 119], we found that the momentum transfer grows linearly with thickness for thin samples, but this relationship breaks down when the sample is thicker than about 6 nm. In addition, the middle-focus momentum transfer never dips below zero, which would indicate a switch in the direction; this is important for qualitative accuracy of the electric field near the nucleus. For the middle-focus probe, the oscillations of the momentum transfer are weakened as the probe position moves further from the atomic column into regions with weaker field; at points between atomic columns (yellow data), the momentum transfer is linear through the entire thickness range. By fitting the yellow data points in the middle-focus condition as a linear function of the thickness, as shown in fig. 2.8a, we calculate the electric field in the interatomic region to be $\langle E_x \rangle = 156$ V/nm. The fit results in a reduced-R^2 value of 0.97, indicating a good fit. Based on the projected potential used in our simulations, we can directly calculate the true value of the electric field at this same position to be 195 V/nm, about 20% different from the value measured from the simulated 4D STEM data.

The momentum transfer from the bottom-focus probe, fig. 2.8c, shows markedly different results from the top- and middle-focused probes. The under-focus probe does not interact significantly with the sample's electric field until it has traversed several nanometers of the sample. The momentum transfer does begin growing linearly in the bottom 4 nm of the sample. This trend holds for all probe positions we tested. Although the under-focus probe does not follow the simple linear relationship between the momentum transfer and the electric field through the entire sample, as the probe exits the sample, where we can measure it, the relative magnitude of the momentum transfer at all probe positions matches what is expected from the relative strength of the electric field. This behavior is likely due to the reduced interaction volume of the bottom-focused probe. In this condition, the beam entering the sample is spread over a larger area, so the interaction with the electric field in the sample does not result in a coherent change in the momentum when summed over the entire region covered by the probe. However, as the probe becomes more focused towards

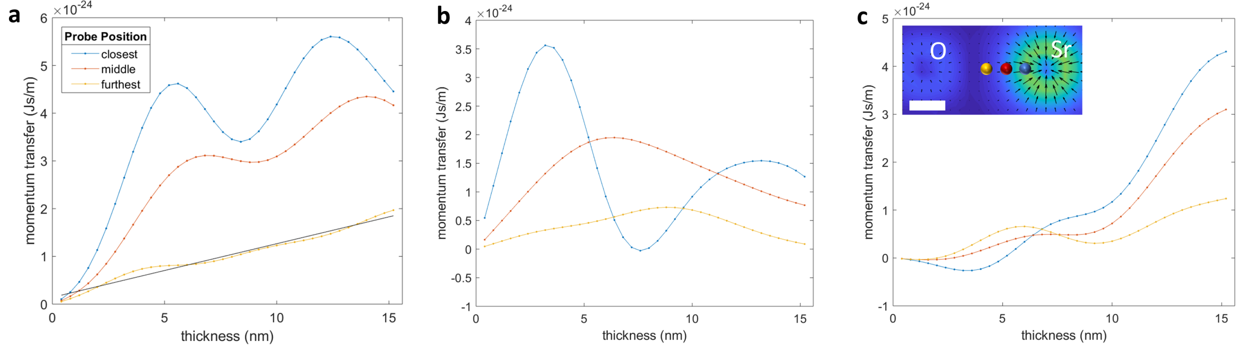

Figure 2.8: **Thickness Dependence of Momentum Transfer.** **a**, The momentum transfer calculated from simulated 4D STEM data as a function of sample thickness for 3 positions near a Sr column with the probe focused in the center of the sample. The total thickness of the sample is 15.2 nm. The momentum transfer at the furthest position has been fit with a linear model to determine the electric field at that point. **b**, **c**, The momentum transfer for the same positions when the probe is focused at the top and bottom surfaces of the sample. The positions where the momentum transfer is sampled in the blue, red, and yellow curves are shown in the inset with the correspondingly colored dots. Notice in **a** the three curves always maintain the correct ordering with the position closest to the atomic column always showing the largest momentum transfer. Scale bar in the inset is 0.5 Å.

the bottom of the sample, the region interacting with the probe becomes smaller and the force exerted on the probe over the entire interaction volume adds coherently to generate a measurable change in the momentum. Overall, these results indicate that using a bottom-focused probe will provide qualitatively correct results for the electric field calculated from momentum transfer even for samples thicker than 5 nm.

In all three cases illustrated in fig. 2.8, beam broadening is the cause of the non-linear changes of the momentum transfer. The broadening of the electron probe in thicker samples increases the interaction volume, so the electric field measured from the momentum transfer is effectively averaged over a much larger area. This results in the non-linear response of the momentum transfer for samples thicker than 6 nm seen in fig. 2.8. It has been shown that beam broadening, caused by both propagation through thick samples and large convergence angles, will increase the error in the measured electric field [119].

In summary, to maintain an accurate quantitative relationship between momentum transfer

and electric field in all regions of the sample, the thickness should be close to 5 nm when the beam is focused near the middle of the sample. But electric field mapping has better tolerance in inter-atomic positions, where the electric field is weak, based on the accurate fit of the momentum transfer as a function of thickness observed in simulation when the beam is focused in the middle of the sample. If the beam is focused on the top surface, the sample should be limited to 4 nm thickness; beyond 4 nm, measuring the electric field based on the momentum transfer will not yield qualitatively, let alone quantitatively, accurate results. If the probe is focused on the bottom surface, quantitative calculation of the electric field from the momentum transfer will require additional modeling to be accurately interpreted because the probe behaves as if it is interacting with a sample of reduced effective thickness. However, this also means electric field mapping with a bottom-focused probe in thicker samples tends to yield qualitatively accurate results which maintain the relative magnitude and direction of the electric field. Therefore, we propose using middle-focused or bottom-focused probe conditions for future atomic resolution studies of electric field using 4D STEM.

2.4 Conclusion

Based on these results from simulation, we can understand why it is possible to still see predictable electric field from experimental samples that are more than a few nanometers thick. The simulations show that the middle-focus and bottom-focus probes both produce momentum transfer that fits with expectations for the electric field within the sample. The momentum transfer points radially inward and is rotationally symmetric around each atomic column. In experiment, the data is generally collected between the top-focus and middle-focus condition because this condition is relatively easy to achieve by maximizing the contrast in the HAADF image. Intentionally moving the focus the electron probe down by a few nanometers would be better when collecting data from thicker samples.

In conclusion, we have presented experimental evidence that momentum transfer calculated from 4D STEM data can provide interpretable results representative of the electric field for samples up to 15-20 nm in thickness. Multi-slice STEM simulations were used to generate 4D diffraction data under varying probe conditions and sample thicknesses to better understand the experimental result. The simulations showed that the defocus of the probe can have a significant effect on the final momentum transfer measured as the probe exits the sample. Based on our results from both experiment and simulation, by collecting the diffraction data with the probe in either middle-focus or bottom-focus, we can avoid the most glaring artifacts associated with larger sample thicknesses; using this approach, the electric field will still agree qualitatively with expected electric field in the sample, especially since 4D STEM can efficiently measure the electric field in regions between atoms where the probe-field interaction is weaker.

Chapter 3

4D STEM applied to the $BiFeO_3$-$SrTiO_3$ interface

3.1 Introduction

Directly visualizing the electron distribution in solids and molecules can broadly advance science, as nearly all physical properties of materials are determined by the electron charge rearrangement between nuclei when atoms aggregate together. However, observing electrons in materials at high spatial resolution is not routine. Indirectly measuring charge density of bulk materials is possible through X-ray or electron diffraction techniques by fitting their structure factors [127–133]. This method is called quantum crystallography when referring to x-ray diffraction or quantitative convergent beam electron diffraction (QCBED) for electron diffraction. Both quantum crystallography and QCBED are capable of measuring low order structure factors that are sensitive to the distribution of valence electrons that take part in bonding in with high accuracy. This is done by collecting high quality diffraction data from pristine samples and then using dynamical scattering simulations to find the structure

factor values that result in diffraction patterns matching with experimental data. As a result, it is possible to measure the bonding electron distribution in materials to a point where it is comparable with density functional theory calculations [127–129, 132, 133]. But these methods require that the sample is homogeneous within the illuminated area; this can be quite restrictive in the case of x-ray diffraction due to the relatively weak interaction between x-rays and materials and the difficulty in focusing x-ray beams. With a TEM, the electron beam can be steered and focused easily, so finding a pristine, defect free, region is not difficult. However, the simulation process is still computationally intensive. This makes quantum crystallography and QCBED ill-suited for studying irregular structures, such as interfaces and defects, where interesting properties often emerge. Recent development of scanning tunneling microscopy (STM) and atomic force microscopy (AFM) allows us to see chemical bonds, but only on surfaces [134–136]. Thus, it remains a great challenge to resolve the charge density in nanostructures and functional materials with imperfect crystalline structures, especially those with defects, interfaces, or boundaries where new physics emerges.

However, 4D STEM and DPC imaging offer a fairly simple method for deriving the charge distribution at atomic scale. As shown in Ch. 2, 4D STEM and DPC can be used to measure the electric field of individual atomic columns using aberration-corrected STEM. Given a detailed map of the projected electric field, $\mathbf{E}$, the associated projected charge density map is given by Gauss's law

$$\nabla \cdot \mathbf{E} = \frac{\rho}{\epsilon_o} \tag{3.1}$$

where ρ is the charge density and ϵ_o is the permitivity of free space [137]. Although Gauss's law is defined in 3D, it is equally applicable to the projected electric field and charge density in 2D. Since this calculation relies only on the electric field map, which is calculated directly from each CBED pattern in the 4D dataset, the process of acquiring a charge density image is very simple compared to quantum crystallography and QCBED. In addition, there are no

constraints against the heterogeneous samples since the analysis process does not make any assumption about the structure itself. The only constraint is that the sample is thin enough to avoid multiple scattering or beam broadening as the electron probe traverses the sample.

This technique has been used to study the atomic scale charge distribution of a variety of materials and heterostructures. DPC imaging has been used to study the charge distribution of Ga atoms in GaN [111]. In this case, both experimental and simulation data demonstrated that the charge density image was sensetive to both the nuclear and electron charge surrounding the Ga and N atoms. 4D STEM has also been used to image the charge density near MoS_2 monolayer-bilayer interfaces and identify the structure of the bilayer termination [120]. Since the electron probe can reach sub-Å width in AC-STEM, this technique is also capable of imaging electron charge distribution in interatomic regions. Charge accumulation inside conductive linear defects in MoS_2 and WSe_2 was imaged by Fang et al. and showed good agreement with the results from first principles calculations[121]. More recently, Zheng, Feng, and Hatchel et al., used 4D STEM to study the inhomogeneity of anionic electrons in Y_5Si_3, an electride material [138] where clusters of electrons occupy interstitial positions and act as anions.

This chapter will describe the application of real-space charge density imaging (RSCDI), towards perovskite materials by drawing comparisons between the insulator $SrTiO_3$ (STO), ferroelectric $BiFeO_3$ (BFO), and a BFO-STO interface. Using this technique, we imaged the interfacial charge distribution and ferroelectric polarization in a BFO-STO heterojunction in four dimensions, and discover charge accumulation at the interface that is induced by the penetration of the polarization field of BFO. We validate this finding through side-by-side comparison with density functional theory calculations. New techniques for quantitatively analyzing atomic resolution charge density images were also developed in this process and will be described below. Charge-density imaging advances electron microscopy from detecting atoms to imaging electron distributions, providing a new way of studying local bonding in

crystalline solids [139].

3.2 Bulk $SrTiO_3$ and $BiFeO_3$

3.2.1 Electric field map and analysis

The BFO films were grown on single crystal (100) STO surfaces by reactive-molecular beam epitaxy. The 50 nm BFO layer was deposited at a substrate temperature of 625 °C in distilled ozone (80% ozone) at a partial pressure of 1×10^{-6} Torr. TEM sample of STO and BFO thin film on STO are prepared by hand polishing followed by ion milling, to provide large, uniformly thin area transparent to electron beam.

4D STEM data was first captured from an over-milled region of the sample where the BFO film had been removed, leaving only the STO substrate. STO is a simple cubic perovskite with a projected square symmetry (fig. 3.1a). In fig. 3.1b, the high angle annular dark field (HAADF) STEM image of STO shows clearly the Sr and Ti atomic columns, while oxygen atoms cannot be seen due to its weak scattering for electrons. The 4D data was collected on a JEOL JEM-ARM300CF double aberration corrected S/TEM at 300 kV; CBED patterns were recorded with a Gatan OneView camera at the speed of 300 frames-per-second (fps), each with the size of 512x512 in pixels. A semi-convergence angle of 32 mrad was used for probe forming in imaging electric field. The scanning of the beam was synchronized with the camera using the Gatan STEMx system, with the scanning step size of 0.2 Å. The electric field was quantified from the 4D dataset with the method introduced in Ch. 2. To ensure the highest quality electric field map and subsequent charge density images, we applied per line drift correction to the 4D dataset. In detail, the sample drift along the horizontal direction is corrected by measuring the average displacement per line from a conventional fast scanned STEM image and then shifting each line of pixels back. Drift along the vertical scan direction

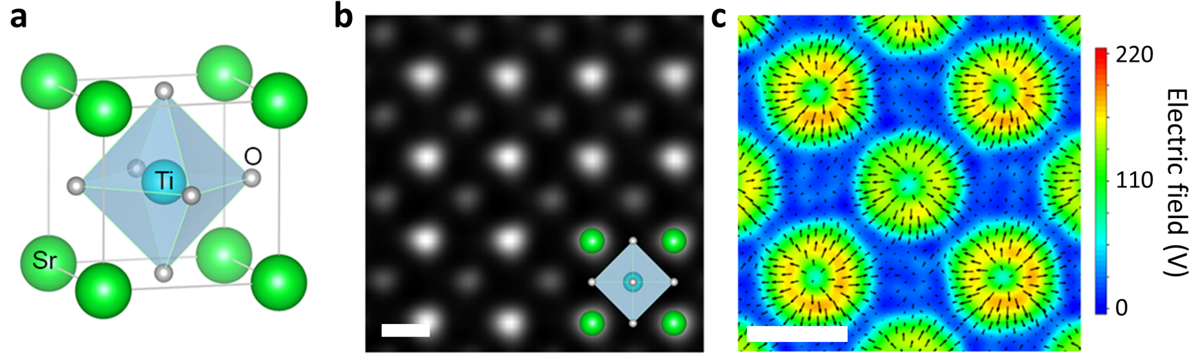

Figure 3.1: **Atomic structure and electric field of STO. a**, Atomic structure obtained from DFT calculation. **b**, HAADF STEM image of STO, scale bar: 2 Å, and **c**, the corresponding electric field map derived using the shift of center of mass from the scanning diffraction data set. The vectors represent the direction and magnitude of the local electric field in a unit cell of STO. Scale bar: 2 Å.

was corrected by rescaling the vertical axis to fit with the fast-scanned STEM image. These operations were first performed on the reconstructed HAADF and BF images based on the visible lattice and the same shift and rescaling operations were then applied to the electric field maps. Individual unit cells where then segmented and averaged together to generate a electric field final map of a single unit cell

The resulting electric field map after drift correction and averaging is shown in fig. 3.1c for a STO sample with a thickness of 5.6 ± 1 nm. The sample thickness was measured by least square fitting (LSF) of experimental position averaged convergent beam electron diffraction (PACBED)[140] data with the simulated data sets, details in Appendix B. The vectors show the direction and magnitude of local electric field. Note that the electric field is radially distributed around each Sr, Ti and O atom, suggesting its high symmetry around ions in STO. Furthermore, it is obvious that the electric field around the O columns is much weaker than that around the Sr and Ti-O columns.

In contrast to STO, BFO adopts a rhombohedral phase at room temperature[20], as shown in Fig. 3.2a. DFT calculations show that electric polarization in BFO originates from the deformation of Bi 6s lone pair electrons, which drives the rotation of Fe-O octahedra along

the (111) axis and displaces the Fe atoms away from the center of the surrounding oxygen octahedral cage[3]. The HAADF image along the BFO $(100)_{pc}$ orientation is given in Fig. 3.2b, in which Bi and Fe-O columns can be identified from the Z-contrast as indicated by the inset atomic model. In this region, Bi atoms are displaced by about 0.35 Å away from the geometric center of the four nearest Fe-O columns towards the top right. As shown in the polarization map (Fig. 3.2c), the arrows are the dipole moment which is related to the shift of Bi atoms[44, 141].

Fig. 3.2d shows the virtual BF STEM image (left panel, collection angle 0-32 mrad) and the electric field map (right panel), both derived from the scanning diffraction data in the same area as in fig. 3.2b. Polarized electric field can be seen around all atomic columns, and a net dipole moment pointing diagonally downward is clearly revealed. A zoom-in image, from the reconstructed HAADF, is shown in fig. 3.2e. The electric field from a single unit cell after drift correction and averaging is shown in fig. 3.2f, where the dipole induced polarized electric field is shown at a sampling rate of 0.2 Å/pixel. It is worth noting that the electric field surrounding the cation columns is no longer radially symmetric: the field is weak in the top right and stronger in the bottom left across the Bi site.

3.2.2 Charge density imaging and comparison with theory

Using the electric field maps in figs. 3.1c and 3.2f, we generated projected charge density images by computing the divergence. Fig. 3.3a and b display the 2D charge density images of STO and BFO in the (001) plane from scanning diffraction experiments. The charge density maps contain negative contributions from both core and valence electrons and positive contributions from atomic nuclei. Note that the nuclear charge distributions appear as broad Gaussians because of the shielding effect from core electrons and the size of the electron probe.

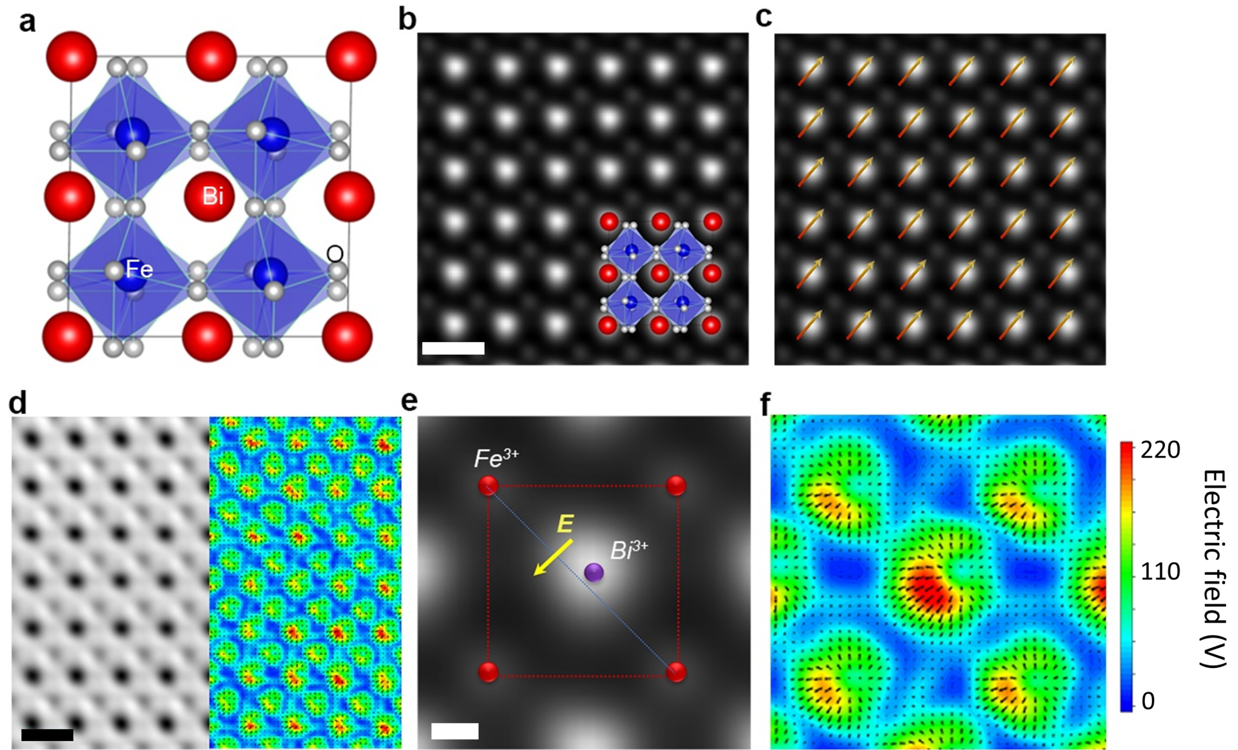

Figure 3.2: **Atomic structure and electric field dipole of BFO. a**, Atomic structure of BFO obtained from DFT calculations. Bi atoms are in red, Fe in blue, and O in grey. **b**, Atomic resolution HAADF STEM image of BFO, scale bar: 4 Å. The Bi atomic columns are seen shifted towards the top right of the unit cell defined from the four Fe columns in the corners. **c**, The dipole moment is defined to be polarized towards top right, as shown by the vectors. **d**, Conventional STEM images and electric field maps generated by scanning diffraction data: the bright field image (left) and the electric field map (right) of BFO, scale bar: 4 Å. **e**, The zoom-in reconstructed dark field STEM image of a BFO unit cell from the as-acquired scanning diffraction data set, where Bi is marked in purple, Fe in red, scale bar: 1 Å. **f**, The corresponding electric field map, the color represents the magnitude of the local electric field. The electric field vector around Bi is stronger pointing toward the bottom left corner. Around Fe columns, the electric field is also deformed diagonally towards the bottom left.

To validate our experimental images of the charge density, we used density functional theory to calculate the charge density of bulk STO and BFO. The first-principles density functional calculations were performed with the Vienna Ab-initio Simulation Package (VASP)[142, 143]. The spin-polarized generalized gradient approximation (GGA)[144] was used for the description of the exchange-correlation interaction among electrons. We treated Bi-6s6p, Fe-3d4s, Sr-4s4p5s, Ti-3d4s and O-2s2p as valence states and adopted the projector-augmented wave (PAW) pseudopotentials to represent the effect of their ionic cores[145, 146]. Spin-orbit coupling (SOC) was not included in the calculation. To describe the correlation effect properly, the GGA + U method was used for the localized d-orbitals of Fe (U = 3.0 eV, J = 0.0 eV)[147]. Calculations of 2x2x2 supercells were carried out to simulate (a) the rotation of adjacent oxygen octahedron and distorted Bi and Fe sites along [111] direction, (b) the G-type antiferromagnetic exchange coupling between Fe atoms. We sampled the Brillouin zone by adopting the Γ-centered Monkhorst-Pack method[148] with a density of about $2\pi \times 0.03$ Å^{-1} in all calculations[149]. Brillouin zone integrations are performed with a Gaussian broadening of 0.05 eV during all calculations. The energy cutoff for the plane-wave expansion was 500 eV which result in good convergence of the computed ground-state properties according to our previous investigation of oxides[150–152]. Structures were optimized with a criterion that the atomic force on each atom becomes weaker than 0.01 eV/Å and the energy convergence is better than 10^{-6} eV.

To corroborate the experimental observations and validate that the observed image contrast is from local charge density, the electron charge density of bulk STO and BFO projected along (001) direction are derived through DFT calculations. It is well known that DFT allows for solving the one-electron Kohn-Sham equations and only evaluating the electron density using a lattice potential acting on the system's electrons[153]. To appreciate the positive charge effect from nucleus in experiment, a Gaussian distribution of effective core charge at different nucleus sites are constructed with the conservation condition that positive charge is equal to negative charge (total number of electrons) in the system. The Gaussian

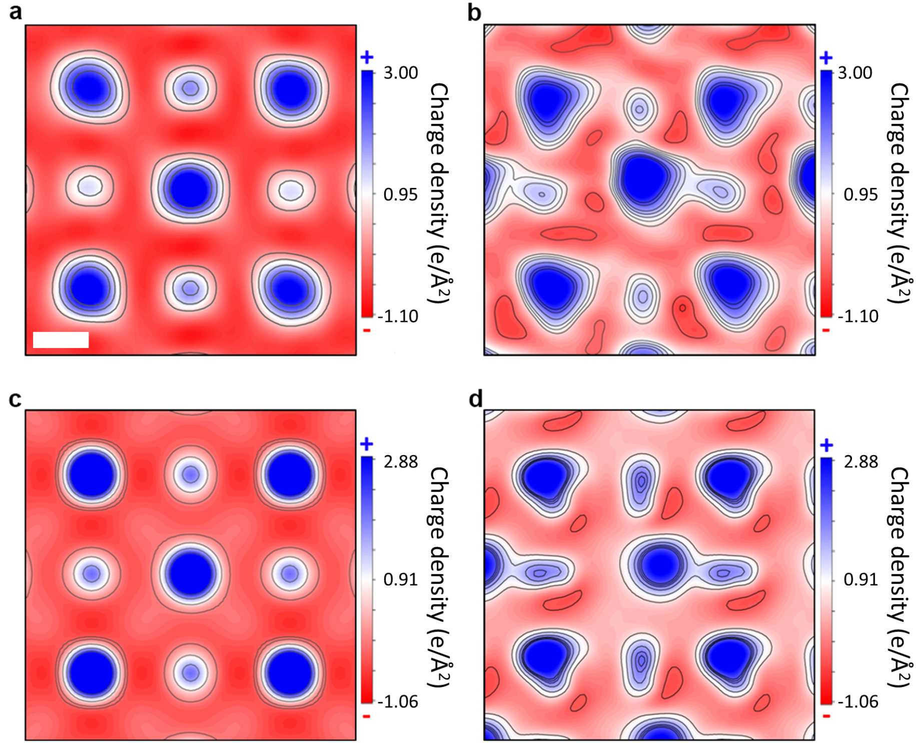

Figure 3.3: **Real space charge density mapping in STO and BFO. a**, Charge density map, ρ, of bulk STO from scanning diffraction experiments. **b**, Charge density map of bulk BFO. **c**, Charge density image of bulk STO obtained from DFT calculations. **d**, Charge density image of bulk BFO obtained from DFT calculation. The simulated positive charge distributions for nuclear and core electrons is constructed by three-dimensional Gaussian function. Scale bar is 1 Å.

broadening width for Sr, Ti, Bi, Fe and O are 0.40 Å, 0.31 Å, 0.50 Å, 0.33 Å and 0.30 Å, respectively[154]. The DFT calculated charge density image is then derived by summing up the electron charge density of the ground states and the Gaussian distributed positive charge density.The similarity in key features in Fig. 3.3 (a-b from experiment and c-d from theory) suggests that the RSCDI indeed reliably reveals the details of charge distribution between atoms in crystalline solids.

One immediate outcome from the charge density mapping is the clear appearance of the oxygen atomic columns in both materials. Locating oxygen atoms is already an important issue for studying the octahedral rotation, which is often involved in phase transition and changes of physical properties of complex oxides such as $La_{1-x}Sr_xMnO_3$[155] and Sr_2RuO_4.[156] For

STO (Figs. 3.3a,c), the oxygen columns are thin, indicating no rotation of oxygen octahedra away from the principle axis. In a sharp contrast, the oxygen columns for BFO are elliptical (Figs. 3b,d) due to the large rotation of oxygen octahedra (about 11° based on DFT calculations), resulting in the splitting of the oxygen columns in the 2D projection (Fig. 3.2a).

In the interstitial regions, the negative charge density of STO (Fig. 3.3a) displays a four-fold symmetry around the columns of Sr atoms, matching its crystallographic symmetry. While the ionic nature dominates the interatomic interaction, the existence of intense red regions suggests electron charge accumulation between oxygen atoms and cations, indicating small covalent characteristics of Sr-O and Ti-O bonds in STO. In contrast, the 2D charge density image of BFO shows the deformed shapes of positive charge on all atomic sites. As shown in Fig. 3.3b and d, the charge contours on Fe sites exhibit triangular geometry, which originates from the anisotropic Fe-O bonds with d-orbitals of Fe atoms. The positive charge density pocket of Bi shows a partial connection to the closest oxygen column and the existence of more intense red pockets between cations and O indicates stronger covalent nature of Bi-O and Fe-O bonds in BFO than those in STO. This is also supported by analysis of the crystal orbital Hamiltonian populations in Bi-based ferroelectric materials such as $BiMnO_3$ [3]. It is worth noting that regions of intense negative charge density migrate to the bottom left side of the nuclei, from which we can directly image the electric polarization in BFO along with the oxygen octahedron tilt.

As a further step, we calculated the positions of weighted centers of positive and negative charge in BFO which allows us to determine the effective charge separation in a unit cell, a key physical quantity of multiferroic materials. We found that the separation between the positive and negative charge centers is about 0.57 Å along the diagonal axis projected in the (100) plane; this process is illustrated in fig. 3.4. According to the definition of dipole moment $\mathbf{p} = q\mathbf{d}$, where q is the charge, $\mathbf{d}$ the displacement, the measured $\mathbf{p}$ is 3.12

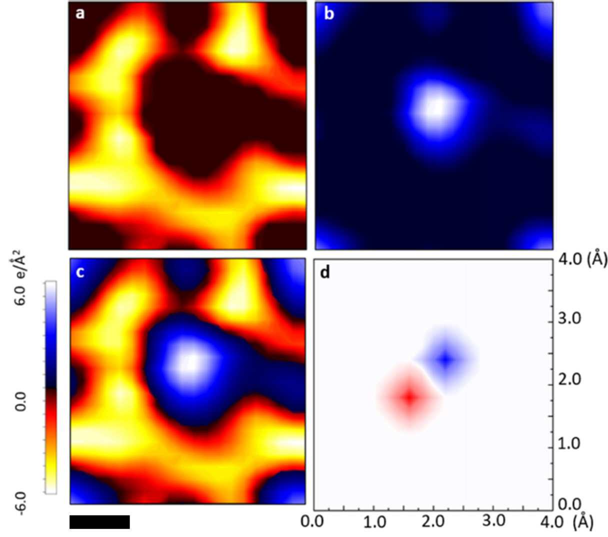

Figure 3.4: **Separation of positive and negative charge in a BFO unit cell. a–c**, Negative charge (**a**); positive charge (**b**); and overlapping of positive and negative charge (**c**) in the pseudo-cubic unit cell of BFO. **d**, Positions of positive (blue) and negative (red) charge center. Scale bar: 1 Å.

± 0.9 eÅ/unit cell, corresponding to a ferroelectric polarization of 78 ± 23 μC/cm^2 along the (111) direction, comparable to the reported value of 100 μC/cm^2[157]. Therefore, the high-resolution RSCDI not only enables us to directly see the charge polarization in BFO, but also to quantitatively determine its dipole moment.

3.3 $BiFeO_3$-$SrTiO_3$ interface

RSCDI's capability to quantify the physical characteristics at high spatial resolution makes it possible to study the complex interfaces in oxides[158, 159], where many intriguing phenomena have been reported, such as the existence of superconductivity[160, 161], polarization vortices[44], quantum Hall effect[162] and magnetism[20, 33, 160]. Applications based on these phenomena require better understanding of the interplay among lattices, electrons, orbitals and spin at the interface [158]. BFO is multiferroic and the effect of its strong electric polarization is predicted to cause band bending in adjacent STO which, in turn,

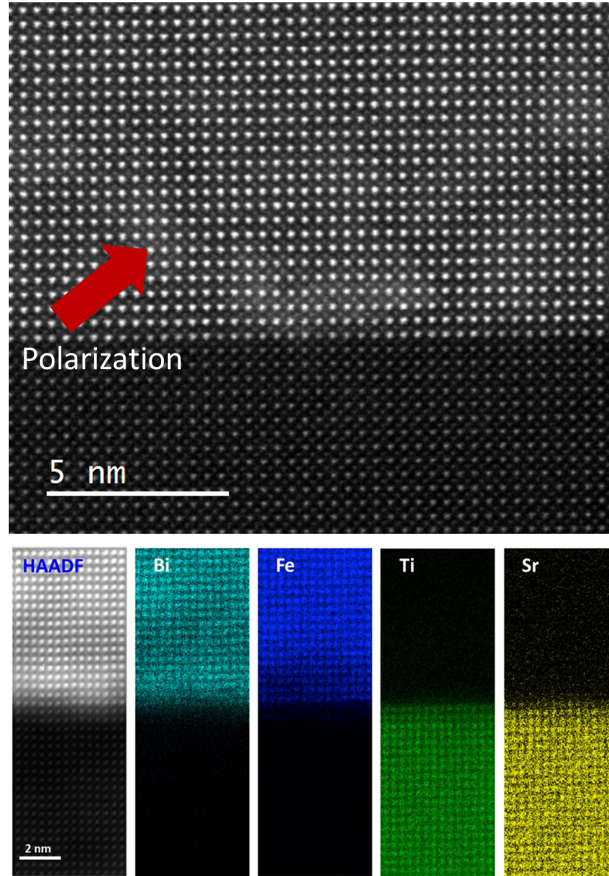

Figure 3.5: **Atomic-resolution HAADF image and EDS maps across the BFO-STO interface. Top,** HAADF-STEM image of the BFO-STO interface from the region where 4D STEM data was collected. **Bottom,** The EDS spectrum image was acquired using a JEM300CF AC-STEM system with EDS dual silicon-drift detectors (SDDs). Thirty scans (each with a 0.4-ms dwell time) in the same area across the interface were aligned and summed. The HAADF-STEM images and atomic-resolution EDS maps of Bi, Fe, Sr and Ti reveal an atomically sharp interface.

exhibits several emergent properties such as controllable interfacial conduction and photovoltaics[163]. However, due to the absence of detailed experimental information in the past regarding charge rearrangement in the interfacial region, the understanding of the interplay among the atomic structure, charge, orbital and spin almost solely relies on DFT calculations which are also limited by the size and complexity of the system.

We now turn to studying a BFO-STO heterostructure using the unique capabilities of RSCI to study the electronic properties across the interface. HAADF imaging and EDS mapping

from the interface, shown in fig. 3.5, confirm that it is atomically sharp, with no mixing of elements across the interface. 4D STEM data was collected from a small area within the region shown in 3.5. As indicated by the structure model obtained from DFT calculations (fig. 3.6a), the STO substrate connects to BFO by sharing a Bi-O layer at the interface. In fig. 3.6b, the reconstructed HAADF STEM image shows a sharp contrast between weak Sr intensity and strong Bi intensity. As shown in fig. 3.6c, d, we mapped the electric field and the charge density in the same area as in fig. 3.6b. The electric dipoles are visible in BFO, particularly near the Bi columns. On approaching the interface, the electric dipoles become weaker in the bottom BFO layers and some induced dipoles appear around the Sr columns of top STO layers in the substrate; similar phenomenon of the electric field penetrating the insulator has been proposed at $PbZr_{0.2}Ti_{0.8}O_3/SrTiO_3$ interfaces[33]. Some qualitative observations can also be made from the charge density image alone. As shown in fig. 3.6d, the oxygen columns are well resolved in STO but become vague and elongated in BFO owing to the rotation of Fe-O octahedra. However, the oxygen atoms at the interface appear to have less positivity than in STO and less elongation than in BFO, indicating the oxygen octahedra are in an intermediate state. In addition, in BFO, the separation between the positive and negative charge pockets is clear but weakens gradually when approaching the interface. Surprisingly, the charge separation persists in STO with a smaller amplitude than in BFO.

Figs. 3.6e-h summarize quantitative analysis of the atomic structure, charge density image, and supporting EELS spectrum imaging. Each will be addressed in detail below.

3.3.1 Atomic structure analysis

Fig. 3.6e shows the A-site displacement and rotation of the oxygen octahedron across the BFO-STO interface measured from both experiment and DFT calculations. In experimental

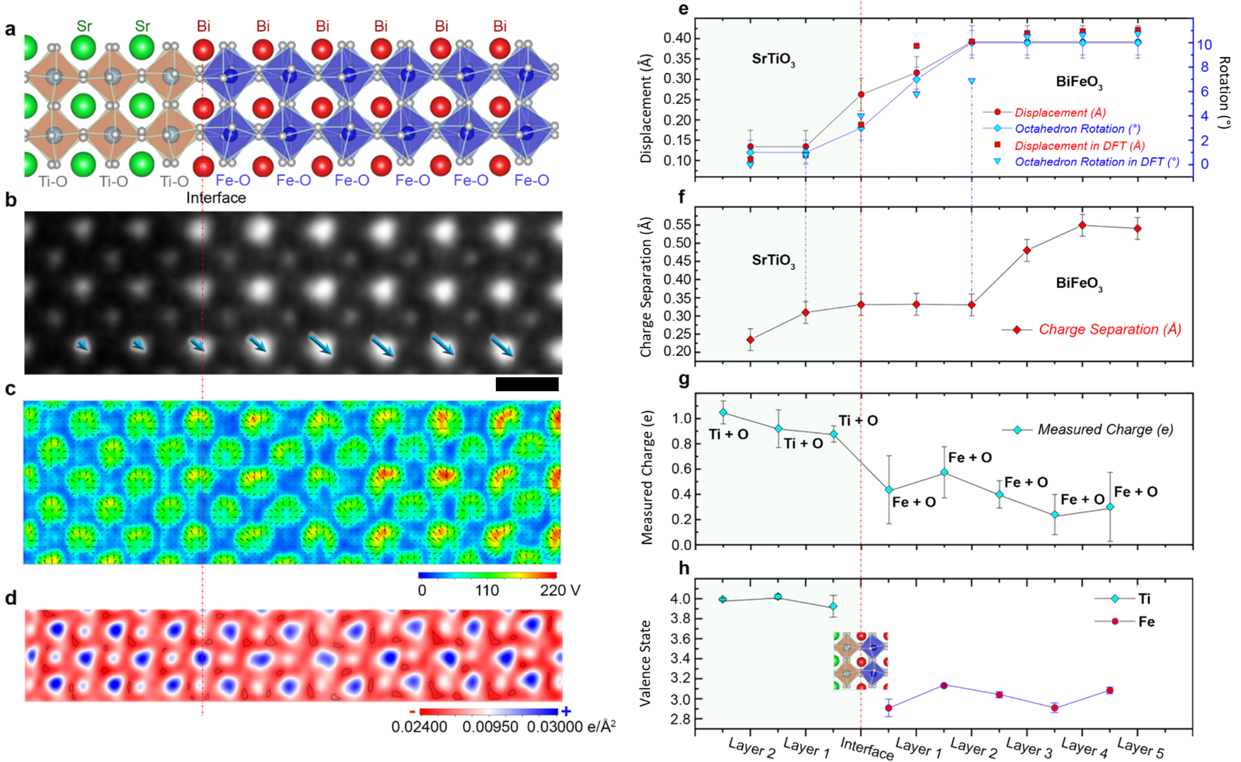

Figure 3.6: **Charge-density map, O octahedron rotation and valence charge state at the interface between BFO and STO. a,** Atomic structure of BFO-STO obtained from DFT calculations. **b**, Atomic-resolution HAADF-STEM image of BFO-STO. Scale bar: 4 Å. Arrows show the direction and relative magnitude of Bi displacement. **c**, Corresponding electric-field map derived from the scanning diffraction dataset. **d**, Charge-density map for BFO-STO. **e**, Changes in A-site displacement across the interface (that is, changes in the displacement of the Bi or Sr atom from the geometric centre of the four nearest Fe or Ti atoms), determined experimentally and by DFT calculation (in Å; error bars denote standard deviation). Also shown is the O octahedron rotation determined experimentally (in degrees; error bars denote the detection limit) and from DFT calculations (scattered points). **f**, Charge separation between weighted centers of positive and negative charge within unit cells across the interface. Error bars denote the detection limit. **g**, Total charge of Ti + O and Fe + O on the two sides of the interface, measured using RSCDI. Error bars denote standard deviation. **h**, Valence states of Ti and Fe measured using high-energy resolution EELS. Error bars denote standard deviation.

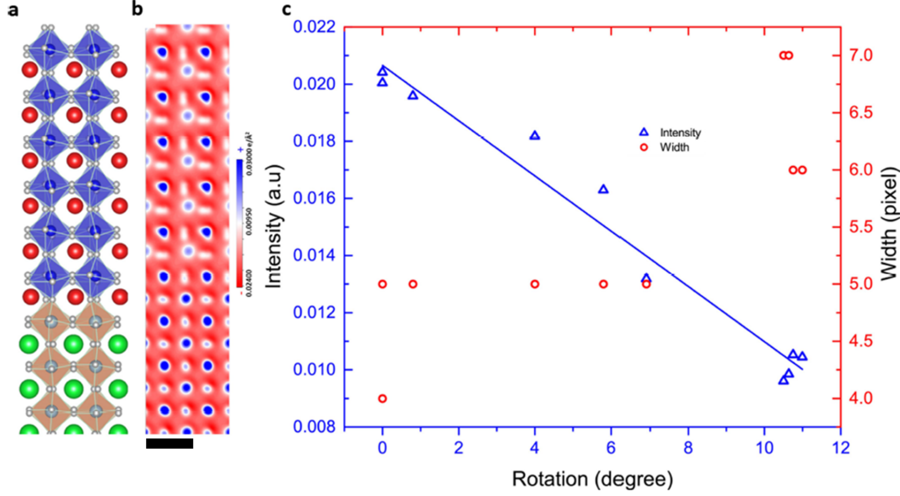

Figure 3.7: **Measurement of O octahedron rotation.** **a**, Atomic model of the BFO-STO interface, which is relaxed and then calculated by DFT. The rotation of O octahedra is readily visible from the splitting of the O atoms in this projection. **b**, Charge-density image calculated using DFT. The images of O charge become elongated and weak with higher O octahedron rotation. **c**, Intensity of O column charge (blue) and width of O intensity (red) plotted against O octahedron rotation measured using the atomic model from DFT calculations. Scale bar: 4 Å.

data, A-site displacement is measured using the reconstructed HAADF image; the displacement is defined as the difference between the center of the four adjacent B-site atoms and the A-site position. This is a common method for measuring ferroelectric polarization [44]. In experiment, the octahedral rotation is measured using the charge density image with the help of results from DFT. In RSCDI images, oxygen can be seen from the positive charge intensity. Without oxygen octahedra rotation, in STO, the oxygen atoms in the face centers overlap along the projection of (100); with rotation, in BFO, the oxygen atoms in face centers split along the projection. Such splitting leads to the weakening and elongation of the oxygen charge intensity.

In the charge density image from DFT, we plot the intensity and width from oxygen columns along with the rotation angle in fig. 3.7. In general, with higher octahedra rotation, the oxygen intensity elongates and the peak intensity decreases. From 1 to 7 degree of rotation, no obvious change in the width of the oxygen intensity is seen. However, the peak intensity

is more sensitive to octahedra rotation in this range, as shown by the blue points and linear fit in the plot. The linear fitting between oxygen intensity and octahedra rotation is then used for quantifying the oxygen rotation in experiment. The error bar used is 1°, because the fitting shows the deviations of all points are below 1°from the linear curve. Based on this model, we can see that both atomic displacement and octahedra rotation change rapidly across the interface, with the Bi displacement of 0.35 Å in BFO changing to the Sr displacement of 0.13 Å in STO, and the octahedral rotation falling sharply from 10° to less than 1° across the interface.

3.3.2 Charge Separation

Fig. 3.6f shows the charge separation of each unit cell across the interface. Each unit cell in fig. 3.6d is segmented based on the positions of the four B-site atoms surrounding each A-site atom. The charge separation of each unit cell is then quantified in the same manner illustrated in fig. 3.4. In comparison to the changes in the atomic structure, the charge separation is more adaptive, dropping early in the second layer of BFO from 0.54 Å to 0.33 Å and remaining the same across the interface until after the first layer of STO, where it further drops to a lower value of 0.23 Å. The atomic structure combined with electron charge relocation shows that the electrons are more responsive to the electric field of the polarized BFO, while the atomic displacement is more rigidly affected by the atomic strain. This unsynchronized response takes places in the interfacial region of 3 unit cells (between the two blue dashed lines in Fig. 3.6e and f) and leads to the phenomenon of interface charging which is the key for understanding and engineering the 2D electron or hole gas localized at the interface.

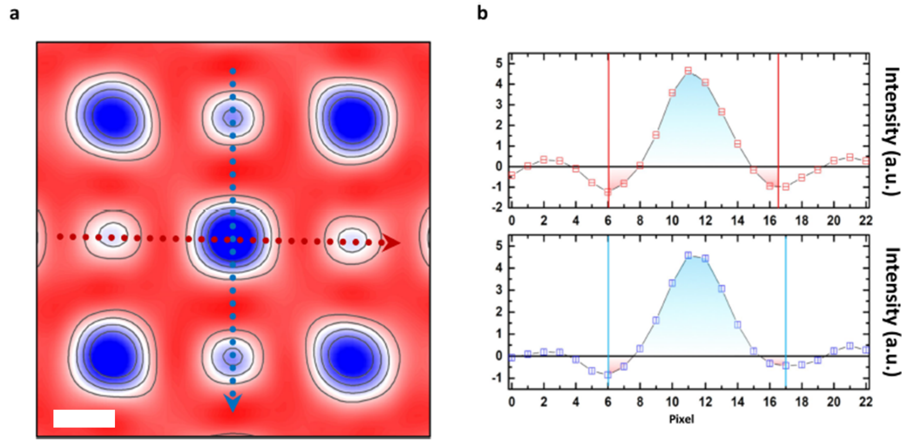

Figure 3.8: **Determination of the region for measuring the total charge of atomic columns.** **a**, 2D charge-density image of STO. **b**, Charge intensity profile drawn along the horizontal (red) and vertical (blue) directions as shown in a. Local minima in the charge-intensity profile are defined as the boundary of the area included for integrating the charge. Scale bar: 1 Å.

3.3.3 Charge state measured with Bader charge analysis

Fig. 3.6g shows the integrated charge of B-site columns across the interface. The total charge from individual atomic columns is measured by integrating the intensity within a region around each atomic column in the charge density image. To define the center of all heavy atomic columns, we used the peak position of atoms in the HAADF image calculated by 2D Gaussian fitting. To determine the size of the integration area, we adapted a method from DFT on calculating the charge state of atoms, Bader charge analysis [164, 165], which uses the saddle points of the 3D charge density contour between atoms to define the boundary for electrons belonging to different atoms. Projecting from 3D to 2D, the saddle point of the charge density in 3D corresponds to the minimum charge density surrounding atomic column in 2D. Therefore, as shown in fig. 3.8, to define the integration boundary, we search for the local minimum in the charge density on each side of the atomic column and then define the integration boundary as a circle centered on the atomic column with radius equal to the average distance to the minima on each side. The total charge state of each column is then defined as the integrated charge within this boundary.

In the measurement of total charge for each atomic column, note that in STO, along the (100) projection, Ti and O atoms overlap, so the integrated charge in STO is from Sr, O, and Ti+O columns. In BFO, it is similar that Fe and O overlap, so the measured charge is from Bi and Fe+O columns. The O columns in BFO are not considered due to the splitting of the oxygen columns. For each type of atomic column across the interface in experimental data, the intensity is measured and shown in the histograms in fig. 3.9. From the fitting the peaks, Bi intensity centers on 9.58, Sr centers on 5.71, Ti+O centers on 4.45, Fe+O centers on 2.51 and O centers on -1.50. As the measured intensity resembles the total charge, including positive nuclei and core orbital electrons, the charge intensity reflects the valence of each types of atomic column.

To provide the estimate partial charge of the atoms and calibrate our experimental measurements, we performed Bader charge calculation for bulk STO and BFO using the charge density from DFT[164, 165]. As shown in Fig. 3.10a, for bulk STO from DFT, we found the partial charges are 8.421e, 1.445e and 7.378e for Sr, Ti and O atoms, respectively. Since there are 10, 4 and 6 valence electrons for Sr ($4s^2 4p^6 5s^2$), Ti ($3d^2 4s^2$) and O ($2s^2 2p^4$) atoms, their corresponding valence states are $Sr^{+1.58}$, $Ti^{+2.55}$ and $O^{-1.38}$, respectively. Similarly, in bulk BFO from DFT, we found 2.131e, 6.119e and 7.584e for Bi, Fe and O atoms, respectively. Considering there are 5, 8 and 6 valence electrons for Bi ($6s^2 6p^3$), Fe ($3d^6 4s^2$) and O ($2s^2 2p^4$) atoms, their corresponding valence states are $Bi^{+2.87}$, $Fe^{+1.88}$ and $O^{-1.58}$, respectively.

It should be noted that the Bader charge calculation uses saddle points (or the so-called "zero flux surfaces") on which the charge density is a minimum to separate atoms from each other[164, 165]. Due to the covalent bond nature in STO and BFO system, the charge states obtained through Bader charge analysis are usually underestimated and is not fully consistent with the definition of "valence" in chemistry, especially when comparing to the valence states measured through electron energy loss spectroscopy (EELS).

In stoichiometric phase BFO, the valence state of Bi, Fe, and O are 3+, 3+, and 2-, respec-

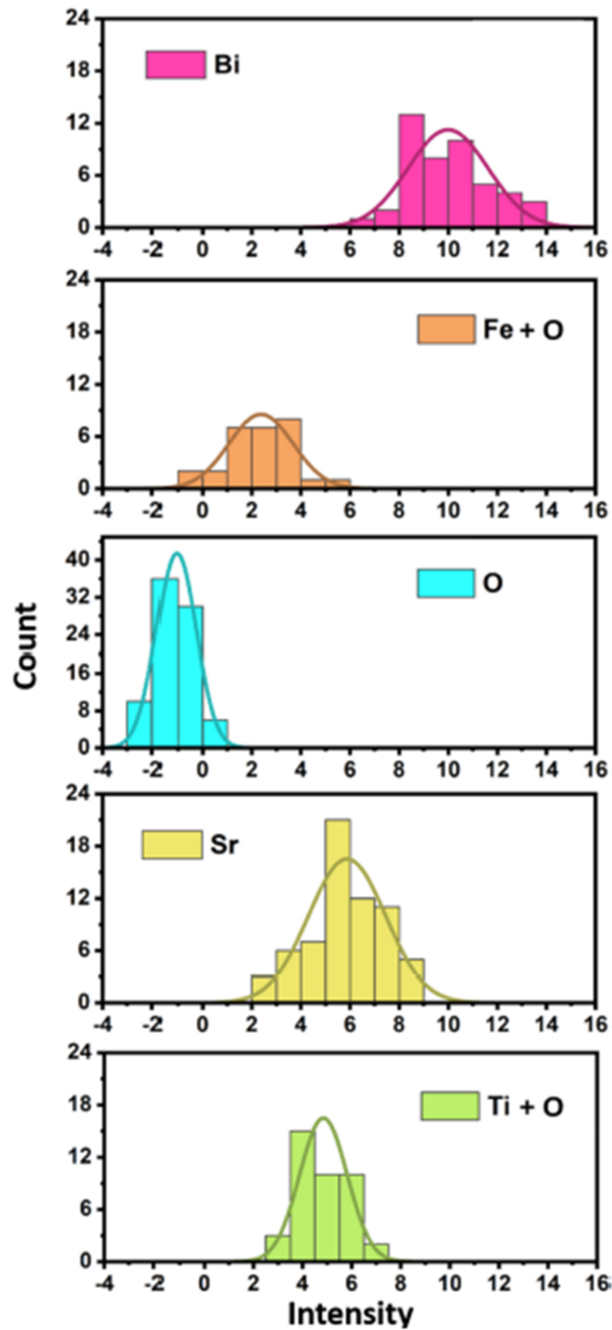

Figure 3.9: **Measurement of the total charge of each atomic site.** Histograms showing the integrated intensity of Bi columns, Fe + O columns, O columns, Sr columns and Ti + O columns from charge-density images of BFO and STO.

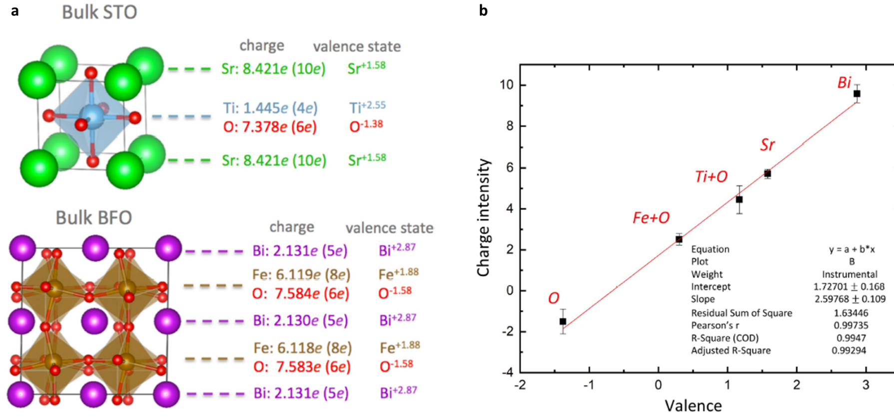

Figure 3.10: **Charge-intensity change as a function of valence.** **a**, Partial charge and valence states of all atoms derived through Bader charge analysis in DFT. **b**, Integrated intensity in each atomic column in the charge-density image, plotted as a function of valence derived through DFT to show their correlation. The red line is the linear fit.

tively, which makes the Fe+O column 1+ when projected along (100). In STO, the valence states of Sr, Ti and O, are 2+, 4+, and 2-, respectively, making the projected Ti+O column 2+. If we order each atomic column according to its valence state (Bi 3+, Sr 2+, Ti+O (2+), Fe+O (1+), and O 2-), we can see that it matches the ordering of the integrated intensities given by the charge density image (fig. 3.9). However, as discussed above, the partial charge derived from charge density, both in experiment and DFT, could be different from the definition of "valence" in chemistry. Therefore, the total charge intensity is compared with the partial charge derived in DFT. This is shown by the plot in fig. 3.10b. All charges are well fitted with a linear curve between the charge intensity and the partial charge from DFT. We then used this linear relationship to estimate the charge of Ti+O and Fe+O columns across the interface in fig. 3.6g, where the error bar denotes the standard deviation from all atomic columns in a row parallel to the interface. Based on this quantification method, we can see that the integrated charge of both the Ti+O an Fe+O columns dip at the interface, indicating an electron rich interface.

By comparing the experimentally measured partial charge with those from DFT calculation, we show quantification of partial charge using RSCDI can be reliable. Relative changes in

atomic charge can be easily observed by comparing the partial charge of atomic columns, when the area is uniform in thickness. Fully quantitative measurement depends on the calibrating the intensity values from the charge density image, which can be achieved by two ways: (1) precisely measuring the sample thickness, calibrating the instrument, and using a standard sample as a reference; (2) comparison with DFT calculation.

It is also worth noting that for measuring the total charge, RSCDI will work best in the case the sample is along a zone axis where each atomic column only comprises of one atom species, so atoms with different charge states will not overlap. The projection of three-dimensional charge to two-dimension can also underestimate those bond charge that are distributed among atoms at different heights. This effect is studied in greater detail in Ch. 5.

3.3.4 EELS analysis

Fig. 3.6h shows the valence state of Ti [81] and Fe [75, 166] atoms as measured from analysis of EELS near edge fine structure. High spatial resolution STEM-EELS experiments were carried out on a Nion UltraSTEM 200, equipped with C_3/C_5 corrector and high-energy resolution monochromated EELS system (HERMES). The instrument was operated at 60kV with convergence semi-angle of 30mrad and with a beam current of 100pA. For spectrum image acquisition, a dispersion of 0.19 eV/channel was used, the dwell time was set as 0.4 s/pixel, and pixel size was 0.1 nm/pixel. The background in each spectrum was removed by fitting a power-law function to the pre-edge region using the commercial software package DigitalMicrograph. To reveal the valence state of Ti, we used the multiple least square (MLS) methods to separate the Ti^{4+} and Ti^{3+} components on each Ti EEL spectrum by the following equation, $S(E) = a_1R_1(E) + a_2R_2(E) + \chi(E)$, where E is energy loss, $S(E)$ is the experimental EEL spectrum, $R_1(E)$ and $R_2(E)$ are standard Ti^{4+} and Ti^{3+} spectra

taken from literature[81], a_1 and a_2 are fit coefficients (spectral weight) of Ti^{4+} and Ti^{3+} components, and χ(E) is the residual spectra. The fitting process was performed in the commercial software Digital Micrograph. The valence state of Ti was further calculated by weighted arithmetic mean of Ti^{4+} and Ti^{3+} components and shown in Fig. 4h. For analyzing valence state of Fe, we measured the difference between onset energy of O K-edge and Fe L_3-edge, which were determined by the energy loss where the edge reaches 10% of its maximum intensity. Due to the linear relationship between the Fe-O onset energy difference and the valence state of Fe,[75, 166] we can further calculate the localized valence state of Fe as shown in Fig. 3.6h, the error bar denotes the standard deviation from all points collected within the atomic columns.

Based on this analysis of the fine structure, the Ti valence decreases from 4+ to 3.7+ approaching the interface from the STO side, indicating a mixture of Ti^{4+} and Ti^{3+}.

There is slight discrepancy between the charge states measured by EELS and charge density imaging, where the charge drops earlier in STO in Fig. 3.6g and later in Fig. 3.6h. This comes from the delocalization of EEL spectrum, where the signal can be influenced by adjacent regions. As measured in EELS, the slightly higher valence of Ti close to the interface is the result of the valence of Ti from the bulk part of the STO being delocalized and detected by the probe at the interface. However, charge density imaging is a more local probe, as the probe is only affected by the field within its interaction volume and we only integrate the charge density close to the atomic column. Therefore, the local charge measured by charge density imaging more clearly shows change in the charge state of individual atomic columns rather than the material as a whole, which is measured with EELS.

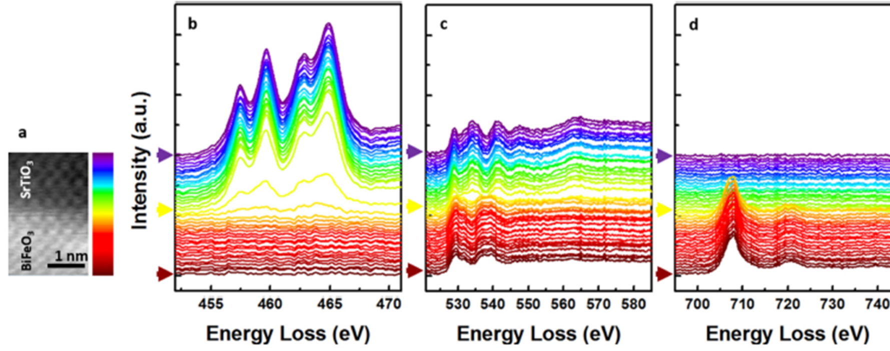

Figure 3.11: **High-resolution core-loss EELS measurement of Ti, O and Fe at the BFO-STO interface.** **a**, HAADF-STEM image used for acquiring EELS data on the BFO-STO interface. Scale bar, 1 nm. **b–d**, Stacking EEL spectra of the Ti $L_{2,3}$-edge (**b**); O K-edge (**c**); and Fe $L_{2,3}$-edge (**d**) across the interface. The location of each coloured spectrum is marked by the colour bar in a. Each spectrum is averaged in the direction parallel with the BFO-STO interface. The purple, yellow and maroon arrows indicate respectively the top edge, interface and bottom edge of the mapping region in **a**.

3.4 Conclusion

In summary, we developed a new method to map the local charge density of materials in real space with sub-Å resolution STEM. The validity of this technique is established through the side-by-side comparison with DFT calculations for STO, BFO and their interface. For the first time, we showed the atomic scale charge density at the interface of STO and BFO, and illustrated the variation of electric dipoles and valence state in the interfacial region. The ability to experimentally trace electron redistribution and probe local bonding in heterogeneous materials at the subatomic level will have a significant impact on the characterization and design of functional materials.

Chapter 4

Electric field imaging in $PbTiO_3$-$SrTiO_3$ superlattice

4.1 Introduction

The electrical properties of nanostructured ferroelectric materials make them among the top candidates for applications towards next generation electronic devices [11, 12, 22, 108, 109]. In ferroelectrics, the polarization can interact with the boundary conditions of thin films heterostructures resulting in various configurations that modify the electric field and charge distribution. Certain polarization patterns can lead to charge accumulation at domain walls [17, 18, 31] and interfaces [32, 33, 139, 167] which could be used for low-power electronic devices. Recently, in ferroelectric multilayers, polarization-vortex structures have been demonstrated to host charge accumulation at their cores [50] and regions of stable negative capacitance [124]. Many exotic states in ferroelectrics are found and studied with the assistance of advanced structural characterization using transmission electron microscopy (TEM). Especially with the latest development of DPC, 4D STEM, and holography in TEM,

the electric field and charge in a sample can be resolved at the atomic scale [98, 99, 110, 113, 119].

4D STEM is a versatile technique due to the flexibility of experimental set-up [100]. But its complexity also challenges our current understanding and interpretation of the data, as each measurement can be strongly affected by the experimental conditions. In 4D STEM, electrical properties are interrogated through changes in the momentum distribution of a converged electron probe as it passes through the sample [99]. Therefore, the condition of the electron probe is a fundamental part of how it interacts with the sample [119]. For electric-field measurements in 4D STEM, there are generally two classes of electron probes used that can be defined by their probe size or, equivalently, convergence angle: picometer sized probes (semi-convergence angle $>$ 20 mrad, probe size $<$ 0.8 Å) and nanometer size probes (semi-convergence angle $<$ 2.5 mrad, probe size $>$ 0.5 nm). With a picometer-size probe, the electric field and charge density surrounding individual atomic columns can be imaged with DPC [98, 111, 113]. Similarly, 4D STEM/DPC has been used to study the electric field and charge densities in 2D materials [115, 120, 121], GaN/AlN nanowires [123], electride materials [138], and ferroelectric heterostructures [139, 168]. While nanoscale probes have much lower spatial resolution, they also offer larger field of view and greater flexibility in what can be extracted from the 4D STEM data. When the diffraction disks are well separated, the internal electric field can be measured from the center disk while the polarization or strain can be determined from the diffracted disks in the same dataset [105, 122, 124, 169], enabling other electronic properties to be determined, such as the permittivity [124, 125].

While 4D STEM/DPC electric-field measurements in ferroelectrics have uncovered several novel phenomena [124, 139, 168], the split in the approaches to measuring the electric field has also generated a range of different results that, when considered together, do not always present a consistent picture. Our investigations of BFO described in Ch. 3 and previous

publications with a highly convergent probe have indicated that the electric field is biased along the local polarization direction [139, 168], but measurements from the $PbTiO_3$ (PTO) layer in $(PTO)_{12}/(STO)_{12}$ superlattices using a low convergence probe do not exhibit a similar pattern [124]. How the polarization and built-in electric field in ferroelectric materials interact with the electron probe across all probe sizes and the mechanism for the interaction are still unclear. This chapter will describe measurements of the electric field using both classes of probes in the same material to understand why differing electric-field patterns have been observed and propose a model to explain them. We have chosen polarization vortex structures in $(PTO)_{16}/(STO)_{16}$ superlattices grown on $DyScO_3$ (DSO) (110) substrates as a model system, as shown in fig. 4.1a. The continuously rotating polarization in the PTO layer presents an optimal environment to study this problem because the changes in polarization direction are not associated with a ferroelastic distortion which may complicate analysis of the 4D STEM data. In a map of the electric field using a picometer-sized probe, we find that it exhibits the same vortex structure as the atomic polarization. In a map measured with a nanometer-sized probe, however, we do not observe the same vortex pattern. Combining this information with phase-field simulations, we show the coexistence of these two patterns can be attributed to two different mechanisms for generating the electric field.

4.2 Film growth and sample preparation

$[(PTO)_{16}/(STO)_{16}]_8$ superlattices were synthesized on single-crystalline DSO (011) substrates with a 4 layer STO buffer layer via reflection high-energy electron diffraction (RHEED)-assisted pulsed-laser deposition (KrF laser). The PTO and the STO layers were grown at 610 °C in 100 mTorr oxygen pressure. For all materials, the laser fluence was 1.0 J/cm^2 with a repetition rate of 10 Hz. RHEED was used during the deposition to ensure the maintenance of a layer-by-layer growth mode for both the PTO and STO. After deposition, the

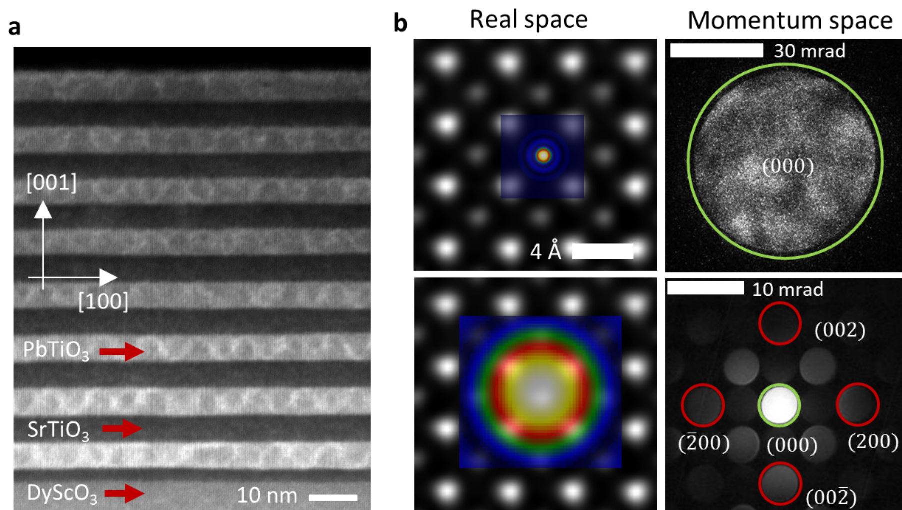

Figure 4.1: **Superlattice and probe conditions.** **a**, An ADF image of PTO/STO superlattice. The vortex structures are visible as the contrast variations in the PTO layers. **b**, Left column: the simulated 2D electron probe shapes for a 33 mrad (top) and 2.4 mrad (bottom) convergence angle electron probe overlaid on a HAADF image of STO. Right Column: Experimental CBED patterns for the corresponding convergence angles from PTO. The center disks CBED (green) are used to determine the electric field. The diffracted disks (red) in the 2.4 mrad CBED pattern are used to calculate the polarization.

heterostructures were annealed for 10 minutes in 50 Torr oxygen pressure to promote full oxidation and then cooled down to room temperature at that oxygen pressure.

TEM specimens were prepared by mechanical polishing using an Allied High Tech Multiprep. Cross-section specimens were cut along DSO (110) and polished into a wedge shape. Further thinning until the samples were electron transparent was completed in a Gatan PIPS 2, starting at 5 keV and then stepping down to a final cleaning stage at 200 eV. Sample thickness was measured to be 12nm based on fitting between experimental and simulated PACBED patterns, see Appendix B for details [106]. Although this is outside the range for fully quantitative electric field imaging, as shown in Chapter 2 and Ref. [170, 171], the electric field measured with 4D STEM maintains qualitative accuracy for samples up to 15-20 nm in thickness. Within this range, the electric field surrounding each atom maintains the expected direction (radially outward) and relative magnitude based on distance from the atomic column.

4.3 Atomic scale E-field

To image the electric field in high resolution, we used a 33 mrad convergence angle which results in an electron probe with full-width half-maximum (FWHM) of 0.6 Å; this is small compared to the (100) lattice spacing of STO and PTO, both close to 4 Å, as illustrated in fig. 4.1b [22]. The 4D STEM data was collected with a 0.3 Å step size on a K2 IS camera at 1200 fps, covering 3 vortices; a survey image with a conventional polarization map based on titanium/oxygen column displacement from the region is shown in fig. 4.2a. The projected electric field magnitude is shown in fig. 4.2b. Due to the relatively slow scan speed and large number of scanning points, drift correction is applied to the atomic resolution 4D STEM data after it has been analyzed by applying shear transformation to correct for lateral motion of the sample during acquisition. In non-polar materials, the electric field surrounding each atomic column points radially outward and is mostly rotationally symmetric, as can be observed in the STO layers near the top and bottom of fig. 4.2b. However, the electric field of cation columns in PTO show a strong asymmetry depending on the polarization direction. Fig. 4.2c-e shows a detailed view of the electric field in regions with polarization down and up in PTO and a region with no polarization in STO, respectively. The electric-field bias in fig. 4.2c and 4.2d points opposite to the local polarization measured by the atomic displacement in fig. 4.2a. Line profiles from regions marked in fig. 4.2d of the electric field magnitude illustrate this asymmetry, as shown in fig. 4.2f for both lead (red) and titanium/oxygen (black) columns. The projected electric field on the bottom side of both lead and titanium/oxygen columns peaks at over 1 kV. On the top side of the column, the electric field of the lead column peaks at 488.3 V while that of the titanium/oxygen column peaks at 861.3 V. These line profiles are indicative of a general trend where lead columns exhibit a strongly asymmetric electric field while titanium/oxygen columns exhibit weaker asymmetry. Some titanium/oxygen columns even appear almost perfectly symmetric as shown in fig. 4.3.

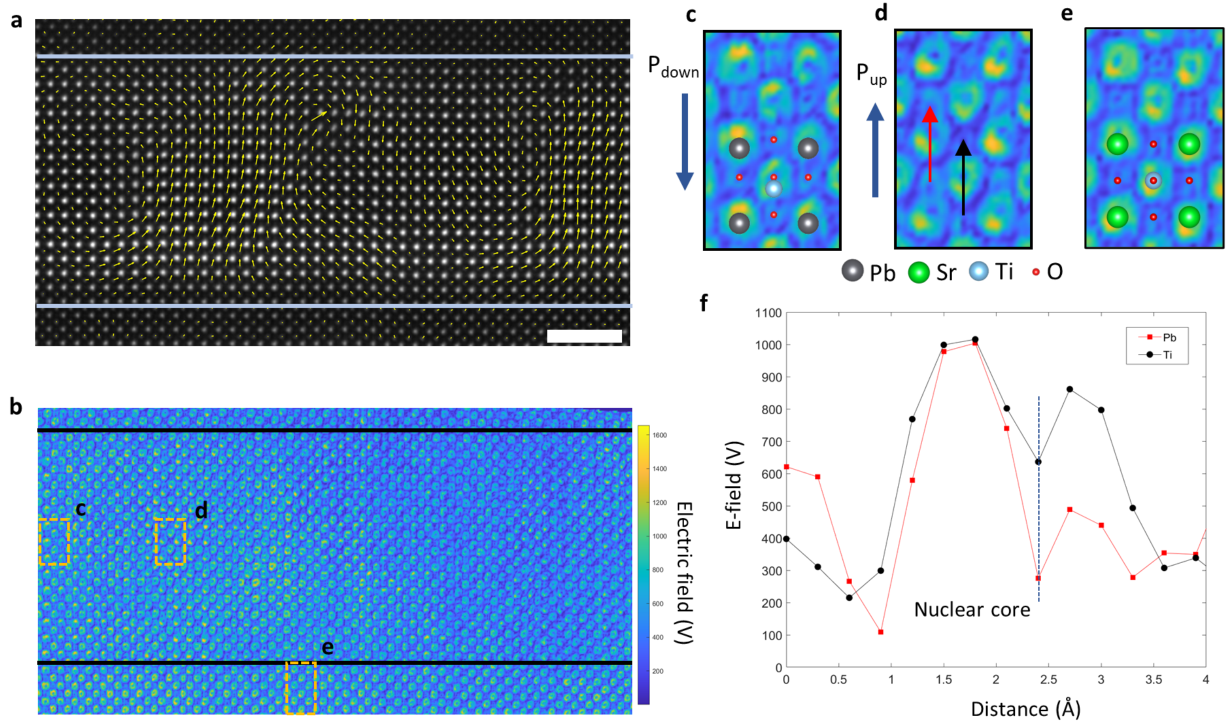

Figure 4.2: **Atomic scale electric field.** **a**, A HAADF survey image collected simultaneously with 4D STEM data. Atomic displacements are overlaid in yellow. Scale bar is 2 nm. **b**, Electric field mapping of the same region in **a**. **c**, Zoomed in view of a region with polarization down. **d**, A zoomed in view of a with polarization up. Red and black arrows indicate the position of the line profiles across lead and titanium/oxygen columns, respectively, shown in **f**. **e**, A zoomed in view of highlighted region in STO. **f**, Line profiles of the electric field magnitude across lead and titanium/oxygen columns.

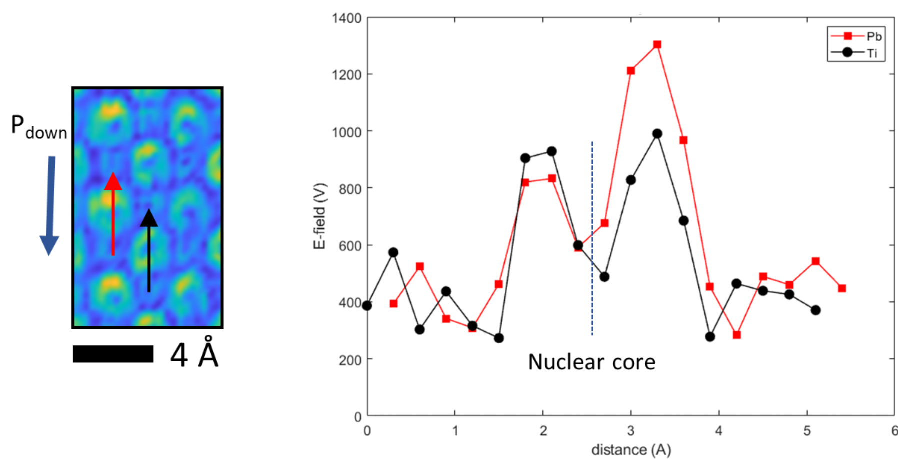

Figure 4.3: **Polarization down E-field.** Line profiles of the electric field magnitude from a unit cell in a region that is polarization up. The Pb column (red) shows a strong bias in the electric field, while the field of the Ti/O column is mostly symmetric.

To further analyze the electric-field distribution surrounding each atomic column, we first estimated the positions of all A-site (lead or strontium) columns using a simultaneously collected HAADF image with 2D gaussian fitting and then refined the position using the divergence of the electric-field image, also called the differentiated center of mass image (dCOM). With the positions measured accurately in the 4D STEM dataset, we then segmented a region of radius 0.9 Å surrounding each column and calculated the average electric-field within this region. With this method, atomic columns with a strong asymmetry will have a large average electric field, while columns with a more symmetric field distribution will have a small average field. This is applied to the full dataset in fig. 4.4a, where vectors of the average electric field of the A-site columns are overlaid on the full electric field map. Detailed views for the same regions highlighted in figs. 4.2c-e are shown in figs. 4.4b-d. Fig. 4.4e shows the average electric field overlaid on a HAADF image for clarity. Examining the entire region, we found the average electric field of each A-site column follows a vortex pattern that is coincident with that shown in conventional polarization map, fig. 4.2b. Notably, this vortex pattern is unique to the lead sites in the PTO lattice. While some titanium/oxygen columns do show an electric field bias, the entire region does not show significant ordering in the electric field (see fig. 4.5). Averaging the electric field over each unit cell also does not reveal the same vortex pattern (see fig. 4.6).

The dominant nature of the A-site electric field and correlation with the structural polarization in PTO agrees with previous studies of the atomic-scale electric field in BFO [139, 168]. Interestingly, in both materials, first principles calculations have shown that the 6s electrons of both lead and bismuth form covalent bonds when they hybridize with oxygen 2p electrons [1, 2, 4]. The 6s lone pair forms a localized lobe that pushes A-site cations away from the center of the unit cell, causing cooperative displacement of B-site cations and the oxygen octahedron. The combined off-center position of the 6s lone pair and the associated lattice distortion results in the polarization of the unit cell. This indicates that the electric field bias surrounding lead atomic columns observed here and on the bismuth columns in

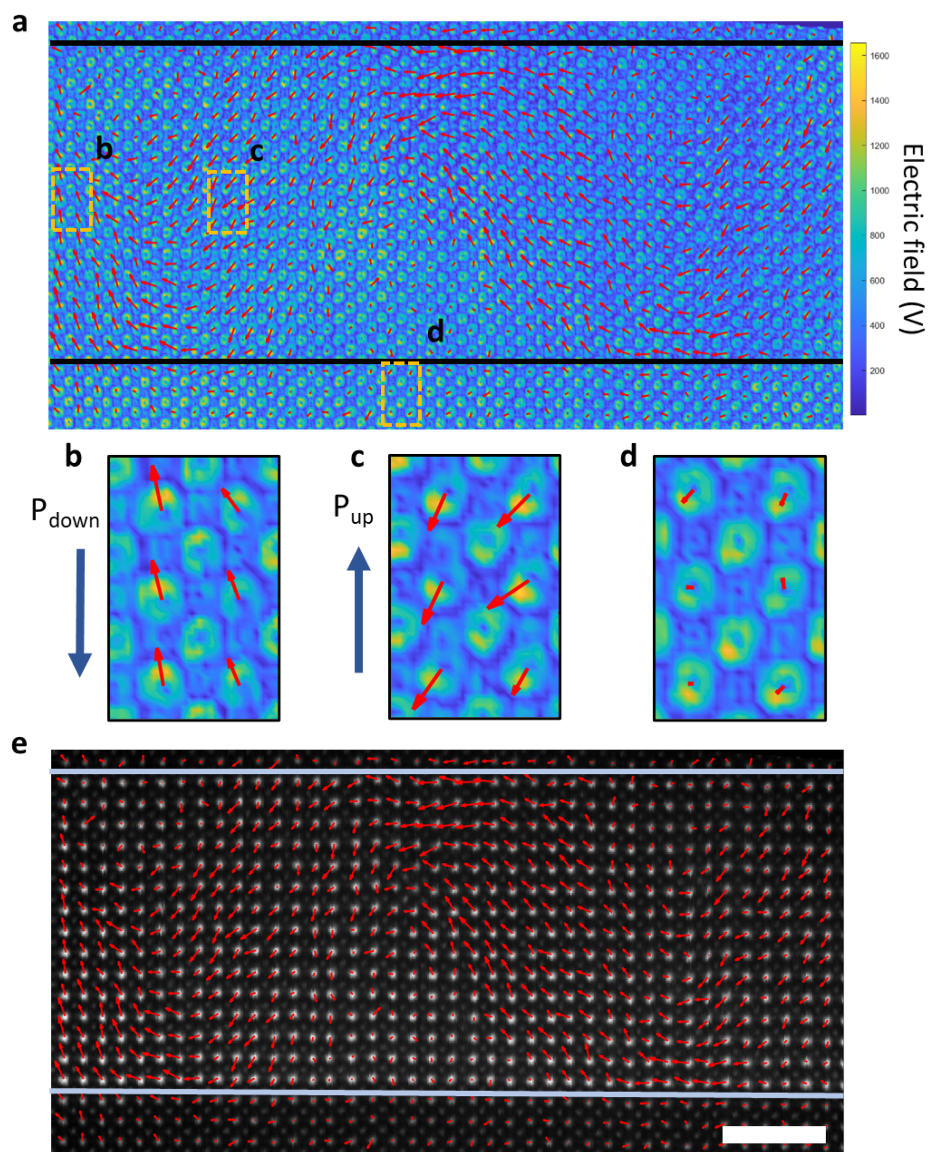

Figure 4.4: **Average A-site electric field.** **a**, The high convergence angle electric field map with a vector map of average lead column electric field overlaid in red. **b-d**, Zoomed-in views of the electric field from the highlighted regions (same regions as fig. 4.2**c-e**). **e**, The vector map of the average Pb column electric field overlaid on a reconstructed HAADF image.

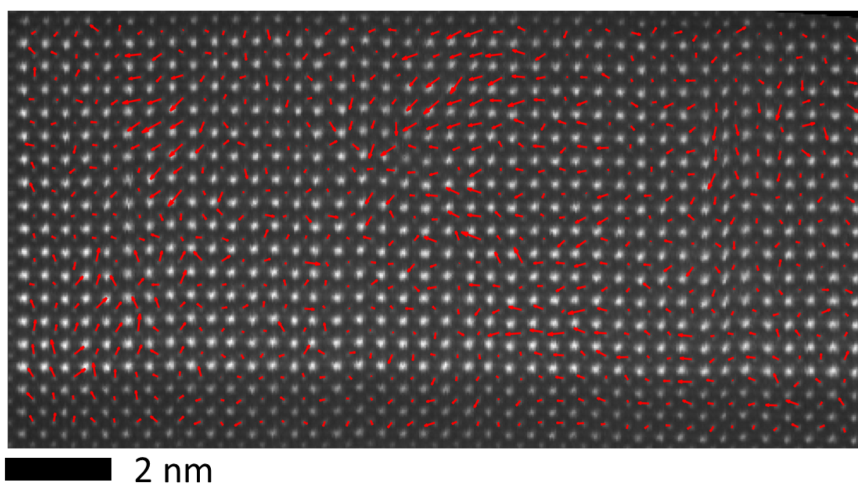

Figure 4.5: **Average Ti/O site electric field.** The simultaneously collected HAADF image with the vector map of the average electric field of the Ti/O columns is overlaid in red.

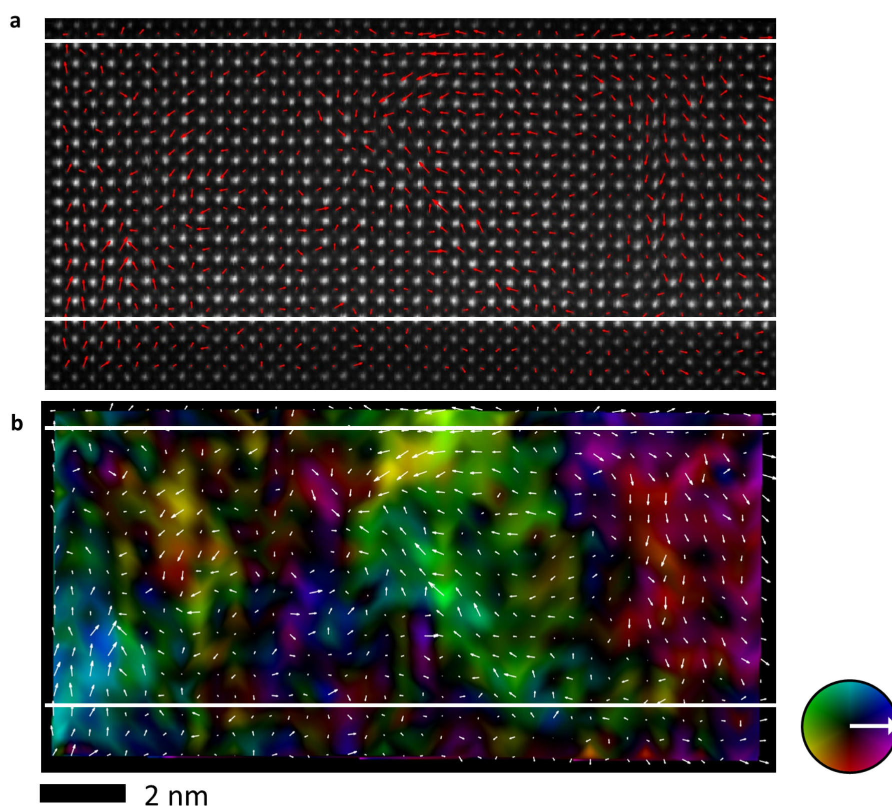

Figure 4.6: **Unit cell electric field.** **a**, Vector map of the average electric field of each unit cell overlaid on a HAADF image. **b**, The same vector where the background now represents the magnitude and direction of the vector according to the color wheel.

previous studies may have a common origin in the covalent bond between the A-site and oxygen atoms [139]. It also provides an explanation for why the same electric field bias is not consistently observed on titanium/oxygen columns. Although titanium 3d orbitals also hybridize with oxygen 2p, the hybridization is not driven by a localized lone pair. First principles calculations have shown weaker charge separation near B-site columns compared to A-site columns which would make the electric field asymmetry weaker compared to A-site columns [4]. Similar studies of 2D materials have also shown that 4D STEM is highly sensitive to bonding structure which can be revealed by changes in the electric field or charge density [115, 120, 121].

4.4 Nanometer scale E-field

To study the electric field at the nanometer scale, we formed an electron probe with a 2.4 mrad semi-convergence angle, resulting in a probe FWHM of 4 Å, close to the (100) lattice spacing in both STO and PTO (fig. 4.1b). In this beam condition, the diffraction disks are well separated. A virtual bright-field image of a PTO layer in this beam condition is shown in fig. 4.7a and a virtual dark field image from the ($\bar{2}00$) diffraction disk is shown in fig. 4.7b. We measured the electric field only from the momentum change of the center disk to exclude any effects due to polarization or strain that may shift the diffraction disks. A map of the electric field in this region with 1.5 Å step size is shown in fig. 4.7c, with the color representing the direction and the saturation representing the relative magnitude. With a maximum value of only 25 V inside the PTO layer, the projected electric field measured in this condition is much weaker than the field measured with the picometer probe and it also does not show the same vortex pattern as before. Instead, the electric field is separated into regions that are mostly oriented in-plane, along [100] or [$\bar{1}00$] in the middle of the PTO layer. The electric field at the edge of the PTO and in the adjacent STO layers is not reliable due

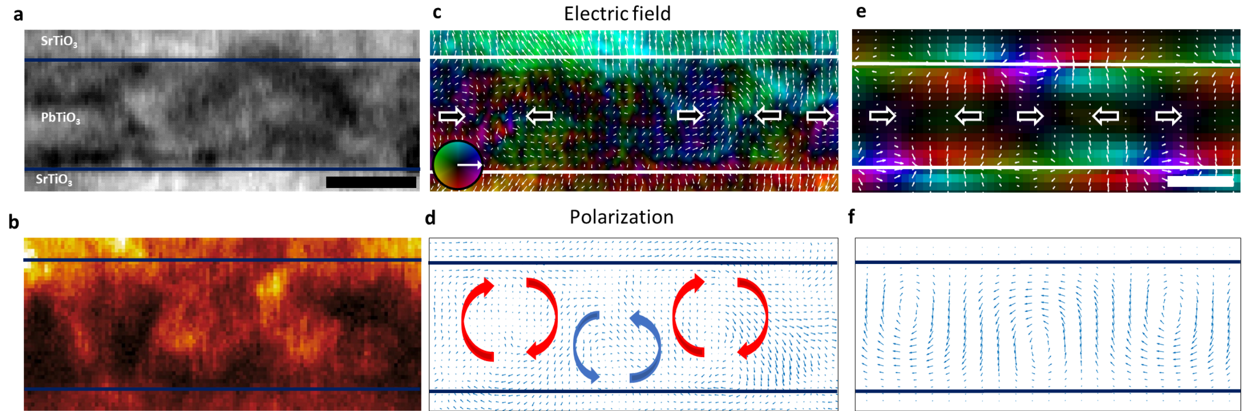

Figure 4.7: **Nanoscale electric field.** **a**, A bright field image reconstructed from the 4D STEM data. **b**, A virtual dark field image from the $(\bar{2}00)$ disk. **c**, The electric field mapping from the central disk. The background represents the magnitude and direction of the field based on the inset color wheel, the vector map is overlaid in white. **d**, The polarization mapping from the same dataset shows this region covers three vortices. **e**, Phase-field simulation of the electric field. **f**, Phase field simulation of the polarization. The scale bar on **a** is 5 nm and applies for experimental data **a-d**. The scale bar on **e** is 5 nm and applies for simulated data **e** and **f**. The larger arrows overlaid on the figure show the general direction of the electric field/polarization in the surrounding region.

to a shift in zone-axis alignment between adjacent layers of the superlattice that affects the intensity distribution in the CBED pattern.

The polarization of the PTO layer can also be measured directly in this beam condition based on changes in the symmetry of the intensity distribution in conjugate pair diffraction disks in each diffraction pattern [124, 169]. Shifts in the diffraction disk positions are related to changes in the lattice parameter induced by strain, not the electric field. However, the intensity distribution within the $(200)/(\bar{2}00)$ and $(002)/(00\bar{2})$ diffraction disks can be used to map the polarization. In centrosymmetric unit cells the diffraction intensity generally obeys Friedel's law, which states that the diffraction intensity in conjugate disks should be symmetric, $f(\mathbf{k}) = f(-\mathbf{k})$. However, the spontaneous polarization in PTO breaks this centrosymmetry, resulting in asymmetric intensity in conjugate pair diffraction disks. We quantify the asymmetric intensity using the intensity center of mass (COM) shift averaged between conjugate pair disks to generate a vector field that shows the polarization. In detail,

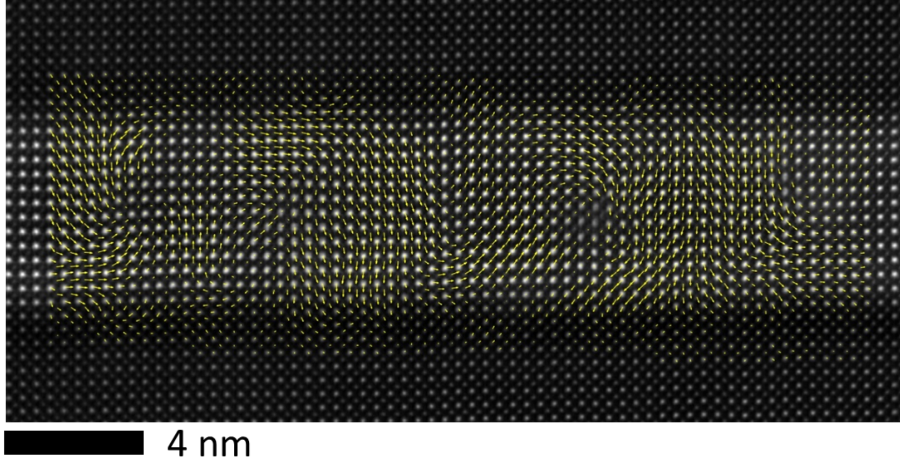

Figure 4.8: **Polarization map.** Conventional atomic structure polarization mapping from a region nearby to where the 4D STEM data in fig. 4.7 was captured.

for the polarization along [100], we first calculate the COM of (200) and ($\bar{2}00$) diffraction disk separately in all CBED patterns. The (200) and ($\bar{2}00$) COMs are then averaged together to get a combined (200)/($\bar{2}00$) COM position for each CBED. A reference position is calculated as the average of all (200)/($\bar{2}00$) COM positions in the entire data set. The polarization along [100] at each scanning position is then taken as the shift of the (200)/($\bar{2}00$) COM away the reference. The polarization along [001] is calculated analogously using the (002) and ($00\bar{2}$) diffraction disks. The polarization in this region is shown in fig. 4.7d and exhibits the characteristic vortex pattern. Polarization measured using conventional displacement mapping from an adjacent region also showed polarization-vortex structures (see fig. 4.8).

4.4.1 Phase field simulations

Phase-field modeling was also performed to model the evolution of the ferroelectric superlattice polarization and electric fields, where the polarization is obtained by solving the time-dependent Ginzburg-Landau (TDGL) equations,

$$\frac{\partial P_i(\mathbf{r},t))}{\partial t} = -L\frac{\delta F}{\delta P_i(\mathbf{r},t)}, (i = 1, 2, 3), \tag{4.1}$$

Where L, $\mathbf{r}$, and t represent a kinetic coefficient related to domain wall mobility, spatial vector, and time, respectively. The polarization field is represented by P_i and the free energy functional (F) contains electrostatic, elastic, Landau bulk, and gradient energy contributions, i.e.

$$F = \int_V (f_{Landau} + f_{elastic} + f_{electric} + f_{gradient})dV \tag{4.2}$$

The exact expressions and material properties for each energy contribution can be found elsewhere in the literature [48, 172–174]. Arising from the inhomogeneity in elastic constants in the PTO/STO superlattice, a spectral iterative perturbation method was used to solve for mechanical equilibrium [175]. It should also be noted that mechanical and electrostatic equilibrium was assumed to occur instantaneously compared to the polarization equilibrium. The lattice constants of STO, PTO, and DSO were all taken from the literature [173, 174, 176].

The system size of the simulations was taken to be $200\Delta x \times 200\Delta y \times 120\Delta z$ where $\Delta x = \Delta y = \Delta z = 0.5nm$. The thickness of the superlattice was divided between substrate ($20\Delta z$), film ($94\Delta z$), and air ($6\Delta z$). Random noise was utilized to initiate the simulation process and the simulation continued until the free energy of the system equilibrated.

The corresponding total electric field and polarization for $(PTO)_{16}/(STO)_{16}$ superlattices from phase-field simulations are shown in fig. 4.7e and f, respectively. Comparing the electric field from experiment and simulation, the alternating in-plane alignment in the experimental electric field is visible near the center of the simulated electric-field map. The out-of-plane electric field component visible at the edges of the PTO layer in the phase-field simulation is likely not visible in the experiment due to the signal being overshadowed by the shift in zone-axis between superlattice layers. The width of the polarization-vortex structures is measured to be approximately 5.5 nm in experiment and 6 nm in simulation (see fig. 4.9). Taken

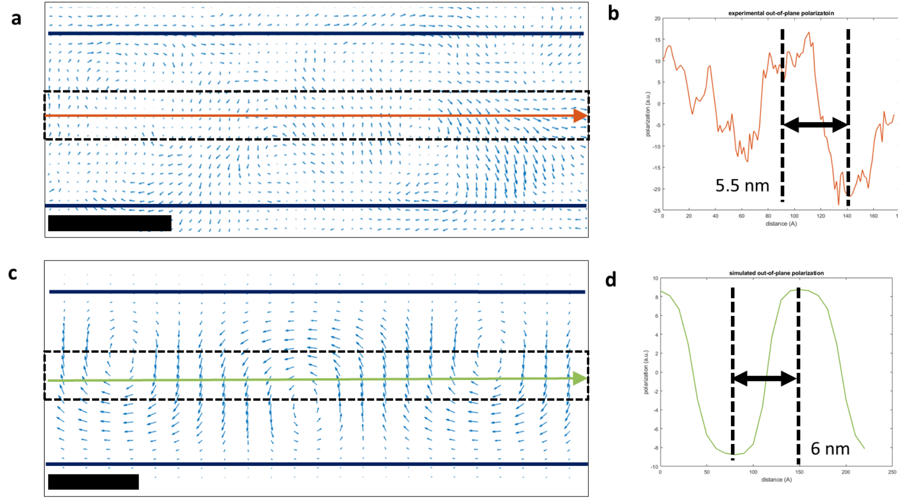

Figure 4.9: **Polarization correspondence a**, Experimental polarization map measured with low convergence angle 4D STEM. **b**, A line profile of the out-of-plane polarization from the region marked in a. The approximate width of the polarization vortex of 5.5 nm. This is measured from the middle of the polarization up region to the middle of the polarization down region. **c**, The polarization from phase-field simulation. **d**, A line profile of the out-of-plane polarization from the region marked in **c**. The width of the polarization vortex in simulation is approximately 6 nm. Scale bars on **a** and **c** are 5 nm.

together, the electric field and polarization measured with the nanoscale probe matches with results from phase-field simulations. This indicates that the electric field measured with a larger probe size follows the strain and electrical boundary conditions determined by the superlattice structure, as it is in phase-field simulations, and is more representative of the total electric field in the sample. This is also in agreement with previous publications that report the electric field distributions in the $(PTO)_{12}/(STO)_{12}$ superlattice under similar beam conditions [124].

4.5 Conclusion

These differences observed when switching between the picometer and nanometer electron probes are due to changes in the interaction volume in the sample. Variations in the electric

field that occur over length scales much smaller than the width of the probe will sum together incoherently and thus do not generate a change in probe momentum. For the nanometer-sized probe, the electric-field bias of atomic columns is not detectable since the probe covers several atomic columns at a time, many with a field that is almost rotationally symmetric. Therefore, only long-range effects that influence the electric field in the entire film are detected with the nanometer sized probe. For the picometer-sized probe, the electric-field bias of individual atomic columns induced by the hybridization of lead 6s lone pair electrons is detectable because of its smaller width and interaction volume. This effect is also much stronger in comparison to the total electric field and will dominate the overall pattern, drowning out any affect from the total electric field. Interestingly, when the electric field measured with a picometer-sized probe is averaged over a whole unit cell, it does not match the result from the nanometer probe, even though the FWHM of the probe used to measure the field in fig. 4.7b is roughly equal to the width of one unit cell. Therefore, even when integrating the signal from the picometer probe over an area roughly equal to that of a nanometer probe, they are not equivalent. Although we have discussed the differences mainly in terms of probe width, this indicates that other factors that change with convergence angle, such as the depth of focus and channeling may affect the interaction as well.

In summary, we have applied 4D STEM electric field imaging to a $(PTO)_{16}/(STO)_{16}$ superlattice with both a picometer-sized and nanometer-sized electron probes and observed different patterns in the electric field at atomic and nanometer scales. The electric field measured by a picometer-sized probe shows a vortex pattern and is mainly determined by the asymmetry introduced to lead atomic columns by bonding configuration of lead 6s lone pair electrons which generates a dipole in each unit cell. On the other hand, the electric field measured with a nanometer-sized probe follows the total electric field set by the electrostatic and elastic boundary conditions of the film. These differing configurations are caused by a change in the interaction volume of the probe which causes the dominant contribution to the electric field image to shift from the dipole of individual unit cells to the total electric field

in the material when the probe size increases. These findings highlight the versatility of 4D STEM in studying both the bonding structure and electrostatic properties of ferroelectric materials and elucidates the mechanisms that cause the differing electric field configurations observed in previous studies.

Chapter 5

Charge density imaging of a $PbTiO_3$-$SrTiO_3$ interface

5.1 Introduction

Measuring and controlling the charge state of specific elements and even specific atoms in a material system is an important part of determining the system's overall behavior. The charge state determines an atom's ability to form bonds and accept or donate additional charge which both contribute to functional properties such as conductivity in electronic materials or reactivity in catalysts. In oxide heterostructures, coupling between the charge and other degrees of freedom, including the lattice strain and polarization, will be an important part of any oxide based electronic devices [22].The precise control of a semiconductor's conductivity through the addition of dopant atoms forms the foundation of all modern semiconductor devices [177–181]. As semiconductor devices have shrunk down to nanometer scale and the control of layer-by-layer deposition in oxides has advanced, high resolution charge state characterization has become increasingly important. In catalysis, the charge

state of surface atoms is important in determining the reactivity, and thus the effectivness, of the material. For example, the orbitals of gold atoms on the surface of nanoclusters are transformed so that the bonding is generally more covalent than metallic which facilitates catalytic activity [182]. There are several techniques for measuring the charge state of a specific element, including XPS [183], XAS [184], EELS [185], and scanning probe microscopy [186–188]. Spectroscopic methods depend on the absorption or emission of characteristic x-rays; in these techniques, spectroscopic fine structure of specific emissions is sensitive to the bonding configuration and thus the charge state of the element. X-ray based methods typically have only micron resolution. EELS can achieve 1Å resolution in an aberration corrected STEM, but the correlation between spectral features and charge state does not paint a clear picture of the charge state of an element. Scanning tunneling microscopy has recently been used to image the bonds and electron density of atoms and molecules, but requires an atomically flat conducting surface [186–188].

As discussed in the previous chapters, 4D STEM is an effective technique for studying the charge state of a materials with atomic resolution. In Ch. 3, 4D STEM is used to detect the change in the charge state of Ti/O and Fe/O columns across a BFO/STO interface. In this case, comparisons are drawn within the same material to show the change in charge state approaching the interface from both sides. In this chapter, we aim to examine how the change in the bonding structure between $PbTiO_3$ (PTO) and $SrTiO_3$ (STO) is reflected in 4D STEM charge density images and the charge state of different elements as measured by Bader charge analysis. Since both materials contain Ti, particular focus is paid to the charge state of Ti across the interface. To isolate the Ti column during experiments, samples are prepared from both (100) and (110) projections so that the Ti column can be examined both with and without an overlapping O column. Despite sharing the same nominal valence state (4+) in both materials, it is shown that experimental 4D STEM can reveal slight changes the Ti charge state due to the differences in bonding characteristics of these materials.

5.2 PTO/STO (100) projection

We start by examining bulk PTO in comparison to STO and BFO. 4D STEM data was collected on a JEOL JEM-ARM300CF double aberration corrected S/TEM at 300 kV; diffraction patterns were recorded with either a Gatan OneView camera at the speed of 300 frames-per-second (fps), with 512x512 pixels for each frame (STO and BFO) or a Gatan K2 IS camera with a speed of 1200 fps with 480x287 pixels for each frame (PTO). The semi-convergence angle was 32 mrad. For comparison, HAADF, electric field, and charge density images are shown for STO, BFO and PTO in fig. 5.1. Note that, in STO the electric field is radially distributed around each Sr, Ti and O atom as demonstrated by the colors and arrows, suggesting the high symmetry of local field around ions in STO, meanwhile in BFO, the electric field surrounding Bi is polarized diagonally towards the bottom left, inversely related to the atomic displacement of Bi. In PTO, because of the dominating Jahn-Teller effect, the atomic structure adopts a tetragonal phase with the c/a ratio of 1.06 [189], the electric field does not exhibit as much distortion as in BFO. However, features that are not as pronounced in the images and electric field maps are revealed in more detail in the charge density. For example, the difference in the distortion of the oxygen octahedron is clearly visible when comparing the charge density of STO, BFO, and PTO. In STO, the oxygen columns appear in-line with the adjacent Sr or Ti columns because there is no octahedral distortion. In BFO, the octahedron is rotated and the oxygen column is split, resulting in an elongated oxygen column with reduced intensity. In PTO, the octahedron is distorted along the growth direction (vertical direction in the images), but are not split as in BFO, so they retain stronger intensity as in STO.

HAADF and 4D STEM data collected from a PTO/STO interface are shown in fig. 5.2. Heavy atom positions are located in the HAADF image by 2D gaussian fitting that is further refined based on the charge density image. Although light elements such as oxygen cannot be detected in HAADF image, they appear in the charge density image as weak positive charge

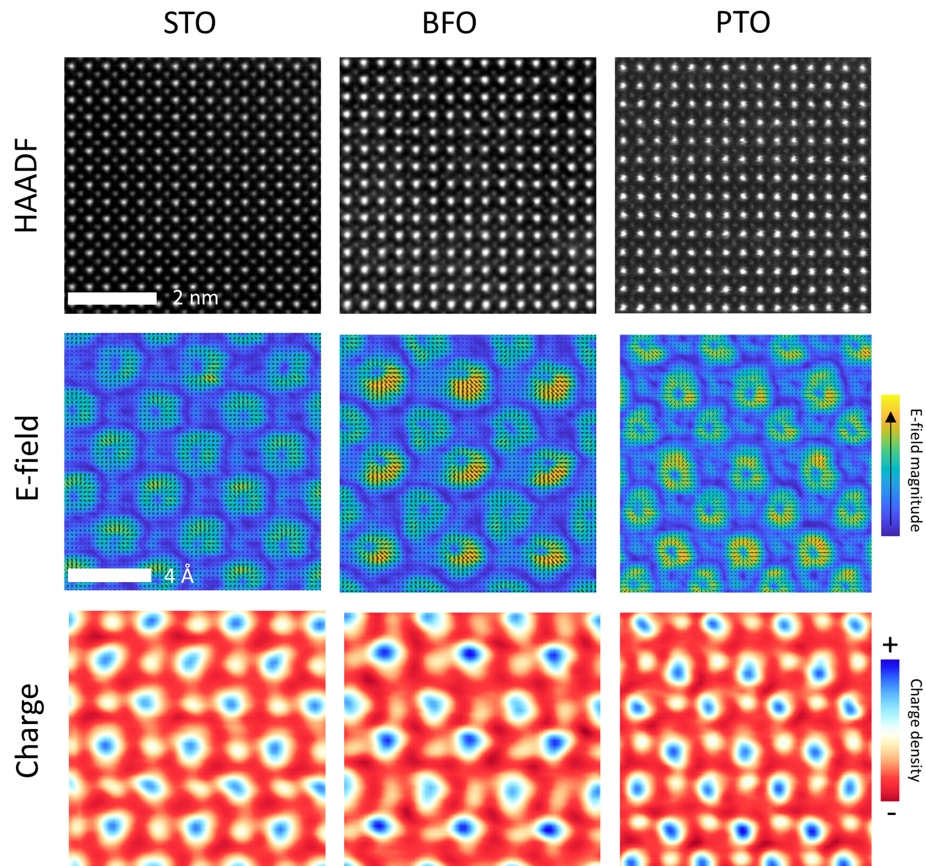

Figure 5.1: **Comparison of perovskites.** HAADF, E-field, and charge density images for STO, BFO and PTO. The electric field and charge density scales have been equalized between all three image sets. The scale bar in the STO HAADF image applies to all HAADF images. The scale bar in the STO E-field image applies to all E-field and charge density images.

centers. Based on the knowledge that oxygen atoms are near the face center of a perovskite unit cell in the (100) projection, we thus search for the local intensity maxima in the area between the adjacent A sites and B sites to identify oxygen atoms, as shown in fig. 5.2b. With all atoms located, we can calculate the charge state by integrating the charge density within a region surrounding each nucleus according to Bader charge analysis. Histograms of the integrated charge for each species are shown in Fig. 3c along with gaussian fitting of each distribution. The mean charge state of Pb, Sr, Ti/O, and O columns are 0.91e, 0.56e, 0.79e, and -0.66e, respectively. Considering that both Sr and Pb have a formal valence state of 2+, the large difference in charge state here indicates that there are likely other factors at play that influence the integrated charge value. The nuclear charge of Pb ($Z = 82$) is more than double that of Sr ($Z = 38$) which would contribute to stronger scattering and thus a higher measured positive charge. This is also supported by previous simulation studies [190]. However, there are also changes in the bonding structure between STO and PTO that may contribute. Bonding between Sr and O is ionic [191] while bonding between Pb an O has more covalent character [1, 4], so there should be stronger charge transfer from Sr than Pb which should yield the opposite trend in the measured charge. Given that the effects of the nuclear charge and ionic charge transfer cannot be separated, it is difficult to draw conclusions based on comparisons between different atomic species in different materials.

On other hand, bonding between Ti and O in both STO and PTO is covalent [192, 193]. Hybridization between transition metal 3d and oxygen 2p orbitals is important for determining the symmetry of perovskite unit cells. Therefore, the charge state of titanium is important in determining the overall properties of the material. The formal valence states of Ti and O in both STO and PTO is 4+ and 2-, respectively, so the combined Ti/O column is 2+ overall. This is equal to the formal valence state of both Pb and Sr, but there are several factors which could account for the intermediate value of the charge state measured from 4D STEM. Although the combined Ti/O ($Z_{\mathrm{Ti+O}} = 30$) column has a comparable nuclear charge to Sr, the greater charge transfer from Ti to O atoms and change in bond type may explain

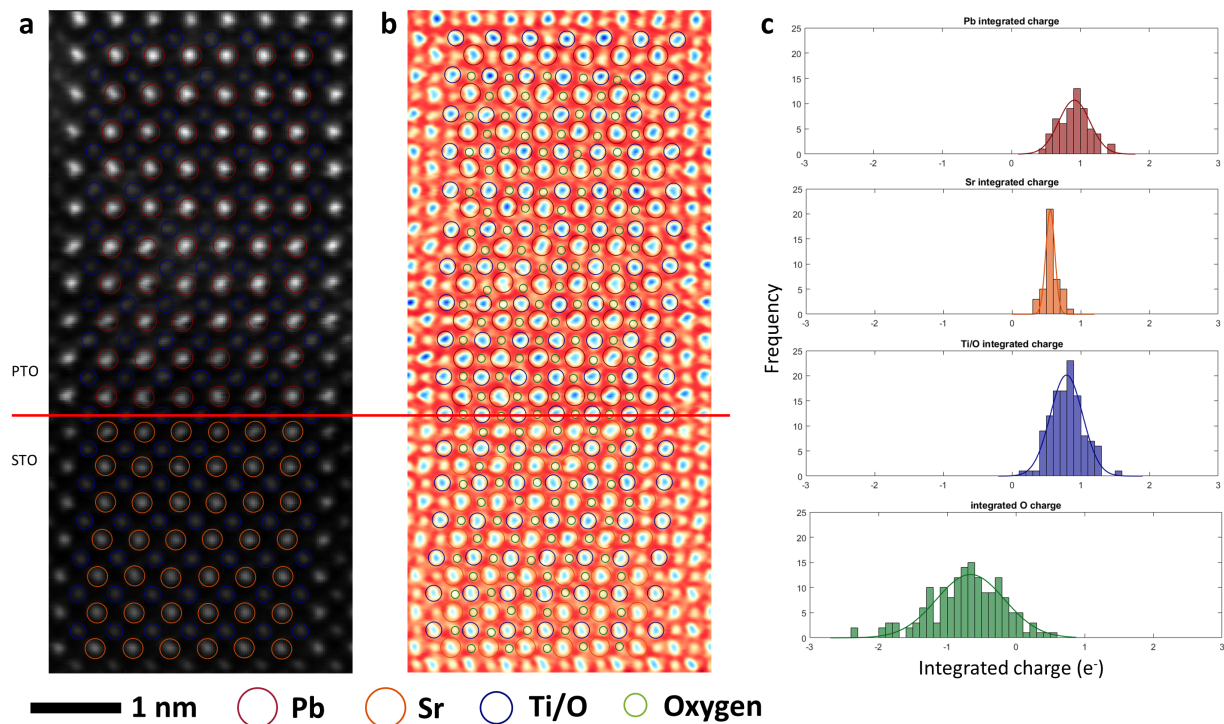

Figure 5.2: **(100) PTO/STO Interface. a**, Simultaneously collected HAADF image of the (100) PTO/STO interface. Atomic positions of the cations are marked with colored circles. **b**, The associated charge density image. Cation and oxygen positions are marked. **c**, Histograms of the integrated charge for each type of atomic column based on Bader charge analysis. The distribution in each case is fit with a gaussian; fitting results are overlaid on each histogram.

the higher charge state compared to Sr. The inclusion of oxygen in the Ti/O columns should reduce the charge state of the Ti/O column, but the hybridization of Ti takes place between all 6 atoms making up the oxygen octahedron, only 2 of which are in Ti/O column, so the effect may not be as strong as simple summation of the formal valence states would suggest. This could be another reason for the slightly higher charge state of the Ti/O column compared to the Sr column. When comparing with the charge state of Pb, the significant difference in nuclear charge again complicates the analysis.

5.3 PTO/STO (110) projection

In order to isolate effect of the change in bonding structure on Ti atoms alone, we prepared a sample which is rotated so that [110] STO is oriented along the beam direction. This is done by cutting the specimen at 45° relative to the edges of the original sample chip prior to mechanical polishing. A HAADF image in this orientation is shown in fig. 5.3a. 4D STEM data was collected from this region and the charge density is shown in fig. 5.3b. In this orientation, the Ti atom is not overlapped with oxygen and the distortion of the oxygen octahedron is apparent based on the zig-zag pattern in the Ti/O rows in the charge density image. Bader charge analysis was applied to the data; the integration regions are illustrated in fig. 5.3c. While the integrated charge of Ti in the first PTO row is 0.54e, the average in PTO is 0.42e $\pm$ 0.07e. For comparison, the average integrated charge of Ti in STO is 0.55e $\pm$ 0.08e. To examine the structural polarization, the displacement between the Ti adjacent O columns projected along the [001] direction was measured in fig. 5.3e. Combining the integrated charge and the polarization, we can see the higher integrated charge in the first PTO layer is also correlated with a lower oxygen octahedral distortion, as indicated by the lower Ti-O displacement measured in the first PTO layer when compared to the remaining layers. The combined higher integrated charge and the lower structural distortion in the

first PTO layer likely indicates that the bonding configuration of this layer are a hybrid of that in STO and PTO. This contrasts with the shared interface layer where the integrated charge and displacement are characteristic of STO alone.

This change in the charge state of Ti across the PTO/STO interface also agrees with results from first principles density functional theory calculations. Using conventional Bader charge analysis calculated from the full charge distribution, the charge state of Ti in bulk PTO was found to be 9.84e compared to 9.90e in bulk STO. The higher charge state of Ti in STO compared to PTO is also supported by calculations of the Born effective charge, where the charge of Ti in PTO and STO was found to be 6.38e and 7.39e, respectively. The trend in these results is also supported by other previously published first principles studies [194–197]. Notably, the increased charge state of Ti in PTO near the interface is also supported by the results of ref. [197]. According to ref. [197], the Born effective charge of Ti in PTO is higher when a cubic structure is used than when a tetragonal structure is used. The reduction in the polarization near the interface in fig. 5.3e is also indicative of a transition towards cubic symmetry. Taken together, this lends further support to the notion that the change in charge state of Ti as measured by 4D STEM reflects the change in bonding configuration.

Electron energy loss spectroscopy (EELS) was also performed across the PTO/STO (110) interface. EELS fine structure, and the associated X-ray absorption fine structure, is often correlated with the formal valence state of specific atomic species, especially transition metals such as Ti [75, 78–80, 198–200]. However, the fine structure is actually determined by a variety of factors, including the coordination number, bond length, bond angle, and symmetry that all affect the exact energy level of the hybridized bonding orbitals. Thus EELS fine structure is not a direct measurement of the charge state of the atom. Across the PTO/STO interface, despite Ti maintaining a valence of 4+, clear changes in the Ti $L_{2,3}$ and O K edge fine structure are visible. An EELs spectrim image was collected from the region shown in fig. 5.4a. Example spectra are shown in Fig. 5.4b and c; the background

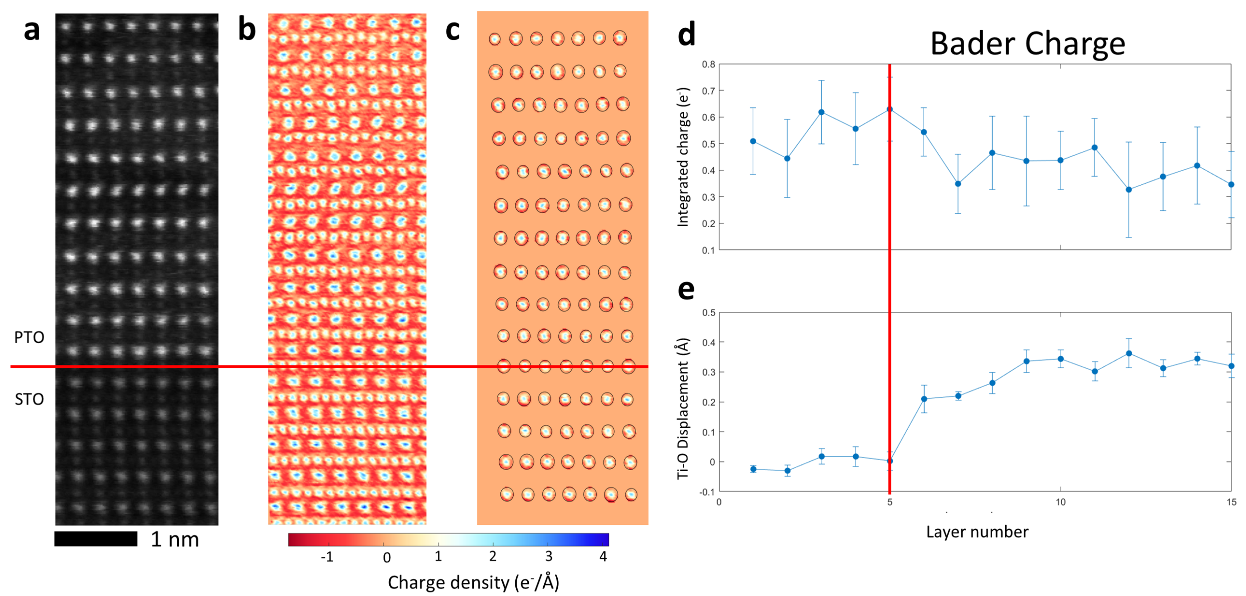

Figure 5.3: **(110) PTO/STO interface. a, b**, HAADF and charge density map from PTO/STO (110). **c**, Regions selected for Bader charge analysis. **d**, Integrated charge of Ti columns for each layer across the interface. **e**, Ti-O displacement along [001] direction. Error bars in **d** and **e** are the standard deviation of integrated charge and displacement of each layer, respectively. The Ti column in PTO shows slightly lower charge than the Ti column in STO.

has been subtracted based on a power-law fitting. In the case of Titanium, the $L_{2,3}$ edges are both split into t_{2g} and e_g peaks which are clearly separated in STO, but merge together in PTO without any clear change in intensity ratio. Qualitatively, this points to a change in the Ti bond symmetry via distortion of the oxygen octahedron [78, 80], but this can already be observed based on the Ti displacement. The oxygen K edge has three peaks, labeled A, B, and C in Fig. 5.4c, which can be identified in STO. However, in PTO, the A and B peaks are smeared together and the C peak is slightly red shifted. Peaks A and B are correlated with the bonding between O 2p and Ti 3d orbitals, so a shift here is expected due to the distortion of the oxygen octahedron. The C peak originates from the bonding between O and A-site cations, so the shift is likely due to the differences between in the electronic structure of the Sr and Pb atoms [78, 200].

To estimate the charge state of Ti, we quantitatively analyzed the changes in Ti $L_{2,3}$ peaks by applying the fine structure fitting algorithms described in Ref [75]. By averaging the peak positions on each side of the interface, we observed that both the L_2 and L_3 e_g peaks are red shifted in PTO compared to STO by 0.43 eV and 0.32 eV, respectively. The L_2 t_{2g} peak is blue shifted by 0.37 eV while the L_3 t_{2g} peak remains stationary across the interface. Taken together, these all point to a change in the hybridization between Ti and the oxygen octahedron, but not a clear change in the valence state; Ti^{3+} is associated with a general red shift of the $L_{2,3}$ peaks compared to Ti^{4+}, especially the L_3 t_{2g} peak [33, 201].

5.4 Image simulations from bulk materials from (110) projection

To understand how the atomic structure and electron probe size may effect Bader charge analysis based on 4D STEM charge density images, we completed a series of multislice simula-

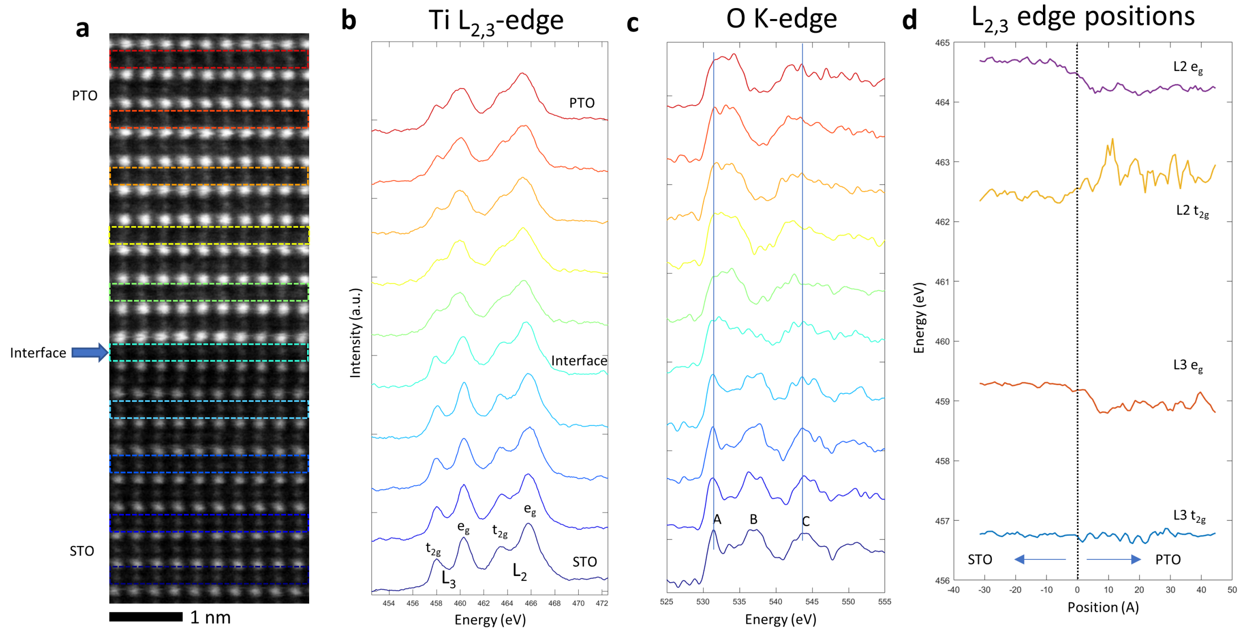

Figure 5.4: **EELS from (110) PTO/STO. a**, HAADF image of the PTO/STO interface with polarization down. **b**, Evolution of the Ti $L_{2,3}$ edge across the interface. **c**, Evolution of the O K-edge across the interface. **d**, Peak positions of the t_{2g} and e_g peaks for the $L_{2,3}$ edges across the interface

tions using the abTEM software package [202–204]. abTEM utilizes the multislice algorithm to simulate TEM and STEM images. In multislice simulations, the electrostatic potential is generated using the independent atom model (IAM), where the potential for each atom is calculated from predefined scattering factors and then the potential from all atoms are summed together to get a potential map covering the simulated structure. Since each atom is treated independently, this does not account for any of the bonding characteristics of the material that may influence the distribution of valence electrons. When simulating conventional TEM/STEM images for structural analysis, this is generally sufficient; the change in the electrostatic potential due to valence electrons is small so image contrast is dominated by scattering from the nucleus and cores shell electrons. However, recent quantitative studies of HRTEM images and off-axis holography measurements of 2D materials have demonstrated that the IAM does not always yield the correct image contrast [59, 205, 206]. For example, evidence of charge transfer in nitrogen doped graphene and hexagonal Boron Nitride has been observed in HRTEM images [59]. Bright-field STEM imaging and TEM imageing are

linked via reciprocity [207], therefore, similar features should be visible in 4D STEM and DPC images as well since both utilize the bright field disk.

Structures models of STO and PTO projected along (110) orientations were generated using the Atomic Simulation Environment with thickness of 5.5 nm [208]. The projected potentials based on the independent atom model were generated using the structure factors defined in Ref. [209]. The projected potentials are shown in fig. 5.5. The electron probe was constructed with parameters to match experimental conditions in the JEOL JEM-ARM300CF (Energy = 300kV, C_3= 1 μm, C_5 = 1 mm). 4D STEM data was then simulated with a step size of 0.16 Å. The E-field images and charge density images were calculated and calibrated using the same methods as in experiment. The resulting charge density from simulated 4D STEM measurements is also shown in fig. 5.5. Some differences between experimental and simulated data are immediately apparent. In the simulated charge density image, the distortion of the oxygen octahedron is visible as splitting of the Pb/O column while it is not in experimental results. In addition, the band of negative charge that appears between Ti and O columns in the Ti/O row is not clearly visible in experimental results. Both of these differences can likely be attributed to lattice vibrations which increase the apparent size of the atomic columns and are not included in the simulations due to the computational cost.

Bader charge analysis was applied for the Ti atomic columns in simulated data. In PTO, the average integrated charge of the Ti columns was found to be $2.05 \pm 0.010e$, where the error is the standard deviation of the integrated charge from all Ti columns in the field of view. In STO, the average integrated charge was $2.03 \pm 0.012e$. These values are higher than those observed in experiment likely due to noise in the diffraction pattern images, as demonstrated in Ch. 2. The fact that these values are so close fits with our expectations from the construction of the electrostatic potential using IAM; under IAM, a Ti atom in STO is no different from a Ti atom in PTO, so they should have the same charge. Therefore, it is clear that conventional image simulation methods using IAM does not account for this

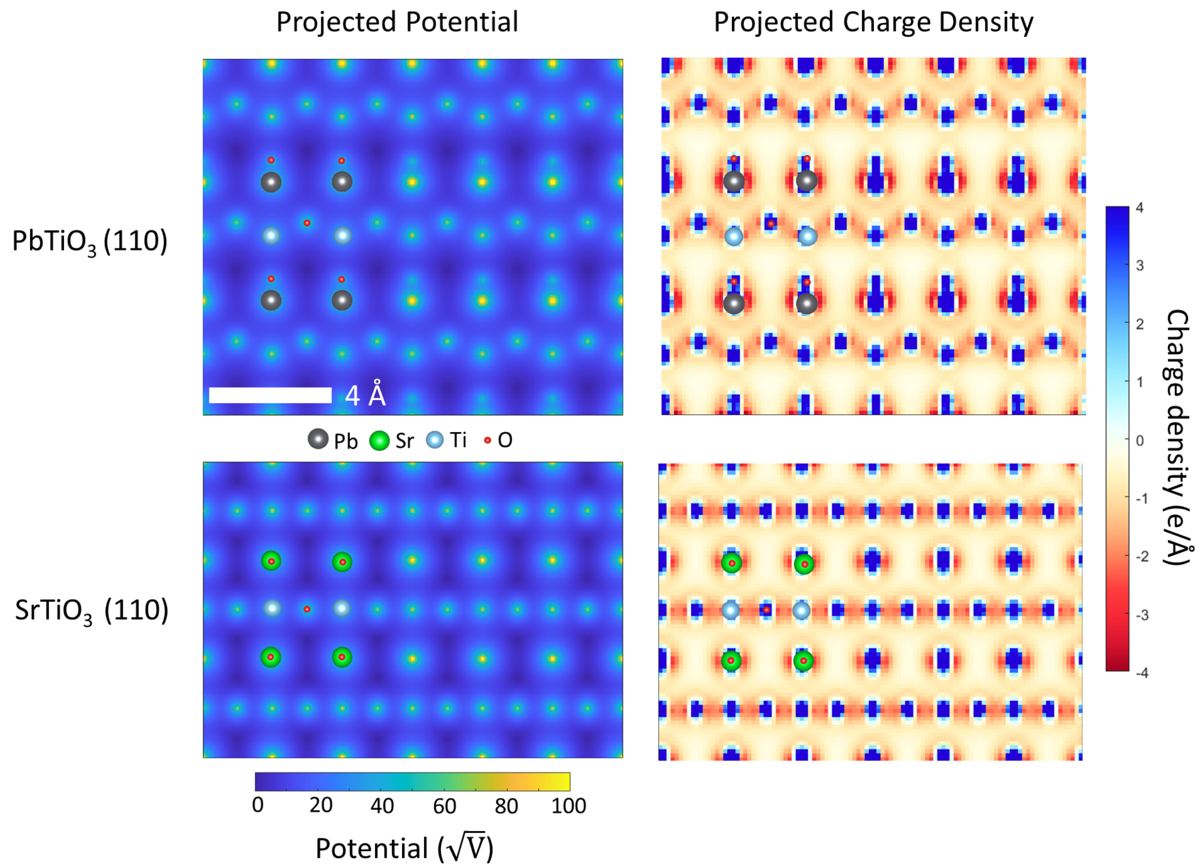

Figure 5.5: **Imaging simulations.** The projected electrostatic potential used in imaging simulations from (110) PTO and STO and the charge density calculated from simulated 4D STEM data. The structure models of STO and PTO are overlaid.

change in the charge state of Ti which is detected in experimental 4D STEM data. Similarly, we can rule out any changes in structure that may effect the Bader charge measurement since the measurement using IAM results in nearly the same values in both materials.

5.5 Conclusion

In conclusion, the changes in Ti bonding characteristics across a PTO/STO interface were examined using Bader charge analysis in 4D STEM. First principles calculations have predicted that Ti in each material should have a different charge state, but conventional experimental methods, such as analysis of the EELS near edge fine structure did not provide a clear picture of the change in charge state. Using a sample prepared from the (110) projection to isolate the Ti column, we have demonstrated the change in charge state between PTO and STO is clearly visible in 4D STEM charge density images with the application of Bader charge analysis. A drop in the charge state moving from STO to PTO was observed within the first two unit cells of PTO. This further demonstrates the sensitivity of 4D STEM Bader charge analysis to the charge transfer and bonding configuration in materials at the atomic scale and the associated changes in charge state of individual atomic columns. This opens the door for the application of atomic resolution 4D STEM to other materials where characterization of the charge state is critical to understanding the overall properties.

Chapter 6

Summary and outlook

In summary, we have presented a systematic study of the electronic properties of perovskite ferroelectric heterostructures by leveraging aberration corrected STEM and fast pixelated electron detectors to to directly image the electric field and charge density distribution in these materials with atomic resolution. After introducing the process of electric field imaging with 4D STEM, we demonstrated that the technique can be extended to samples that are outside the typical thickness range, up to 15-20 nm, while still maintaining a qualitatively accurate electric field distribution. This enables us to extend the electric field imaging technique to a wider variety of samples and materials than previously accepted. For example, while the 5 nm restriction that is typically placed on sample thickness is only accessible with mechanical polishing, samples prepared by FIB can routinely be fabricated with 20 nm thickness and therefore could be utilized with 4D STEM electric field imaging with these new findings [210]. Next, we studied a series of ferroelectric-insulator heterostructures, revealing new phenomena in each case by developing new analysis methods for 4D STEM electric field and charge density data. In a $BiFeO_3$-$SrTiO_3$ interface, we showed that there is charge accumulation at the interface through a combined analysis of the atomic structure, electric field, and charge density. Atomic resolution electric field images revealed a weakening dipole

across the interface which was supported by measurements of the structural polarization. Using high resolution charge density images that contain information from both the positive nuclear charge and the negative inter-atomic electron distribution, we were able to show that the dipole and integrated charge of B-site species in each unit cell changes across the interface with a different rate than the atomic structure alone might suggest [139]. This proivdes a mechanistic explanation for the appearance of a 2D charge-carrier gas that has been predicted at several ferroelectric-insulator interfaces. We then studied the electric field distribution in $PbTiO_3$-$SrTiO_3$ superlattices using STEM probes formed with both high and low convergence angles in order to understand the origin of varying electric field features that have been observed in ferroelectric materials. Using the high convergence angle probe, we observed an asymmetric electric field surrounding lead columns which we attributed to the off-center lone pair electrons that are part of the hybridization between lead and oxygen valence electrons. In the low convergence angle case, we found that the electric field measured with 4D STEM can be attributed with the total field of the system as determined by the boundary conditions. These findings elucidate the asymmetric electric field features that had been previously observed in other publications and also demonstrates how the probe size can dramatically influence the electric field image. Finally, we studied the charge state of titanium across a $PbTiO_3$-$SrTiO_3$ interface. Although titanium has the same formal valence state in both materials, we observed a change in the charge state based on Bader charge analysis. Although a change in the bonding configuration had previously been observed through EELS, these results conclusively demonstrate that there is also additional charge transfer associated with the change in bonding structure between the two materials. Taken together, these results represent a significant development in the capabilities of TEM to image the local electronic properties of materials.

In future research, more complex ferroelectric systems can be examined with 4D STEM to unravel the electronic properties of interfaces, domain walls, and defects. Although many of these structures have been studied through atomic resolution polarization mapping, scanning

probe microscopy, and electron energy-loss spectroscopy [18, 32–34, 44, 73], 4D STEM can provide unique information regarding the atomic scale electric field and charge distribution that is not available with any other method. This could lead to a better understanding of why unique polarization patterns appear and the mechanism for charge screening that occurs in many ferroelectric structures. For example, while this work focused mainly on ferroelectric-insulator heterostructures, the properties of ferroelectric-conductor interfaces have yet to be explored and will likely show very different behavior. In addition, incorporating 4D STEM with *in-situ* biasing could provide valuable insights into how the electronic properties respond to an external electric field which would be of great importance in applications. Outside of ferroelectrics, 4D STEM electric field and charge density imaging could also be applied to semiconductor devices to understand the electronic properties in cases where the sample geometry or the required spatial resolution makes conventional holography impractical [61, 113, 126].

In terms of the direct development of 4D STEM electric field and charge density imaging, significant work has already been done in terms of detector development. The most advanced direct electron detectors can now count every electron impact on the sensor with frame rates matching conventional STEM imaging [117, 118]. This will allow for 4D STEM to be acquired with larger fields of view with smaller step sizes than previously possible and will also enable the study of beam sensitive materials. There are still many opportunities to improve the theoretical understanding and analysis of 4D STEM electric field and charge density images. Currently, the electric field and charge density images are derived from relatively simple calculations performed for each CBED pattern. The development of more nuanced models for how the charge distribution affects CBED intensity, such as the multipole formalism [211], will lead to more accurate quantification of the charge density in materials. In addition, closer integration between first principles calculations and image simulations will significantly improve the understanding of how valence electrons influence charge density images from 4D STEM. New software packages are in development that may be helpful in this regard [202].

The analysis methods from machine learning also offer many opportunities for improving the quality of 4D STEM data [212] as well as compression of 4D STEM datasets [213]; the combination of these two may one day enable live 4D STEM imaging as is currently done with DPC.

Expanding outside of the electric field, the electron beam is also sensitive to the magnetic field of materials and DPC and 4D STEM have been applied to image a variety of magnetic structures [214–216]. Techniques for separating the electric and magnetic field fields in DPC/4D STEM data have also been developed [217]. But the most significant developments with respect to studying magnetic materials with 4D STEM will likely come from the newly developed field-free pole piece [218]. This new microscope design will bring atomic resolution imaging to the study of magnetic materials opening many new pathways for studying their combined electromagnetic properties.

Bibliography

1. Ronald E. Cohen. Origin of ferroelectricity in perovskite oxides. *Nature* **358,** 136–138 (1992).

2. Ravindran, P., Vidya, R., Kjekshus, A., Fjellvåg, H. & Eriksson, O. Theoretical investigation of magnetoelectric behavior in BiFe O3. *Physical Review B* **74** (2006).

3. Seshadri, R. & Hill, N. A. Visualizing the role of Bi 6s "lone pairs" in the off-center distortion in ferromagnetic BiMnO3. *Chemistry of Materials* **13,** 2892–2899 (2001).

4. Pitike, K. C., Parker, W. D., Louis, L. & Nakhmanson, S. M. First-principles studies of lone-pair-induced distortions in epitaxial phases of perovskite SnTiO3 and PbTiO3. *Physical Review B* **91,** 1–8 (2015).

5. Dawber, M., Rabe, K. M. & Scott, J. F. Physics of thin-film ferroelectric oxides. *Reviews of Modern Physics* **77,** 1083 (2005).

6. Scott, J. F. Applications of modern ferroelectrics. *Science* **315,** 954–959 (2007).

7. Schlom, D. G., Chen, L. Q., Pan, X., Schmehl, A. & Zurbuchen, M. A. A thin film approach to engineering functionality into oxides. *Journal of the American Ceramic Society* **91,** 2429–2454 (2008).

8. Catalan, G. & Scott, J. F. Physics and applications of bismuth ferrite. *Advanced Materials* **21,** 2463–2485 (2009).

9. Hoffman, J. *et al.* Ferroelectric Field Effect Transistors for Memory Applications. *Advanced Materials* **22,** 2957–2961 (2010).

10. Scott, J. F. & de Araujo, C. A. P. Ferroelectric Memories. *Science* **246,** 1400–1405 (1989).

11. Jeong, D. S. *et al.* *Emerging memories: resistive switching mechanisms and current status* 2012.

12. Han, S. T., Zhou, Y. & Roy, V. A. *Towards the development of flexible non-volatile memories* 2013.

13. Tsymbal, E. Y. & Kohlstedt, H. Tunneling across a ferroelectric. *Science* **313,** 181–183 (2006).

14. Garcia, V. *et al.* Giant tunnel electroresistance for non-destructive readout of ferroelectric states. *Nature 2009* **460,** 81–84 (2009).

15. Garcia, V. *et al.* Ferroelectric control of spin polarization. *Science* **327,** 1106–1110 (2010).

16. Gajek, M. *et al.* Tunnel junctions with multiferroic barriers. *Nature Materials 2007 6:4* **6,** 296–302 (2007).

17. Ma, J. *et al.* Controllable conductive readout in self-assembled, topologically confined ferroelectric domain walls. *Nature Nanotechnology* **13,** 947–952 (2018).

18. Li, L. *et al.* Giant Resistive Switching via Control of Ferroelectric Charged Domain Walls. *Advanced Materials* **28,** 6574–6580 (2016).

19. Sharma, P. *et al.* Nonvolatile ferroelectric domain wall memory. *Science Advances* **3,** e1700512 (2017).

20. Wang, J. *et al.* Epitaxial BiFeO3 Multiferroic Thin Film Heterostructures. *Science* **299,** 1719–1722 (2003).

21. Bark, C. W. *et al.* Tailoring a two-dimensional electron gas at the LaAlO3/SrTiO3 (001) interface by epitaxial strain. *Proceedings of the National Academy of Sciences* **108,** 4720–4724 (2011).

22. Schlom, D. G. *et al.* Strain tuning of ferroelectric thin films. *Annual Review of Materials Research* **37,** 589–626 (2007).

23. Martin, L. W., Chu, Y. H. & Ramesh, R. Advances in the growth and characterization of magnetic, ferroelectric, and multiferroic oxide thin films. *Materials Science and Engineering: R: Reports* **68,** 89–133 (2010).

24. Ramesh, R. & Spaldin, N. A. Multiferroics: progress and prospects in thin films. *Nature Materials 2007 6:1* **6,** 21–29 (2007).

25. Ohtomo, A. & Hwang, H. Y. A high-mobility electron gas at the LaAlO 3 /SrTiO 3 heterointerface. *Nature* **427,** 423–426 (2004).

26. Niranjan, M. K., Wang, Y., Jaswal, S. S. & Tsymbal, E. Y. Prediction of a Switchable Two-Dimensional Electron Gas at Ferroelectric Oxide Interfaces. *Physical Review Letters* **103,** 016804 (2009).

27. Zhang, Z., Wu, P., Chen, L. & Wang, J. First-principles prediction of a two dimensional electron gas at the BiFeO 3/SrTiO 3 interface. *Applied Physics Letters* **99,** 3–6 (2011).

28. Fredrickson, K. D. & Demkov, A. A. Switchable conductivity at the ferroelectric interface: Nonpolar oxides. *Physical Review B* **91,** 115126 (2015).

29. Yin, B., Aguado-Puente, P., Qu, S. & Artacho, E. Two-dimensional electron gas at the PbTi O3/SrTi O3 interface: An ab initio study. *Physical Review B* **92,** 1–11 (2015).

30. Siemons, W. *et al.* Origin of Charge Density at ¡span class. *Physical Review Letters* **98,** 196802 (2007).

31. Zhang, Y. *et al.* Intrinsic Conductance of Domain Walls in BiFeO3. *Advanced Materials* **31,** 1–7 (2019).

32. Zhang, Y. *et al.* Anisotropic polarization-induced conductance at a ferroelectric–insulator interface. *Nature Nanotechnology* **13,** 1132–1136 (2018).

33. Zhang, Y. *et al.* Discovery of a magnetic conductive interface in PbZr0.2Ti0.8O3 /SrTiO3 heterostructures. *Nature Communications* **9,** 685 (2018).

34. Huyan, H., Li, L., Addiego, C., Gao, W. & Pan, X. Structures and electronic properties of domain walls in BiFeO3 thin films. *National Science Review* **6,** 669–683 (2019).

35. Yadav, A. K. *et al.* Observation of polar vortices in oxide superlattices. *Nature* **530,** 198–201 (2016).

36. Hong, Z. *et al.* Stability of Polar Vortex Lattice in Ferroelectric Superlattices. *Nano Letters* **17,** 2246–2252 (2017).

37. Damodaran, A. R. *et al.* Phase coexistence and electric-field control of toroidal order in oxide superlattices. *Nature Materials* **16,** 1003–1009 (2017).

38. Das, S. *et al.* Observation of room-temperature polar skyrmions. *Nature* **568,** 368–372 (2019).

39. Estandía, S., Sánchez, F., Chisholm, M. F. & Gázquez, J. Rotational polarization nanotopologies in BaTiO3/SrTiO3 superlattices. *Nanoscale* **11,** 21275–21283 (2019).

40. Holtz, M. *et al.* Dimensionality-Induced Change in Topological Order in Multiferroic Oxide Superlattices. *Physical Review Letters* **126,** 157601 (2021).

41. Zavaliche, F. *et al.* Multiferroic BiFeO3 films: domain structure and polarization dynamics. *Phase Transitions* **79,** 991–1017 (2007).

42. Folkman, C. M. *et al.* Stripe domain structure in epitaxial (001) BiFeO 3 thin films on orthorhombic TbScO 3 substrate. *Applied Physics Letters* **94,** 1–4 (2009).

43. Chu, Y.-H. *et al.* Domain Control in Multiferroic BiFeO3 through Substrate Vicinality. *Advanced Materials* **19,** 2662–2666 (2007).

44. Nelson, C. T. *et al.* Spontaneous vortex nanodomain arrays at ferroelectric heterointerfaces. *Nano Letters* **11,** 828–834 (2011).

45. Xie, L. *et al.* Giant Ferroelectric Polarization in Ultrathin Ferroelectrics via Boundary-Condition Engineering. *Advanced Materials* **29,** 1–7 (2017).

46. Li, L. *et al.* Atomic Scale Structure Changes Induced by Charged Domain Walls in Ferroelectric Materials. *Nano Letters* **13,** 5218–5223 (2013).

47. Stemmer, S, Streiffer, S. K., Ernst, F & Rüuhle, M. Atomistic structure of 90° domain walls in ferroelectric PbTiO3 thin films. *Philosophical Magazine A* **71,** 713–724 (1995).

48. Li, Y. L., Hu, S. Y., Liu, Z. K. & Chen, L. Q. Effect of substrate constraint on the stability and evolution of ferroelectric domain structures in thin films. *Acta Materialia* **50,** 395–411 (2002).

49. Jia, C.-L. *et al.* Atomic-scale study of electric dipoles near charged and uncharged domain walls in ferroelectric films. *Nature Materials 2008 7:1* **7,** 57–61 (2007).

50. Du, K. *et al.* Manipulating topological transformations of polar structures through real-time observation of the dynamic polarization evolution. *Nature Communications* **10,** 1–8 (2019).

51. Li, X. *et al.* Atomic-scale observations of electrical and mechanical manipulation of topological polar flux closure. *Proceedings of the National Academy of Sciences* **117,** 18954–18961 (2020).

52. Chen, P. *et al.* Atomic imaging of mechanically induced topological transition of ferroelectric vortices. *Nature Communications* **11,** 1–8 (2020).

53. Williams, D. B. & Carter, C. B. *Transmission electron microscopy: A textbook for materials science* 1–760 (Springer US, 2009).

54. Giannuzzi, L. A. & Stevie, F. A. A review of focused ion beam milling techniques for TEM specimen preparation. *Micron* **30,** 197–204 (1999).

55. Haider, M. *et al.* Electron microscopy image enhanced. *Nature* **392,** 768–769 (1998).

56. Batson, P. E., Dellby, N & Krivanek, O. L. Sub-ångstrom resolution using aberration corrected electron optics. *Nature* **418,** 617–620 (2002).

57. Lichte, H. & Lehmann, M. Electron holography—basics and applications. *Reports on Progress in Physics* **71,** 016102 (2007).

58. Lichte, H., Geiger, D. & Linck, M. Off-axis electron holography in an aberration-corrected transmission electron microscope. *Philosophical Transactions of the Royal Society A: Mathematical, Physical and Engineering Sciences* **367,** 3773–3793 (2009).

59. Winkler, F. *et al.* Absolute Scale Quantitative Off-Axis Electron Holography at Atomic Resolution. *Physical Review Letters* **120,** 156101 (2018).

60. Boureau, V. *et al.* Quantitative Mapping of the Charge Density in a Monolayer of MoS2 at Atomic Resolution by Off-Axis Electron Holography. *ACS Nano* **14,** 524–530 (2019).

61. Haas, B., Rouvière, J. L., Boureau, V., Berthier, R. & Cooper, D. Direct comparison of off-axis holography and differential phase contrast for the mapping of electric fields in semiconductors by transmission electron microscopy. *Ultramicroscopy* **198,** 58–72 (2019).

62. Winkler, F., Barthel, J., Dunin-Borkowski, R. E. & Müller-Caspary, K. Direct measurement of electrostatic potentials at the atomic scale: A conceptual comparison between electron holography and scanning transmission electron microscopy. *Ultramicroscopy* **210,** 112926 (2020).

63. Nelson, C. T. *et al.* Domain Dynamics during Ferroelectric Switching. *Science* **334,** 968–971 (2011).

64. Gao, P. *et al.* Atomic mechanism of polarization-controlled surface reconstruction in ferroelectric thin films. *Nature Communications* **7,** 3–8 (2016).

65. Okunishi, E *et al.* Visualization of Light Elements at Ultrahigh Resolution by STEM Annular Bright Field Microscopy. *Microscopy and Microanalysis* **15,** 164–165 (2009).

66. Ishikawa, R. *et al.* Direct imaging of hydrogen-atom columns in a crystal by annular bright-field electron microscopy. *Nature Materials* **10,** 278–281 (2011).

67. Scanning Transmission Electron Microscopy (eds Pennycook, S. J. & Nellist, P. D.) (2011).

68. Carter, C. B. & Williams, D. B. *Transmission electron microscopy: Diffraction, imaging, and spectrometry* 1–518 (Springer International Publishing, 2016).

69. Xin, H. L. & Muller, D. A. Special number: Methods Aberration-corrected ADF-STEM depth sectioning and prospects for reliable 3D imaging in S/TEM. *Journal of Electron Microscopy* **58,** 157–165 (2009).

70. Vulović, M., Voortman, L. M., Van Vliet, L. J. & Rieger, B. When to use the projection assumption and the weak-phase object approximation in phase contrast cryo-EM. *Ultramicroscopy* **136,** 61–66 (2014).

71. Kirkland, E. J. *Advanced Computing in Electron Microscopy* 3rd ed. (Springer, Cham, 2020).

72. Cowley, J. M. & Moodie, A. F. The scattering of electrons by atoms and crystals. I. A new theoretical approach. *Acta Crystallographica* **10,** 609–619 (1957).

73. Li, L. *et al.* Defect-Induced Hedgehog Polarization States in Multiferroics. *Physical Review Letters* **120,** 137602 (2018).

74. Sun, Y. *et al.* Subunit cell–level measurement of polarization in an individual polar vortex. *Science Advances* **5,** 1–8 (2019).

75. Tan, H., Verbeeck, J., Abakumov, A. & Van Tendeloo, G. Oxidation state and chemical shift investigation in transition metal oxides by EELS. *Ultramicroscopy* **116,** 24–33 (2012).

76. Egerton, R. *Electron Energy-Loss Spectroscopy in the Electron Microscope* (Springer US, 2011).

77. Muller, D. A. *et al.* Atomic-Scale Chemical Imaging of Composition and Bonding by Aberration-Corrected Microscopy. *Science* **319,** 1073–1076 (2008).

78. Zhang, Z., Sigle, W. & Rühle, M. Atomic and electronic characterization of the a[100] dislocation core in SrTiO3. *Physical Review B* **66,** 094108 (2002).

79. Yoshiya, M., Tanaka, I., Kaneko, K. & Adachi, H. First principles calculation of chemical shifts in ELNES/NEXAFS of titanium oxides. *Journal of Physics: Condensed Matter* **11,** 3217 (1999).

80. Rez, P. & Muller, D. A. The Theory and Interpretation of Electron Energy Loss Near-Edge Fine Structure. *Annual Review of Materials Research* **38,** 535–558 (2008).

81. Ohtomo, A., Muller, D. A., Grazul, J. L. & Hwang, H. Y. Artificial charge-modulation in atomic-scale perovskite titanate superlattices. *Nature* **419,** 378–380 (2002).

82. Harada, K. Interference and interferometry in electron holography. *Microscopy* **70,** 3–16 (2021).

83. Koch, C. T. Towards full-resolution inline electron holography. *Micron* **63,** 69–75 (2014).

84. Harrison, R. J., Dunin-Borkowski, R. E. & Putnis, A. Direct imaging of nanoscale magnetic interactions in minerals. *Proceedings of the National Academy of Sciences* **99,** 16556–16561 (2002).

85. Song, K. *et al.* Direct imaging of the electron liquid at oxide interfaces. *Nature Nanotechnology* **13,** 198–203 (2018).

86. Boureau, V. *et al.* Quantitative Mapping of the Charge Density in a Monolayer of MoS2 at Atomic Resolution by Off-Axis Electron Holography. *ACS Nano* **14,** 524–530 (2020).

87. Yasin, F. S. *et al.* Probing Light Atoms at Subnanometer Resolution: Realization of Scanning Transmission Electron Microscope Holography. *Nano Letters* **18,** 7118–7123 (2018).

88. Rodenburg, J. M. & Bates, R. H. T. The theory of super-resolution electron microscopy via Wigner-distribution deconvolution. *Philosophical Transactions of the Royal Society of London. Series A: Physical and Engineering Sciences* **339,** 521–553 (1992).

89. Rodenburg, J. M. & Faulkner, H. M. A phase retrieval algorithm for shifting illumination. *Applied Physics Letters* **85,** 4795–4797 (2004).

90. Hawkes, P. W. *Advances in imaging and electron physics. Volume 150* (Elsevier/Academic Press, 2008).

91. Jiang, Y. *et al.* Electron ptychography of 2D materials to deep sub-ångström resolution. *Nature* **559,** 343–349 (2018).

92. Nellist, P. D., McCallum, B. C. & Rodenburg, J. M. Resolution beyond the 'information limit' in transmission electron microscopy. *Nature* **374,** 630–632 (1995).

93. Lozano, J. G., Martinez, G. T., Jin, L., Nellist, P. D. & Bruce, P. G. Low-Dose Aberration-Free Imaging of Li-Rich Cathode Materials at Various States of Charge Using Electron Ptychography. *Nano Letters* **18,** 6850–6855 (2018).

94. Yang, H. *et al.* Electron ptychographic phase imaging of light elements in crystalline materials using Wigner distribution deconvolution. *Ultramicroscopy* **180,** 173–179 (2017).

95. Dos Reis, R. *et al.* Determination of the structural phase and octahedral rotation angle in halide perovskites. *Applied Physics Letters* **112** (2018).

96. Wang, P., Zhang, F., Gao, S., Zhang, M. & Kirkland, A. I. Electron ptychographic diffractive imaging of boron atoms in LaB 6 crystals. *Scientific Reports* **7,** 1–8 (2017).

97. Lupini, A. R., Oxley, M. P. & Kalinin, S. V. Pushing the limits of electron ptychography: Subatomic probe sizes in convergent-beam electron microscopy offer new opportunities. *Science* **362,** 399–400 (2018).

98. Shibata, N. *et al.* Differential phase-contrast microscopy at atomic resolution. *Nature Physics* **8,** 611–615 (2012).

99. Müller, K. *et al.* Atomic electric fields revealed by a quantum mechanical approach to electron picodiffraction. *Nature Communications* **5** (2014).

100. Ophus, C. Four-Dimensional Scanning Transmission Electron Microscopy (4D-STEM): From Scanning Nanodiffraction to Ptychography and Beyond. *Microscopy and Microanalysis,* 563–582 (2019).

101. Hachtel, J. A., Idrobo, J. C. & Chi, M. Sub-Ångstrom electric field measurements on a universal detector in a scanning transmission electron microscope. *Advanced Structural and Chemical Imaging* **4** (2018).

102. Shukla, A. K. *et al.* Effect of composition on the structure of lithium- and manganese-rich transition metal oxides. *Energy Environ. Sci.* **11,** 830–840 (2018).

103. Mehta, A. N. *et al.* Unravelling stacking order in epitaxial bilayer MX2 using 4D-STEM with unsupervised learning. *Nanotechnology* **31,** 445702 (2020).

104. Mukherjee, D., Gamler, J. T. L., Skrabalak, S. E. & Unocic, R. R. Lattice Strain Measurement of Core@Shell Electrocatalysts with 4D Scanning Transmission Electron Microscopy Nanobeam Electron Diffraction. *ACS Catalysis* **10,** 5529–5541 (2020).

105. Ozdol, V. B. *et al.* Strain mapping at nanometer resolution using advanced nano-beam electron diffraction. *Applied Physics Letters* **106,** 253107 (2015).

106. LeBeau, J. M., Findlay, S. D., Allen, L. J. & Stemmer, S. Position averaged convergent beam electron diffraction: Theory and applications. *Ultramicroscopy* **110,** 118–125 (2010).

107. Panova, O. *et al.* Diffraction imaging of nanocrystalline structures in organic semiconductor molecular thin films. *Nature Materials* **18,** 860–865 (2019).

108. Ramesh, R. & Schlom, D. G. Creating emergent phenomena in oxide superlattices. *Nature Reviews Materials* **4,** 257–268 (2019).

109. Scott, J. F. Device physics of ferroelectric thin-film memories. *Japanese Journal of Applied Physics, Part 1: Regular Papers and Short Notes and Review Papers* **38,** 2272–2274 (1999).

110. Shibata, N. *et al.* Electric field imaging of single atoms. *Nature Communications* **8,** 2–4 (2017).

111. Sánchez-Santolino, G. *et al.* Probing the Internal Atomic Charge Density Distributions in Real Space. *ACS Nano* **12,** 8875–8881 (2018).

112. Bauer, B. *et al.* Direct detection of spontaneous polarization in wurtzite GaAs nanowires. *Applied Physics Letters* **104** (2014).

113. Shibata, N. *et al.* Direct Visualization of Local Electromagnetic Field Structures by Scanning Transmission Electron Microscopy. *Accounts of Chemical Research* **50,** 1502–1512 (2017).

114. Liu, L. *et al.* Regioselective generation and reactivity control of subnanometric platinum clusters in zeolites for high-temperature catalysis. *Nature Materials* **18,** 866–873 (2019).

115. Ishikawa, R. *et al.* Direct electric field imaging of graphene defects. *Nature Communications* **9,** 8–13 (2018).

116. Shibata, N. *et al.* New area detector for atomic-resolution scanning transmission electron microscopy. *Journal of Electron Microscopy* **59,** 473–479 (2010).

117. Ciston, J. *et al.* The 4D Camera: Very High Speed Electron Counting for 4D-STEM. *Microscopy and Microanalysis* **25,** 1930–1931 (2019).

118. Ercius, P. *et al.* The 4D Camera – An 87 kHz Frame-rate Detector for Counted 4D-STEM Experiments. *Microscopy and Microanalysis* **26,** 1896–1897 (2020).

119. Müller-Caspary, K. *et al.* Measurement of atomic electric fields and charge densities from average momentum transfers using scanning transmission electron microscopy. *Ultramicroscopy* **178,** 62–80 (2017).

120. Müller-Caspary, K. *et al.* Atomic-scale quantification of charge densities in two-dimensional materials. *Physical Review B* **98,** 1–5 (2018).

121. Fang, S. *et al.* Atomic electrostatic maps of 1D channels in 2D semiconductors using 4D scanning transmission electron microscopy. *Nature Communications* **10,** 1–9 (2019).

122. Carvalho, D. *et al.* Direct Measurement of Polarization-Induced Fields in GaN/AlN by Nano-Beam Electron Diffraction. *Scientific Reports* **6,** 1–9 (2016).

123. Müller-Caspary, K. *et al.* Electrical Polarization in AlN/GaN Nanodisks Measured by Momentum-Resolved 4D Scanning Transmission Electron Microscopy. *Physical Review Letters* **122,** 106102 (2019).

124. Yadav, A. K. *et al.* Spatially resolved steady-state negative capacitance. *Nature* **565,** 468–471 (2019).

125. Das, S. *et al.* Local negative permittivity and topological phase transition in polar skyrmions. *Nature Materials* **20,** 194–201 (2021).

126. Beyer, A. *et al.* Quantitative Characterization of Nanometer-Scale Electric Fields via Momentum-Resolved STEM. *Nano Letters* **21,** 2018–2025 (2021).

127. Midgley, P. A. Electronic Bonding Revealed by Electron Diffraction. *Science* **331,** 1528–1529 (2011).

128. Zuo, J. M., Kim, M., O'Keeffe, M. & Spence, J. C. H. Direct observation of d-orbital holes and Cu–Cu bonding in Cu¡sub¿2¡/sub¿O. *Nature* **401,** 49–52 (1999).

129. Zuo, J. M. Measurements of electron densities in solids: A real-space view of electronic structure and bonding in inorganic crystals. *Reports on Progress in Physics* **67,** 2053–2103 (2004).

130. Massa, L., Huang, L. & Karle, J. Quantum crystallography and the use of kernel projector matrices. *International Journal of Quantum Chemistry* **56,** 371–384 (1995).

131. Nakashima, P. N. H. Quantitative convergent-beam electron diffraction and quantum crystallography—the metallic bond in aluminium. *Structural Chemistry* **28,** 1319–1332 (2017).

132. Peng, D. & Nakashima, P. N. Measuring Density Functional Parameters from Electron Diffraction Patterns. *Physical Review Letters* **126,** 176402 (2021).

133. Nakashima, P. N., Smith, A. E., Etheridge, J. & Muddle, B. C. The bonding electron density in aluminum. *Science* **331,** 1583–1586 (2011).

134. Mohn, F., Gross, L., Moll, N. & Meyer, G. Imaging the charge distribution within a single molecule. *Nature Nanotechnology* **7,** 227–231 (2012).

135. Altman, E. I., Baykara, M. Z. & Schwarz, U. D. Noncontact Atomic Force Microscopy: An Emerging Tool for Fundamental Catalysis Research. *Accounts of Chemical Research* **48,** 2640–2648 (2015).

136. Han, Z. *et al.* Imaging the halogen bond in self-assembled halogenbenzenes on silver. *Science* **358,** 206–210 (2017).

137. Jackson, J. D. *Classical electrodynamics* 3rd ed., 808 (Wiley, New York, NY, 1999).

138. Zheng, Q. *et al.* Direct visualization of anionic electrons in an electride reveals inhomogeneities. *Science Advances* **7,** eabe6819 (2021).

139. Gao, W. *et al.* Real-space charge-density imaging with sub-ångström resolution by four-dimensional electron microscopy. *Nature* **575,** 480–484 (2019).

140. Lebeau, J. M. *et al.* High-angle scattering of fast electrons from crystals containing heavy elements: Simulation and experiment. *Physical Review B* **79,** 2–7 (2009).

141. Kim, Y.-M. *et al.* Direct observation of ferroelectric field effect and vacancy-controlled screening at the BiFeO3/LaxSr1 xMnO3 interface. *Nature Materials* **13,** 1019–1025 (2014).

142. Kresse, G. & Furthmüller, J. Efficient iterative schemes for ¡i¿ab initio¡/i¿ total-energy calculations using a plane-wave basis set. *Physical Review B* **54,** 11169 (1996).

143. Kresse, G. & Hafner, J. ¡i¿Ab initio¡/i¿ molecular-dynamics simulation of the liquid-metal–amorphous-semiconductor transition in germanium. *Physical Review B* **49,** 14251 (1994).

144. Perdew, J. P., Burke, K. & Ernzerhof, M. Generalized Gradient Approximation Made Simple. *Physical Review Letters* **77,** 3865 (1996).

145. Kresse, G. & Joubert, D. From ultrasoft pseudopotentials to the projector augmented-wave method. *Physical Review B* **59,** 1758 (1999).

146. Blöchl, P. E. Projector augmented-wave method. *Physical Review B* **50,** 17953 (1994).

147. Dudarev, S. L., Botton, G. A., Savrasov, S. Y., Humphreys, C. J. & Sutton, A. P. Electron-energy-loss spectra and the structural stability of nickel oxide: An LSDA U study. *Physical Review B* **57,** 1505 (1998).

148. Monkhorst, H. J. & Pack, J. D. Special points for Brillouin-zone integrations. *Physical Review B* **13,** 5188 (1976).

149. Elsässer, C., Fähnle, M., Chan, C. T. & Ho, K. M. Density-functional energies and forces with Gaussian-broadened fractional occupations. *Physical Review B* **49,** 13975 (1994).

150. Wang, Z., Wang, H., Yu, C. C. & Wu, R. Q. Hydrogen as a source of flux noise in SQUIDs. *Physical Review B* **98,** 020403 (2018).

151. Wang, H. *et al.* Candidate Source of Flux Noise in SQUIDs: Adsorbed Oxygen Molecules. *Physical Review Letters* **115,** 077002 (2015).

152. Wang, H. *et al.* Possibility of realizing quantum spin Hall effect at room temperature in stanene/Al2O3. *Physical Review B* **94,** 035112 (2016).

153. Kohn, W. & Sham, L. J. Self-Consistent Equations Including Exchange and Correlation Effects. *Physical Review* **140,** A1133 (1965).

154. Shannon, R. D. Revised effective ionic radii and systematic studies of interatomic distances in halides and chalcogenides. *Acta Crystallographica Section A* **32,** 751–767 (1976).

155. Moon, E. J. *et al.* Spatial control of functional properties via octahedral modulations in complex oxide superlattices. *Nature Communications* **5,** 5710 (2014).

156. Thomas, S. *et al.* Localized Control of Curie Temperature in Perovskite Oxide Film by Capping-Layer-Induced Octahedral Distortion. *Physical Review Letters* **119,** 177203 (2017).

157. Li, J. *et al.* Dramatically enhanced polarization in (001), (101), and (111) BiFeO3 thin films due to epitiaxial-induced transitions. *Applied Physics Letters* **84,** 5261 (2004).

158. Yu, P., Chu, Y. H. & Ramesh, R. Oxide interfaces: pathways to novel phenomena. *Materials Today* **15,** 320–327 (2012).

159. Spaldin, N. A., Cheong, S.-W. & Ramesh, R. Multiferroics: Past, present, and future. *Physics Today* **63,** 38 (2010).

160. Bert, J. A. *et al.* Direct imaging of the coexistence of ferromagnetism and superconductivity at the LaAlO3/SrTiO3 interface. *Nature Physics* **7,** 767–771 (2011).

161. Li, L., Richter, C., Mannhart, J. & Ashoori, R. C. Coexistence of magnetic order and two-dimensional superconductivity at LaAlO3/SrTiO3 interfaces. *Nature Physics* **7,** 762–766 (2011).

162. Tsukazaki, A. *et al.* Quantum Hall Effect in Polar Oxide Heterostructures. *Science* **315,** 1388–1391 (2007).

163. Guo, R. *et al.* Non-volatile memory based on the ferroelectric photovoltaic effect. *Nature Communications* **4,** 1990 (2013).

164. Henkelman, G., Arnaldsson, A. & Jónsson, H. A fast and robust algorithm for Bader decomposition of charge density. *Computational Materials Science* **36,** 354–360 (2006).

165. R. F. W. Bader. *Atoms in Molecules: A Quantum Theory, Oxford University Press* (Clarendon Press, 1990).

166. Rojac, T. *et al.* Domain-wall conduction in ferroelectric BiFeO3 controlled by accumulation of charged defects. *Nature Materials* **16,** 322–327 (2016).

167. Chen, C. *et al.* Two-dimensional electron gas at the Ti-diffused BiFeO3/SrTiO3 interface. *Applied Physics Letters* **107** (2015).

168. Campanini, M. *et al.* Periodic Giant Polarization Gradients in Doped BiFeO3 Thin Films. *Nano Letters* **18,** 717–724 (2018).

169. Tsuda, K., Yasuhara, A. & Tanaka, M. Two-dimensional mapping of polarizations of rhombohedral nanostructures in the tetragonal phase of BaTiO3 by the combined use of the scanning transmission electron microscopy and convergent-beam electron diffraction methods. *Applied Physics Letters* **103,** 1–5 (2013).

170. Campanini, M. *et al.* Atomic-resolution differential phase contrast STEM on ferroelectric materials: A mean-field approach. *Physical Review B* **101,** 184116 (2020).

171. Bürger, J., Riedl, T. & Lindner, J. K. Influence of lens aberrations, specimen thickness and tilt on differential phase contrast STEM images. *Ultramicroscopy* **219,** 113118 (2020).

172. Li, Y. L., Hu, S. Y., Liu, Z. K. & Chen, L. Q. Effect of electrical boundary conditions on ferroelectric domain structures in thin films. *Applied Physics Letters* **81,** 427–429 (2002).

173. Haun, M. J., Furman, E., Jang, S. J., McKinstry, H. A. & Cross, L. E. Thermodynamic theory of PbTiO3. *Journal of Applied Physics* **62,** 3331–3338 (1987).

174. Sheng, G. *et al.* A modified Landau-Devonshire thermodynamic potential for strontium titanate. *Applied Physics Letters* **96,** 108–111 (2010).

175. Wang, J. J., Ma, X. Q., Li, Q., Britson, J. & Chen, L. Q. Phase transitions and domain structures of ferroelectric nanoparticles: Phase field model incorporating strong elastic and dielectric inhomogeneity. *Acta Materialia* **61,** 7591–7603 (2013).

176. Chen, Z. H., Damodaran, A. R., Xu, R., Lee, S. & Martin, L. W. Effect of "symmetry mismatch" on the domain structure of rhombohedral BiFeO3 thin films. *Applied Physics Letters* **104,** 182908 (2014).

177. Peercy, P. S. The drive to miniaturization. *Nature* **406,** 1023–1026 (2000).

178. Claeys, C. Technological challenges of advanced CMOS processing and their impact on design aspects. *Proceedings of the IEEE International Conference on VLSI Design* **17,** 275–282 (2004).

179. Lundstrom, M. Moore's Law Forever? *Science* **299,** 210–211 (2003).

180. Lu, W. & Lieber, C. M. Semiconductor nanowires. *Journal of Physics D: Applied Physics* **39,** R387 (2006).

181. Wong, H. S. Beyond the conventional transistor. *Solid-State Electronics* **49,** 755–762 (2005).

182. Wang, A., Li, J. & Zhang, T. Heterogeneous single-atom catalysis. *Nature Reviews Chemistry* **2,** 65–81 (2018).

183. Hariki, A., Winder, M. & Kuneš, J. Continuum Charge Excitations in High-Valence Transition-Metal Oxides Revealed by Resonant Inelastic X-Ray Scattering. *Physical Review Letters* **121,** 126403 (2018).

184. Hall, E. R. *et al.* Valence-to-Core-Detected X-ray Absorption Spectroscopy: Targeting Ligand Selectivity. *Journal of the American Chemical Society* **136,** 10076–10084 (2014).

185. Muller, D. A. Structure and bonding at the atomic scale by scanning transmission electron microscopy. *Nature Materials* **8,** 263–270 (2009).

186. Olsson, F. E., Paavilainen, S., Persson, M., Repp, J. & Meyer, G. Multiple Charge States of Ag Atoms on Ultrathin NaCl Films. *Physical Review Letters* **98,** 176803 (2007).

187. Sterrer, M. *et al.* Control of the Charge State of Metal Atoms on Thin MgO Films. *Physical Review Letters* **98,** 096107 (2007).

188. Repp, J., Meyer, G., Olsson, F. E. & Persson, M. Controlling the Charge State of Individual Gold Adatoms. *Science* **305,** 493–495 (2004).

189. Wang, Y.-J., Zhu, Y.-L. & Ma, X.-L. Chiral phase transition at 180° domain walls in ferroelectric PbTiO3 driven by epitaxial compressive strains. *Journal of Applied Physics* **122,** 134104 (2017).

190. Cao, M. C. *et al.* Theory and practice of electron diffraction from single atoms and extended objects using an EMPAD. *Microscopy* **67,** i150–i161 (2018).

191. Ekuma, C. E., Jarrell, M., Moreno, J. & Bagayoko, D. First principle electronic, structural, elastic, and optical properties of strontium titanate. *AIP ADVANCES* **2,** 12189 (2012).

192. Ruiz, F. M. *et al.* Role of O 2p-Ti 3d orbital hybridization in dielectric and ferroelectric properties of barium zirconate titanate ceramics. *Materials Research Bulletin* **129,** 110905 (2020).

193. Khomskii, D. I. Transition Metal Compounds. *Transition Metal Compounds,* 1–485 (2014).

194. Enterkin, J. A. *et al.* A homologous series of structures on the surface of SrTiO3(110). *Nature Materials* **9,** 245–248 (2010).

195. Xin, H. *et al.* Effect of Mn doping defect on 180° domain wall in ferroelectric PbTiO3. *Physics Letters A* **384,** 126279 (2020).

196. Ghosez, P., Michenaud, J.-P. & Gonze, X. Dynamical atomic charges: The case of ABO3 Compounds. *Physical Review B* **58,** 6224 (1998).

197. Zhong, W., King-Smith, R. D. & Vanderbilt, D. Giant LO-TO splittings in perovskite ferroelectrics. *Physical Review Letters* **72,** 3618 (1994).

198. Gao, X. *et al.* Lithium Atom and A-Site Vacancy Distributions in Lanthanum Lithium Titanate. *Chemistry of Materials* **25,** 1607–1614 (2013).

199. Huang, C.-N. *et al.* Nonstoichiometric Titanium Oxides via Pulsed Laser Ablation in Water. *Nanoscale Research Letters* **5,** 972–985 (2010).

200. Ma, C. *et al.* Atomic-scale origin of the large grain-boundary resistance in perovskite Li-ion-conducting solid electrolytes. *Energy and Environmental Science* **7,** 1638–1642 (2014).

201. Lee, J.-S. *et al.* Titanium dx y ferromagnetism at the LaAlO3/SrTiO3 interface. *Nature Materials* **12,** 703–706 (2013).

202. Madsen, J. & Susi, T. abTEM: ab Initio Transmission Electron Microscopy Image Simulation. *Microscopy and Microanalysis* **26,** 448–450 (2020).

203. Susi, T. *et al.* Efficient first principles simulation of electron scattering factors for transmission electron microscopy. *Ultramicroscopy* **197,** 16–22 (2019).

204. Kirkland, E. J. Advanced computing in electron microscopy: Second edition. *Advanced Computing in Electron Microscopy: Second Edition,* 1–289 (2010).

205. Meyer, J. C. *et al.* Experimental analysis of charge redistribution due to chemical bonding by high-resolution transmission electron microscopy. *Nature Materials* **10,** 209–215 (2011).

206. Borghardt, S. *et al.* Quantitative Agreement between Electron-Optical Phase Images of WSe2 and Simulations Based on Electrostatic Potentials that Include Bonding Effects. *Physical Review Letters* **118,** 086101 (2017).

207. Krause, F. F. & Rosenauer, A. Reciprocity relations in transmission electron microscopy: A rigorous derivation. *Micron* **92,** 1–5 (2017).

208. Larsen, A. H. *et al.* The atomic simulation environment - a Python library for working with atoms. *Journal of Physics: Condensed Matter* **29,** 273002 (2017).

209. Lobato, I. & Dyck, D. V. An accurate parameterization for the scattering factors, electron densities and electrostatic potentials for neutral atoms that obey all physical constraints. *Acta Crystallographica Section A* **70,** 636–649 (2014).

210. Addiego, C., Gao, W. & Pan, X. Thickness and defocus dependence of inter-atomic electric fields measured by scanning diffraction. *Ultramicroscopy,* 112850 (2019).

211. Wu, L., Meng, Q. & Zhu, Y. Mapping valence electron distributions with multipole density formalism using 4D-STEM. *Ultramicroscopy* **219,** 113095 (2020).

212. Zhang, C., Han, R., Zhang, A. R. & Voyles, P. M. Ultramicroscopy Denoising atomic resolution 4D scanning transmission electron microscopy data with tensor singular value decomposition. *Ultramicroscopy* **219,** 113123 (2020).

213. Jesse, S. *et al.* Big Data Analytics for Scanning Transmission Electron Microscopy Ptychography. *Scientific Reports* **6,** 1–8 (2016).

214. Matsumoto, T., So, Y. G., Kohno, Y., Ikuhara, Y. & Shibata, N. Stable Magnetic Skyrmion States at Room Temperature Confined to Corrals of Artificial Surface Pits Fabricated by a Focused Electron Beam. *Nano Letters* **18,** 754–762 (2018).

215. Matsumoto, T. *et al.* Quantum Physics: Direct observation of 7 domain boundary core structure in magnetic skyrmion lattice. *Science Advances* **2,** 1–6 (2016).

216. Krajnak, M., McGrouther, D., Maneuski, D., O'Shea, V. & McVitie, S. Pixelated detectors and improved efficiency for magnetic imaging in STEM differential phase contrast. *Ultramicroscopy* **165,** 42–50 (2016).

217. Campanini, M, Nasi, L, Albertini, F & Erni, R. Disentangling nanoscale electric and magnetic fields by time-reversal operation in differential phase-contrast STEM Disentangling nanoscale electric and magnetic fields by time-reversal operation in differential phase-contrast STEM. **154102** (2020).

218. Shibata, N. *et al.* Atomic resolution electron microscopy in a magnetic field free environment. *Nature Communications 2019 10:1* **10,** 1–5 (2019).

Appendix A

Derivation of the projected electric field with the phase object approximation

This section will present a short derivation of the electric field in a sample starting from the exit wave that is the result of using the phase object approximation. This can be insightful since the assumptions made during the derivation in Chapter 1 will be visible directly in the mathematics. This derivation is adapted from Ref. [62]. Starting from momentum expectation value of the exiting probe (Eq. 2.4), we will carry out the integration in real-space instead of momentum space so the momentum transfer can be expressed as

$$\langle \mathbf{p}_{\perp} \rangle (\mathbf{r_o}) = \int \Psi^{*}_{\mathrm{obj}}(\mathbf{r}, \mathbf{r}_o) \left(-i\hbar\nabla\right) \Psi_{\mathrm{obj}}(\mathbf{r}, \mathbf{r}_o) d^2\mathbf{r} \tag{A.1}$$

where $-i\hbar\nabla$ is the momentum operator now expressed in real-space. Plugging in the result from the phase object approximation (Eq. 1.17), the result is

$$\langle \mathbf{p}_{\perp} \rangle (\mathbf{r_o}) = -i\hbar \int \Psi_o^*(\mathbf{r}, \mathbf{r}_o) e^{-i\sigma V_{\text{proj}}} \; \nabla \; \Psi_o(\mathbf{r}, \mathbf{r}_o) e^{i\sigma V_{\text{proj}}} d^2\mathbf{r} \tag{A.2}$$

Computing the gradient by applying the product and chain rules, yields two expectation values: one for the momentum of the initial probe, and a second one which represents the momentum transferred by the sample's potential

$$\langle \mathbf{p}_{\perp} \rangle_o (\mathbf{r_o}) = -i\hbar \int \Psi_o^*(\mathbf{r}, \mathbf{r}_o) \; \nabla \; \Psi_o^*(\mathbf{r}, \mathbf{r}_o) d^2\mathbf{r} \tag{A.3}$$

$$\langle \mathbf{p}_{\perp} \rangle_{\text{obj}} (\mathbf{r_o}) = -i\hbar \int |\Psi(\mathbf{r}, \mathbf{r}_o)|^2 e^{-i\sigma V_{\text{proj}}} \; \nabla \; e^{-i\sigma V_{\text{proj}}} d^2\mathbf{r} \tag{A.4}$$

So the final momentum transfer is

$$\langle \mathbf{p}_{\perp} \rangle (\mathbf{r_o}) = \langle \mathbf{p}_{\perp} \rangle_o (\mathbf{r_o}) + \langle \mathbf{p}_{\perp} \rangle_{\text{obj}} (\mathbf{r_o}) \tag{A.5}$$

Now we can explicitly see that the final momentum transfer includes both the initial probe momentum and that imparted by the sample. The electron probe is always slightly asymmetric due lens aberrations, so in experiment, we approximate $\langle \mathbf{p}_{\perp} \rangle_o (\mathbf{r_o})$ as the average over the momentum over the all scan positions. However, for the sake of this derivation, we will assume the probe is perfectly symmetric, so $\langle \mathbf{p}_{\perp} \rangle_o (\mathbf{r_o}) = 0$. With this assumption, the only remaining term is Eq. A.4. Further simplifying Eq. A.4 by applying the chain rule, the momentum transfer can be expressed as

$$\langle \mathbf{p}_{\perp} \rangle (\mathbf{r_o}) = \hbar\sigma \int |\Psi(\mathbf{r}, \mathbf{r}_o)|^2 \; \nabla \; V_{\text{proj}} \; d^2\mathbf{r} \tag{A.6}$$

If we now recognize that the square of Ψ_o is just the intensity of the initial probe, this integral can be expressed as a convolution between the probe's initial intensity and the gradient of

the projected potential, which is the electric field. Therefore, we arrive at the final result

$$\langle \mathbf{p}_\perp \rangle(\mathbf{r_o}) = \hbar\sigma(I_o \otimes \nabla V_{\text{proj}})(\mathbf{r}_o) \tag{A.7}$$

$$\frac{-1}{\hbar\sigma}\langle \mathbf{p}_\perp \rangle(\mathbf{r_o}) = \langle \mathbf{E}_\perp \rangle(\mathbf{r}_o) \tag{A.8}$$

where $\langle \mathbf{E}_\perp \rangle(\mathbf{r}_o)$ is the electric field of the sample at position $\mathbf{r}_o$ convolved with the probe's intensity. This result shows that the momentum transfer is linearly proportional to the electric field of the sample and is equivalent to Eq. 2.9. However, starting from the phase object approximation to arrive at the same result just makes it explicit that this technique is a simple form of phase reconstruction (retrieving the gradient of the phase instead of the phase itself) and has made the convolution with the probe's initial intensity explicit.

Appendix B

Position averaged CBED thickness measurements

As described in Ch. 1 and 2, measuring the sample thickness along the beam direction is important in order to quantify the electric field and charge density measured with 4D STEM. Position averaged CBED (PACBED) patterns offer a convenient method for measuring the thickness of samples. PACBED patterns are collected by scanning the probe over a small region, and incoherently averaging the CBED pattern from all probe positions together. This can be done simply by inserting a camera and capturing with a long exposure time as the probe scans. The resulting diffraction pattern is insensitive to any lens aberrations or contrast variations that depend on the probe's position in the unit cell, but is highly sensitive to sample thickness and zone-axis alignment. As demonstrated by Ref. [106], the thickness and zone-axis alignment of a sample can be easily determined by simply comparing the experimental PACBED pattern with those generated by STEM image simulations. This comparison can be done by either qualitative comparison or quantitative least squares error. When using the least square error, we normalize the intensity range in the simulated and experimental data and then sum the squared difference between each pixel in the experimental

and simulated PACBED patterns.

The sample thickness was measured using PACBED in all experiments in this work. We collect PACBED data at an intermediate convergence angle (10 mrad) because the change in features associated with sample thickness and zone-axis alignment are more readily visible in this condition. The PACBED data for the sample used in Ch. 2 is presented in that chapter; this appendix presents the PACBED data used to determine the sample thickness in all other chapters.

In Ch. 3, for the sample region used to measure the E-field and charge density of bulk STO, we measured the thickness quantatitvely with least squares error. As shown in Fig. B.1, the thickness was found to be 5.6 nm. The thickness for the bulk BFO was found to be 6-8 nm based on comparison with simulated PACBEDs from bulk BFO, as shown in Fig. B.2. Note that the PACBED pattern appears asymmetric in this case due to the symmetry breaking polarization in BFO. Fig. B.3 shows the experimental PACBED pattern taken from the interface region from Ch. 3; comparison with the experimental and simulated PACBED from Fig. B.1 indicates this region is also 5-6 nm thick.

In Ch. 4, the region used for atomic resolution electric field measurement using a high convergence angle was found to be 12 nm based on least squares error, as shown in Fig. B.4a. As demonstrated in Ch. 2 and Ref. [171], this is sufficient for the E-field to be qualitatively correct, but there is likely significant error in the quantitative value. However, this does not affect the results of this section as the vortex pattern would remain unchanged. The thickness in the region used for imaging the nanometer scale electric field with a low convergence angle was found to be 16 nm as shown in Fig. B.4b. Refs. [119, 124] demonstrated that measurements of the electric field with a low convergence angle probe are relatively unaffected by sample thickness, so the thickness of this region should not affect the electric field measurement.

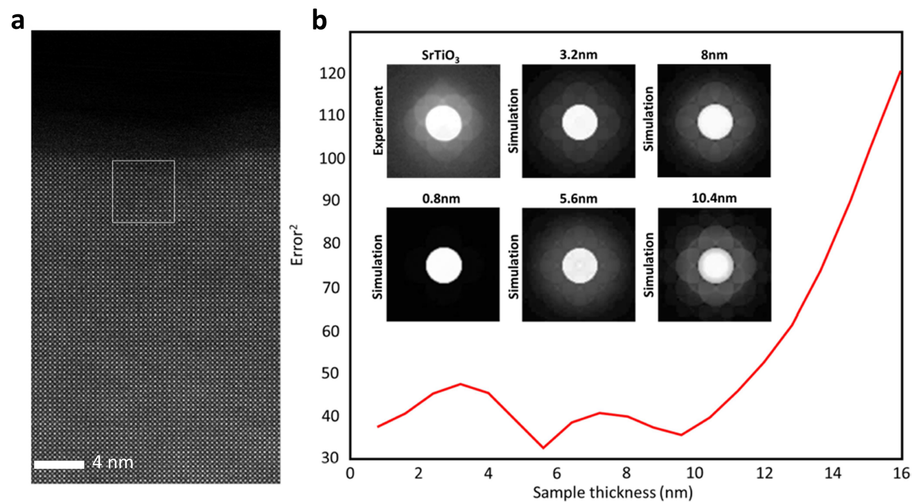

Figure B.1: **Bulk STO PACBED. a**, Region where 4D STEM and PACBED data was collected. The highlighted region shows where the PACBED pattern was collected. **b**, Least-squares error of the experimental PACBED results compared with the simulated PACBEDs (red line). The inset shows the PACBED acquired from the boxed region in the STEM image, and simulated PACBEDs of STO with thicknesses from 0.8 nm to 10.4 nm.

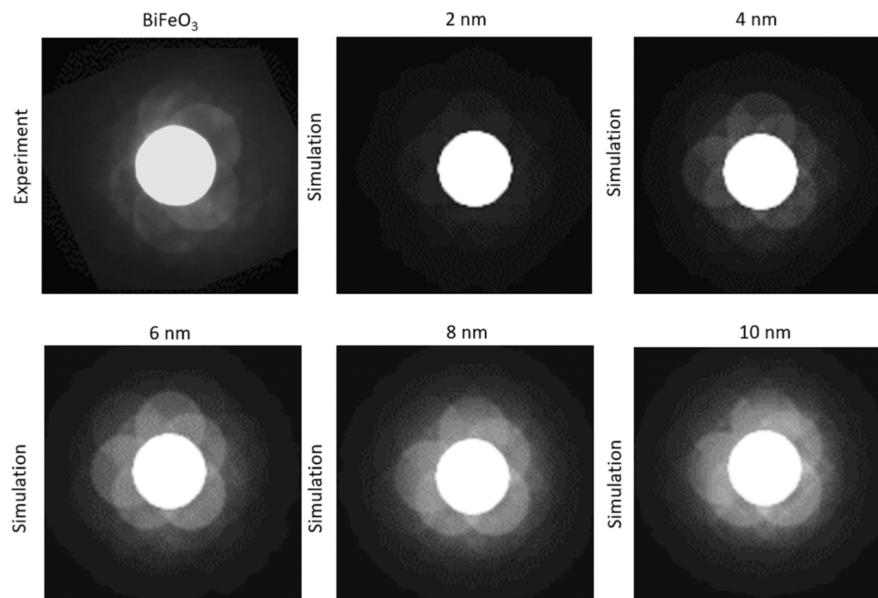

Figure B.2: **BFO bulk PACBED.** Shown are the PACBED acquired in experiment and simulated PACBEDs for BFO with thicknesses of 2–10 nm.

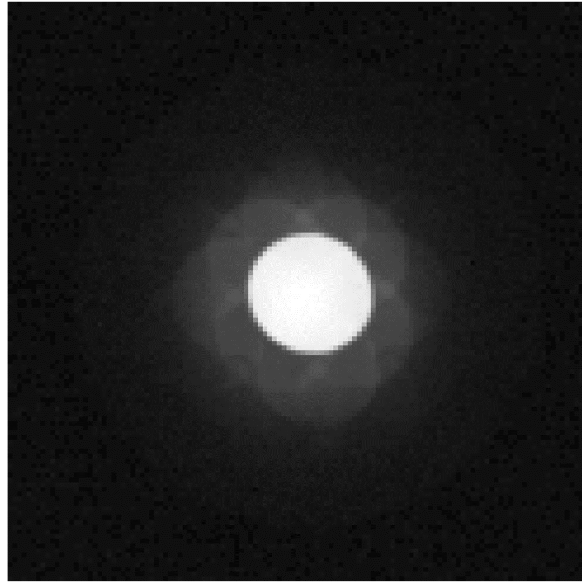

Figure B.3: **BFO-STO interface PACBED.** The PACBED pattern collected from the BFO-STO interface. The pattern appears more symmetric because polarization is reduced near the interface and some unit cells in STO are included in the scanned region.

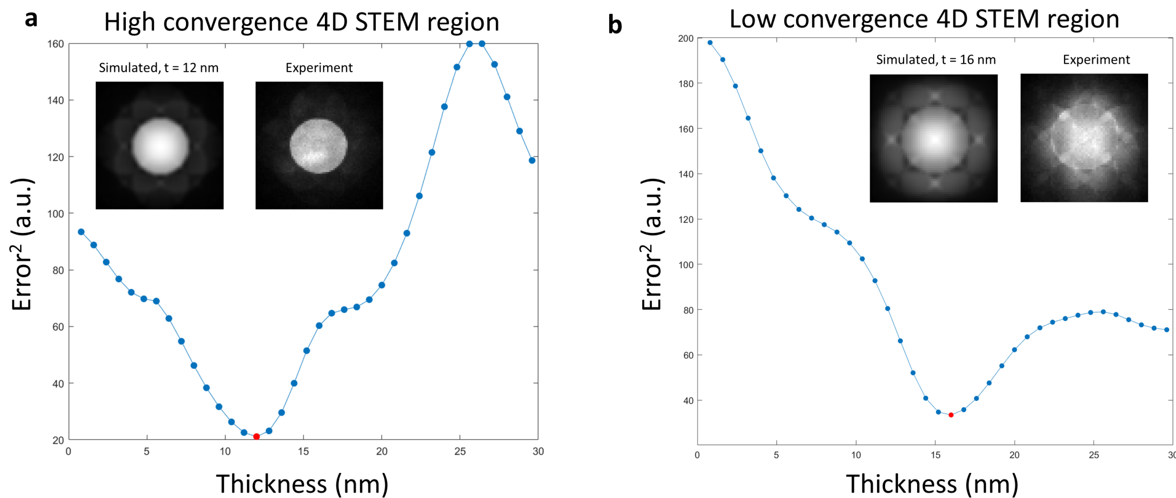

Figure B.4: **PTO-STO superlattice PACBED. a-b**, comparison of experimental and simulated PACBED patterns taken from the region where high convergence (**a**) and low convergence (**b**) 4D STEM data were acquired in Ch. 4. Minimum least square error is highlighted in red. The insets shows the simulated PACBED pattern corresponding to the minimum squared-error and experimental PACBED patterns.

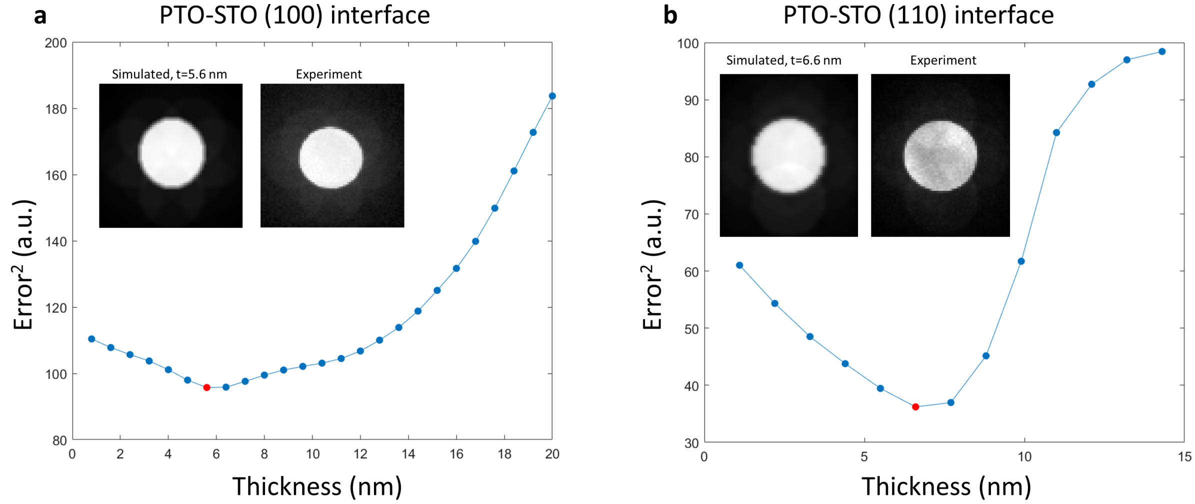

Figure B.5: **PTO-STO interface PACBED. a-b**, Comparison of experimental and simulated PACBED patterns taken from the PTO-STO (100) (**a**) and the (110) (**b**) interface in Ch. 5. Minimum least square error is highlighted in red. The insets shows the simulated PACBED pattern corresponding to the minimum squared-error and experimental PACBED patterns.

In Ch. 5, the region imaged from the (100) orientation of the PTO/STO interface was found to be 5.6 nm in thickness, as shown in B.5a. The region imaged from the (110) orientation was found to be 6.6 nm in thickness, as shown in B.5b. The region of the CBED pattterns used for comparison in B.5b are rectangular because the unit cell in (110) projection is also rectangular, not square as it is in the (100) projection.